National Library of Canada

Acquisitions and Bibliographic Services Branch

395 Wellington Street
Ottawa, Ontario
K1A 0N4

Bibliothèque nationale du Canada

Direction des acquisitions et des services bibliographiques

395, rue Wellington
Ottawa (Ontario)
K1A 0N4

Your file Votre référence

Our file Notre référence

NOTICE

The quality of this microform is heavily dependent upon the quality of the original thesis submitted for microfilming. Every effort has been made to ensure the highest quality of reproduction possible.

If pages are missing, contact the university which granted the degree.

Some pages may have indistinct print especially if the original pages were typed with a poor typewriter ribbon or if the university sent us an inferior photocopy.

AVIS

La qualité de cette microforme dépend grandement de la qualité de la thèse soumise au microfilmage. Nous avons tout fait pour assurer une qualité supérieure de reproduction.

S'il manque des pages, veuillez communiquer avec l'université qui a conféré le grade.

La qualité d'impression de certaines pages peut laisser à désirer, surtout si les pages originales ont été dactylographiées à l'aide d'un ruban usé ou si l'université nous a fait parvenir une photocopie de qualité inférieure.

Canada

OTTAWA-CARLETON INSTITUTE OF PHYSICS
UNIVERSITY OF OTTAWA
DEPARTMENT OF PHYSICS

PRESSURE-INDUCED STRUCTURAL MODIFICATIONS IN DIOXIDES OF GROUP IVB ELEMENTS: TiO_2, ZrO_2 AND HfO_2

by

KEN LAGAREC

Thesis submitted to the School of Graduate Studies
of the University of Ottawa in partial fulfilment
for the degree of Master of Science

ISBN 0-612-11568-2

Canada

UNIVERSITÉ D'OTTAWA
UNIVERSITY OF OTTAWA

ABSTRACT

A study of the pressure-induced structural phase transitions of dioxides of group IVB elements was performed, using X-ray diffraction and Raman spectroscopy. TiO_2, ZrO_2 and HfO_2 represent important compounds for the global understanding of the high-pressure phases of MO_2 compounds.

Four specific studies are presented in this thesis, regarding the high-pressure phases of the three compounds. ZrO_2 was studied at pressures of up to 73 GPa using energy dispersive X-ray (EDX) diffraction techniques. The quenched phase was analysed using angle dispersive X-ray (ADX) diffraction with imaging plates, and was identified as having a cotunnite-type structure (space group *Pnma*) by Rietveld refinement. HfO_2 was also studied to 72 GPa using EDX diffraction measurements, and its quenched phase was also identified as having a cotunnite-type structure, based on the similarities of its EDX and Raman spectra with those of the quenched phase of ZrO_2. TiO_2 was involved in two separate studies. The first is a Raman spectroscopic study up to 73 GPa, starting with anatase. Some EDX diffraction measurements were also taken to pressures up to 105 GPa. Additionally, EDX diffraction measurements of TiO_2 up to 28 GPa were taken to determine the equations of state of its high-pressure phases, starting with anatase and rutile at atmospheric pressure.

Both ZrO_2 and HfO_2 followed the same pressure-induced transitions, evolving from their atmospheric baddeleyite-type structure ($P2_1/c$) to an orthorhombic phase with space group *Pbca*, and finally to a cotunnite-type phase (*Pnma*) which was quenched to atmospheric pressure, producing pure samples of high density cotunnite-type ZrO_2 and HfO_2 which have exceptionally high bulk moduli, 444 ± 15 and 340 ± 10 GPa, respectively.

When starting with anatase, TiO_2 was observed to transform to the columbite-type structure at 4.5 GPa (or α-PbO_2-type), then to a baddeleyite-type structure around 15 GPa. Raman spectroscopic measurements also seemed to indicate the transformation to a new structure at pressures exceeding 60 GPa, based on important intensity changes in the spectra. A new peak was also observed using X-ray diffraction at a pressure of 105 GPa. When starting

with rutile, the intermediate phase was not observed, and the sample partially transformed to the baddeleyite-type structure around 12 GPa, leaving traces of rutile at pressures higher than 23 GPa.

These three compounds might provide a link between the behaviour of dioxides with small cation radii (such as TiO_2) and those with larger cation radii such as HfO_2 and ZrO_2. TiO_2 is the first such compound found to transform to a baddeleyite-type structure under pressure, and it might thus be expected to transform like HfO_2 and ZrO_2 from that point. The identification of a cotunnite phase for both ZrO_2 and HfO_2 is of great importance since this structure is expected to be the stable high-pressure structure of dioxides with large cation radii.

RÉSUMÉ

Une étude des transitions de phases structurales induites par la pression dans les dioxydes d'éléments du groupe IVB a été réalisée en utilisant la diffraction des rayons-X et la spectroscopie Raman. Le TiO_2, ZrO_2 et HfO_2 représentent des matériaux clés pour une compréhension globale des phases denses des dioxydes.

Quatre études individuelles sont présentées dans cette thèse, relatives aux phases à haute pression de ces trois matériaux. Le ZrO_2 a été étudié jusqu'à 73 GPa en utilisant la méthode de diffraction des rayons X en énergie (DXE). La phase haute pression qui fut retenue à l'ambiante a ensuite fait l'étude de diffraction des rayons X en angle (DXA) et fut identifiée comme ayant une structure du type cotunnite (groupe *Pnma*) par une analyse Rietveld. Le HfO_2 fut aussi étudié jusqu'à 72 GPa en DXE, et sa phase haute pression fut aussi retenue dans la structure cotunnite, ainsi que déterminée par la ressemblance des spectres DXE et Raman avec ceux de la phase cotunnite du ZrO_2. Le TiO_2 fut impliqué dans deux études distinctes. La première fut une étude en spectroscopie Raman jusqu'à 73 GPa, en commençant avec de l'anatase. Quelques mesures de DXE ont aussi été prises jusqu'à 105 GPa. Ensuite, des mesures de DXE furent effectuées sur du TiO_2 jusqu'à 28 GPa pour déterminer les équations d'état de ses phases à haute pression. Celles-ci furent réalisées pour des échantillons de rutile et d'anatase.

Le ZrO_2 et le HfO_2 passent par les mêmes transitions de phases, progressant de leur structure à pression atmosphérique du type baddeleyite ($P2_1/c$) à une structure orthorhombique du groupe d'espace *Pbca*, puis finalement à une structure du type cotunnite (*Pnma*) qui put être retenue à pression atmosphérique, produisant des échantillons purs de ZrO_2-cotunnite et HfO_2-cotunnite de haute densité des modules de compression extrêmement élevés ($B_0 = 444 \pm 15$ et 340 ± 10 GPa, respectivement).

Le TiO_2, débutant dans la structure anatase, se transforme dans une structure du type columbite (ou α-PbO_2) vers 4.5 GPa, puis dans une structure du type baddeleyite aux alentours de 15 GPa. Des données de spectroscopie Raman semblent aussi indiquer une nouvelle

transition à des pressions au-delà de 60 GPa, identifiée grâce à d'importants changements d'intensité dans les spectres. Une nouvelle réflexion fut aussi observée en diffraction des rayons X à 105 GPa. En commençant avec la phase rutile, la phase intermédiaire n'est pas observée, et l'échantillon se transforme partiellement dans la structure du type baddeleyite vers 12 GPa, laissant des traces de rutile à des pressions supérieures à 23 GPa.

Les trois composés étudiés peuvent indiquer un lien entre les comportements de dioxydes avec des cations de petits rayons, tels que le TiO_2, et ceux qui ont des cations de rayons plus grands, tels que le ZrO_2 et le HfO_2. Le TiO_2 est le premier de ces composés qui présente une structure du type baddeleyite à haute pression, et il pourrait évoluer comme le ZrO_2 et le HfO_2 à partir de cette phase. L'identification de la phase du type cotunnite est d'importance, puisque cette structure est supposée être la forme stable des dioxydes à cations de rayons élevés.

ACKNOWLEDGMENTS

This project is the result of numerous hours of work on my part and that of my supervisor, Dr. Desgreniers. However, there are also a great number of people who have made this possible.

I would first like to thank my parents, Catherine and Daniel and my brother Antoine for their continuing support throughout my education and especially my graduate work. I am also thankful to them for their proofreading of this document. I dedicate this work to them, guaranteeing it will not be the last, for I am forever in their debt.

My supervisor, Dr. Serge Desgreniers has also played an important part in the completion of this work. He has been able to motivate me to perform the hard work necessary, but has also given me invaluable skills in experimental research and shown me the joys of getting the work accomplished properly. I am also in his debt for putting up with the numerous drafts of this thesis that came before this final copy.

There are a number of people of the Physics Department who have helped me throughout my graduate work, with whom I have had important or simply interesting conversations: Claude Desruisseaux, Robert Parent, Richard Legault and everybody else who runs the Department and makes it a pleasure to work there. I would also like to thank Dr. Keith Brister at the Cornell High Energy Synchrotron Source (CHESS) with whom I have now worked for over two years, for always helping us with setups and calibrations, and sometimes also listening for possible improvements of the setup.

I would also like to thank several friends for proofreading this thesis and for providing useful remarks regarding the clarity of the text, namely Brian Dooling, Benoît Mareschal and John Minnery.

REMERCIEMENTS

Cette étude est le résultat de nombreuses heures de labeur de ma part, ainsi que de la part de mon directeur de thèse, Dr. Desgreniers. Il y a cependant un grand nombre d'individus qui l'ont rendu possible.

J'aimerais tout d'abord remercier mes parents, Catherine et Daniel, et mon frère Antoine pour leur appui incessant au cours de mes études, surtout lors de mes études supérieures. Je leur suis aussi reconnaissant d'avoir relu ce document. Je leur dédie cet ouvrage, me tenant garant que ce ne sera pas le dernier car je leur suis éternellement obligé. Je dédie aussi ce travail à ma grand-mère, décédée cette année, qui a toujours été très fière de mon travail et qui m'a montré combien il est important de prendre plaisir à son travail et à sa vie.

Mon directeur de thèse, Dr. Serge Desgreniers a aussi joué un rôle primordial dans l'accomplissement de ce travail. Il fut capable de me garder motivé pour que je persévère malgré le travail à accomplir, mais il m'a aussi inculqué les méthodes de la recherche expérimentale et m'a montré la joie d'avoir proprement accompli son travail. Je lui suis aussi reconnaissant d'avoir corrigé les nombreux brouillons de cette thèse qui virent jour avant cette version finale.

Il y a beaucoup de personnes du département de physique qui m'ont aidé au cours de mes études supérieures, avec qui j'ai pu avoir d'importantes ou simplement d'intéressantes conversations: Claude Desruisseaux, Robert Parent, Richard Legault et tout le personnel qui fait marcher le département et qui le rend si agréable. J'aimerais aussi remercier Dr. Keith Brister du Cornell High Energy Synchrotron Source avec qui j'ai maintenant travaillé pour plus de deux ans, pour nous avoir toujours aidé avec les calibrations et les manipulations, et pour nous avoir parfois écouté au sujet d'améliorations de l'appareillage.

Il y a certains amis que j'aimerais remercier d'avoir relu cette thèse et d'y avoir porté des critiques intéressantes: Brian Dooling, Benoît Mareschal et John Minnery.

STATEMENT OF ORIGINALITY

This project includes several experiments and findings which appear to be original:

- ZrO_2 and HfO_2 were studied up to quasi-hydrostatic pressures of around 70 GPa using energy dispersive X-ray diffraction with synchrotron radiation, yielding more information than other studies performed up to 50 GPa.

- A pure phase of cotunnite-type ZrO_2 was obtained by quenching the high-pressure phase. This phase was identified as having a cotunnite-type ($PbCl_2$) structure, based on energy and angle dispersive X-ray diffraction, as well as Raman spectroscopy. This phase is stable to at least 70 GPa.

- The high-pressure phase of HfO_2 (post-*Pbca*) was clearly identified as having a cotunnite-type structure, as observed by energy dispersive X-ray diffraction and Raman spectroscopy. It was also quenched to atmospheric pressure. This phase is also stable to at least 70 GPa.

- A Raman spectroscopic study of the pressure-induced behaviour of TiO_2 was performed using a single crystal of anatase. This identified that the crystallinity of the sample is an important factor for the transition to the columbite-type structure.

- Two programs were written to anaylse the X-ray diffraction data, greatly increasing our productivity throughout this research.

TABLE OF CONTENTS

LIST OF FIGURES AND TABLES

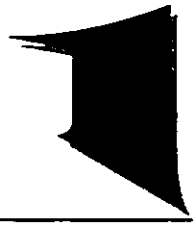

INTRODUCTION TO HIGH-PRESSURE PHYSICS

The field of high-pressure physics has long been a relatively obscure science for those who were not involved in it, and only a few scientists could be credited for the great number of innovations and discoveries it prompted. For obvious technical reasons, the study of the temperature behaviour of materials has become a more common field of study than the effect of pressure. With the emergence of this field in the early twentieth century, the high-pressure researchers seemed more focused on making diamond out of graphite than anything else, yet their understanding of the effect of pressure on solids grew enormously, even if they weren't all able to devise the right technical apparatus and experiment to grow diamonds. Now, the synthesis of diamond from graphite is well known, and yet the science is still progressing, for example to achieve a better understanding of the dynamics of materials inside the Earth (at the center of which the pressure is ~360 GPa) and inside other planets. In addition, a more industrial branch has developed, seeking new types of materials, in particular stable high-density compounds harder than diamond.

For geological purposes, the knowledge of the pressure-based behaviour of post-stishovite SiO_2 is of great importance, since it is the main component of the Earth's crust and mantle. Since the Si^{4+} cation has a very small radius, the transition pressures to high-pressure phases are higher than that of similar compounds of the MO_2 type which have larger cation radii, making it necessary and useful to study these compounds and try to find a global scheme and common structures. The dioxides of group IVB elements are distinctive in this sense since they comprise the smaller Ti^{4+} cation and the larger Zr^{4+} or Hf^{4+} cations. A common high pressure structure in their dioxides could be a link between the two classes of small and large cation radii dioxides.

For these reasons, we have decided to study the pressure induced phases of TiO_2, ZrO_2 and HfO_2, using both Raman spectroscopy and X-ray diffraction using synchrotron radiation.

This introductory chapter deals with the generation and measurement of very high pressures as those used in our experiments, with a foreground on the behaviour of solids, in particular dioxides, under pressure. Following is a precise description of the experimental procedures used in this research. Because of the extreme similarity of ZrO_2 and HfO_2, a single chapter is devoted to their study, with a final chapter on our study of anatase and rutile TiO_2.

1.1 The Behaviour of Solids Under Hydrostatic Pressure

1.1.1 Structural Phase Transitions

The structure into which a compound forms is such that the Gibbs free energy (G) of the system is minimized at a given temperature T and pressure P, yielding a system with internal energy E, entropy S and volume V:

$$G = E - TS + PV. \tag{1.1}$$

When applying pressure, the internal energy of the structure increases with the decrease in volume, and in some conditions, a different atomic configuration might provide a lower resulting free energy. At a given temperature, the entropy of the system might also be decreased in such a transformation of the structure. When considering the (P, T) diagram of a compound, the compound will thus be observed in different structures.

In our case, constant room temperature is maintained, and we study in particular the structural *phase transitions* in the compounds (the compounds studied are non-magnetic, so we don't observe magnetic phase transitions in which the magnetic ordering is changed to lower the free energy).

As a rule of thumb, during a phase transition, the higher pressure phase has a lower volume and a higher coordination number than the lower pressure phase. The coordination number of a given atom or ion represents the number of nearest neighbours of another type.

In our study, the coordination number refers to the number of anions (O^{2-}) surrounding each cation (Ti^{4+}, Zr^{4+} or Hf^{4+}). In an ionic compound, it is reasonable that an increase in cation-anion coordination reduces the internal energy because of their attractive interaction. The phase transition can thus partially be characterized by the relative volume decrease and the change in coordination number.

When studying powdered samples, the presence of a large number of crystallites and their boundary interactions might increase the range of pressure over which the transition takes place. In single crystals, the transition is usually faster since a seed of the new phase can grow unobstructed by crystallite boundaries. Also, depending on the relation between the two structures, the single crystal might break into several crystallites of the new structure if several seeds which have different orientations appear.

1.1.2 Isothermal Equations of State (EOS)

1.1.2.1 The Murnaghan Integrated Linear EOS

Two characteristic quantities that determine the behaviour of solids under pressure are the bulk modulus at null pressure, which is given by

$$B_0 = -V\left(\frac{\partial P}{\partial V}\right)_{P=0}, \tag{1.2}$$

and the pressure derivative of the bulk modulus, at null pressure,

$$B_0' = \left(\frac{\partial B}{\partial P}\right)_{P=0}. \tag{1.3}$$

We could generate a very elementary EOS by assuming that the bulk modulus is constant over a given pressure range, in which case we get

$$V = V_0 \exp\left(-\frac{P}{B_0}\right). \tag{1.4}$$

This, however, is unrealistic, except for very low pressures. Instead, through experimentation,

Murnaghan demonstrated that the bulk modulus could be expressed as a function of three elastic constants λ, μ and P_0 (which could be taken as null pressure) [Murnaghan, 1944].

$$B_0 = \tfrac{1}{3}(\lambda+\mu+P_0). \tag{1.5}$$

Assuming that λ and μ are linear functions of pressure, which means B_0' is a constant, we obtain the *Murnaghan integrated linear EOS*:

$$P = \frac{B_0}{B_0'}\left[\left(\frac{V_0}{V}\right)^{B_0'} - 1\right]. \tag{1.6}$$

1.1.2.2 The Birch-Murnaghan EOS

A more rigorous theoretical derivation of an EOS can be obtained by expanding the Helmoltz free energy $F = G + TS$ of the solid in terms of f, the compression, using a finite strain hypothesis. In this case, the EOS is obtained by using the definition of pressure

$$P = \left(\frac{\partial F}{\partial V}\right)_T. \tag{1.7}$$

In the finite strain approximation, the compression f is defined as

$$\frac{V_0}{V} = (1+2f)^{3/2}. \tag{1.8}$$

Another intermediate result obtained during the derivation [Poirier, 1991] is that

$$9B_{0T}V_0 = \lim_{P\to 0}\left(\frac{1}{f}\frac{\partial F}{\partial f}\right)_T. \tag{1.9}$$

Now we do an expansion of the free energy (assumed to be 0 in the unstrained state)

$$F = a(T)f^2 + b(T)f^3 + c(T)f^4 + O(f^5). \tag{1.10}$$

When using a second order expansion, we get the *second-order Birch-Murnaghan EOS*

$$P = \frac{3}{2}B_0\left[\left(\frac{V_0}{V}\right)^{7/3} - \left(\frac{V_0}{V}\right)^{5/3}\right]. \tag{1.11}$$

In the same way, we get the *third-order Birch-Murnaghan EOS*

$$P = \frac{3}{2}B_0\left[\left(\frac{V_0}{V}\right)^{7/3} - \left(\frac{V_0}{V}\right)^{5/3}\right]\left(1+\frac{3}{4}(B_0'-4)\left[\left(\frac{V_0}{V}\right)^{2/3} - 1\right]\right). \tag{1.12}$$

This is the most widely used isothermal EOS in geophysics and is the one we use in this report. Any references to B_0 and B_0' correspond to this equation. This result was first published by Birch [1952] in a short communiqué related to the works of Murnaghan [1944]. A comprehensive derivation can also be found in Poirier [1991].

1.1.2.3 The Vinet EOS

The desire of finding a universal EOS has spurred many interesting ideas regarding the behaviour of solids under pressure. Several ultra-high pressure EOS's were known and derived from statistical mechanics, such as the Fermi-Dirac EOS for a cloud of electrons, but none could be found which would be universal enough to be independent of the type of interaction between the components of the matter. More recently, Vinet *et al.* [1986] proposed a method to determine a universal bulk modulus from a V *vs.* P diagram, since fitting the curve to a particular equation affects the value of the bulk modulus. It is considered universal because it can be successfully applied to several types of atomic interactions, corresponding to many types of compounds. We will not give any detail regarding the determination of the parameters, but it is worthwhile to explore in the cases where the Birch-Murnaghan EOS doesn't work.

1.1.3 The Current State of Dioxide Phase Diagrams

Much work has been done on the behaviour of MO_2 compounds under pressure, and this section presents a brief description of their similarities and expected behaviours. A comprehensive review can be found in Liu *et al.* [1986]. These compounds can be categorized into four groups, based on their position in the Periodic Table: the elements of group IVA, the tetravalent transition elements (Cr, Ir, Mn, *etc.*.), the elements of group IVB, and the last group includes lanthanides, actinides and Po. A more physical approach is to categorize them according to their structure at atmospheric pressure. In this case, we have quartz-type dioxides (which have α-quartz, β-quartz, tridymite or cristobalite structures), rutile-type dioxides (GeO_2, SnO_2, PbO_2, TiO_2, MnO_2, RuO_2, and TeO_2), baddeleyite-type dioxides (ZrO_2 and HfO_2) and fluorite-type dioxides (TbO_2, PrO_2, CeO_2, UO_2, and ThO_2).

Liu [1982] observed that the behaviour of the dioxides is greatly dependent on the size of the cation, creating two main groups which until now had very few known common structures, genrally refered to as the quartz and rutile-type (for the smaller radii cations) and cotunnite-type (for the larger radii cations) classes. Additionally, ZrO_2 and HfO_2 (mid-size cations) are distinct, since they occur naturally in a baddeleyite-type structure. One classical example usually cited is that of TiO_2, which never assumed a baddeleyite-type structure like HfO_2 and ZrO_2. This has recently been revoked since the observation of such a phase in TiO_2 by Sato *et al.* [1991]. Apart from the quartz-type dioxides, all other dioxides share several particular structures. The rutile-type dioxides are known to transform into a columbite-type (α-PbO_2-type) structure, and then into a fluorite structure. The two baddeleyite-type dioxides are expected to transform into a cotunnite-type structure at high pressure, even though the latest research identifies a tetragonal symmetry structure for HfO_2 [Léger, 1993b] and the expected cotunnite-type structure for ZrO_2 [Haines, 1995]. At high temperature, both ZrO_2 and HfO_2 adopt a fluorite-type structure which is also expected to transform into a cotunnite-type structure at high temperature and high pressure. The fluorite-type dioxides are expected to stay in their initial structure or possibly evolve to a cotunnite-type structure, as observed in

non-stoichiometric $TbO_{1.75}$. Since the discovery of the baddeleyite-type phase of TiO_2, it seems that TiO_2 is a link which bridges the gap between the rutile-type dioxides and the baddeleyite-type dioxides. It is thus expected that TiO_2 could still evolve to either a cotunnite or a fluorite-type phase.

This research deals specifically with the three dioxides of the group IVB elements, for which we study the room temperature high-pressure phases' structural properties and phase transitions. Along with the determination of the equations of state of the known phases of these compounds, we wish to ascertain the presence of a high-pressure cotunnite of HfO_2 and ZrO_2, and to look for a post-baddeleyite phase of TiO_2. These goals would provide a better understanding of the relation between the smaller and larger cation radii dioxides and bring more evidence supporting the high-pressure stability cotunnite-type structure.

1.2 Generating and Measuring High Hydrostatic Pressures

1.2.1 The Diamond Anvil Cell (DAC)

Since the beginning of high-pressure physics, there has always been a need for the improvement of the high pressure generating apparatus; in most cases, the early high-pressure scientists were basically designing and building their own. Several designs have been used over time, and most were greatly improved by the use of diamond as a pressure inducing medium. Its hardness and optical transparency make it a material of choice for applying pressure.

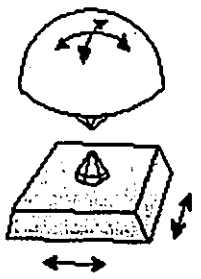

Figure 1.1 Diamond anvil alignment mechanism

1.2.1.1 Design of the DAC

Of the still numerous designs available today, the Mao-Bell design is one of the most common for generating very high static pressures. In all our experiments, we have used only one DAC, which is a lever-type modified Mao-Bell diamond anvil cell (**Figure 1.3**). The diamond anvils are cut from low birefringence and low fluorescence Type IA stones. A piston, above which is located a diamond anvil with a flat culet, is inserted inside a bore in which there is another identical diamond. In this DAC, the lower diamond anvil is glued onto a WC (tungsten carbide) base which can be adjusted in a horizontal plane. The top diamond anvil is glued on a WC hemisphere, permitting the diamond's tilt to be adjusted (**Figure 1.1**). Using four screws on each anvil's base, the diamond anvils were interferometrically aligned, using a Na lamp. For very high pressure experiments, the alignment of the two opposed anvils is such that a maximum angle of 0.05° between the two faces of the diamonds could be accepted.

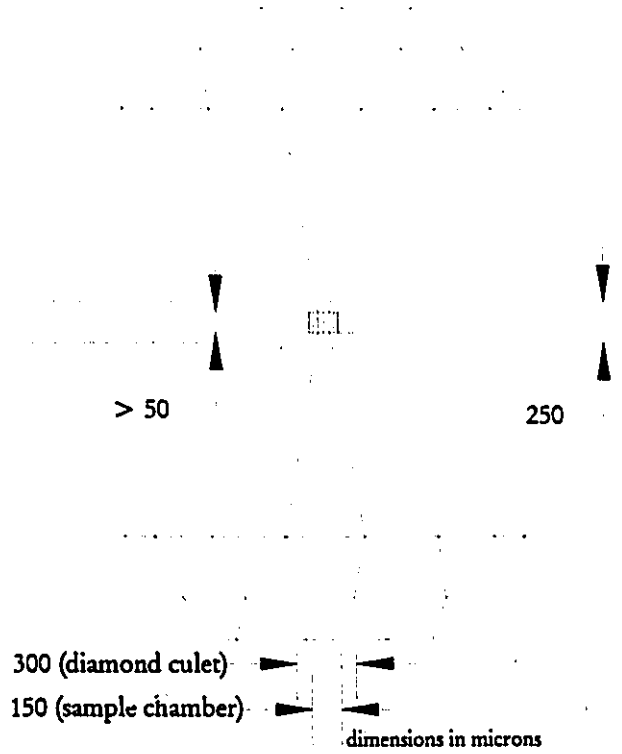

Figure 1.2 Schematic view of the diamond anvils, the gasket and the sample chamber.

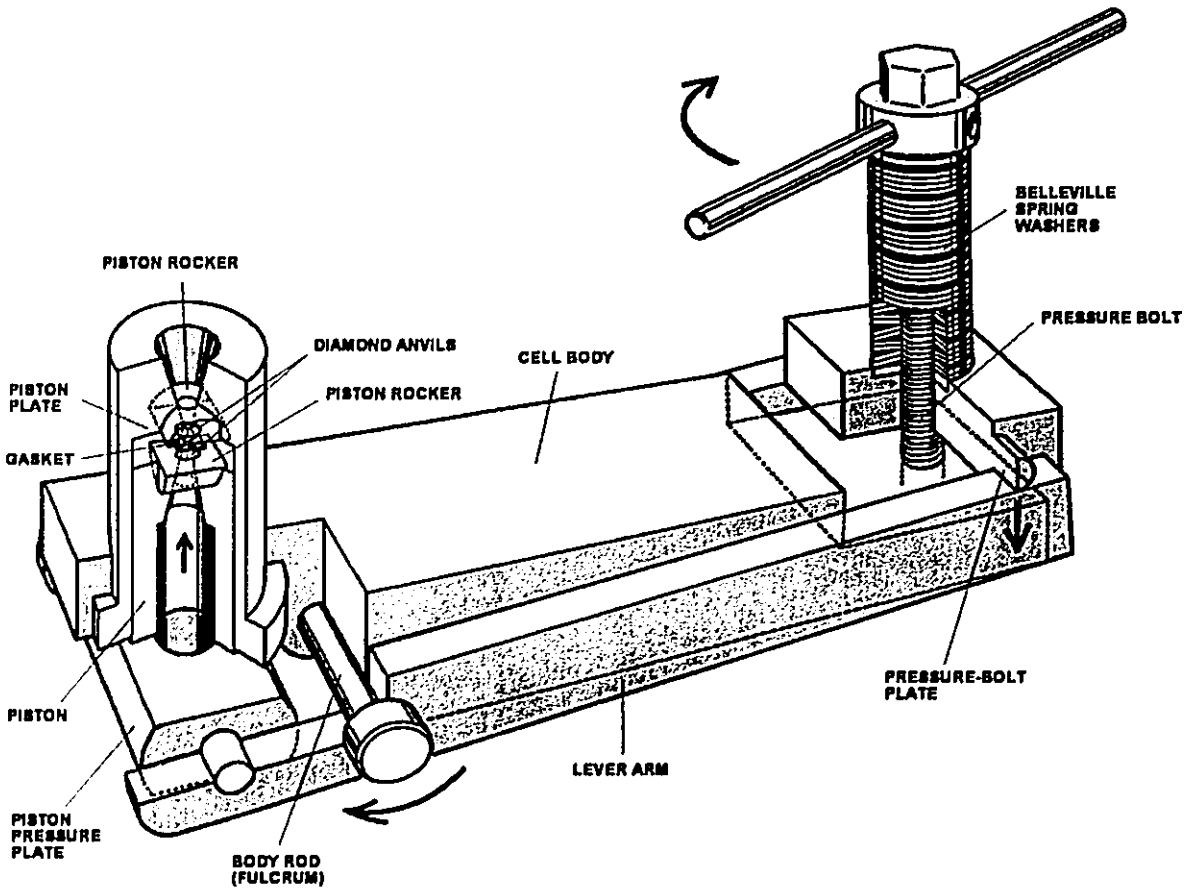

Figure 1.3 Example of the thrust mechanism of a lever-type DAC similar to the one used in our experiments. In this design, the tightening of the bolt exerts a vertical force on the piston, which translates into a very high pressure in the sample chamber, because of the size differential between the piston and the diamond anvil's culet (3 cm: 300 μm). (Figure from Jayaraman [1984])

Using the Na lamp, the interference fringes caused by the two partially reflecting diamond faces were required to be larger than the diameter of the face. Once properly aligned and tightened, this DAC could be used for several runs up to 60 GPa with no further alignment correction. The piston and bore are then inserted into the lever, which is activated using a ½" pressure bolt (**Figure 1.3**).

1.2.1.2 The Gasket and the Pressure Transmitting Medium

The sample itself is placed in a chamber between the two diamond anvil faces (**Figure 1.2**). A hardened stainless steel (AISI T301) gasket is used to hold the sample and to prevent any contact between the diamond culets. This gasket, which is roughly 250 μm thick initially, is pre-indented to 50 to 70 μm and then drilled in the centre of the indentation using a high precision drill with WC drill bits. The size of the hole depends on the size of the diamond culets. In general, we used diamond anvils which had 300 μm culets in diameter, and we drilled a hole of 150 μm in diameter. Once replaced on the piston diamond anvil, the sample could be loaded in the pressure chamber, along with the pressure calibration material.

To ensure that the pressure acting on the sample be as hydrostatic as possible, a pressure transmitting medium was used to fill the hole before the chamber was closed. In some cases, the sample was simply packed in the hole, but generally, either a 4:1 mixture of methanol and ethanol or silicone oil were used to transmit the pressure hydrostatically and to prevent the hole from collapsing. Both these media are liquid at ambient temperature and pressure, but solidify in amorphous or nearly amorphous states at pressures of ~10 GPa. Other pressure transmitting media can also be used to improve on these, like very high density rare gases. Even though cryogenic loadings have been attempted with this DAC, we did not believe the added complexity was necessary for these experiments.

1.2.1.3 Using Bevelled Diamonds for Higher Pressures

When using the diamond anvils with 300 μm culets, a plateau of 70-75 GPa was systematically reached, indicating a point where the diamonds might break under load. When applying very high pressures, diamond anvil culets are under a great deal of stress, especially near the edges. A better design is to have a bevelled tip, which has for instance a flat central surface of 100 μm in diameter, and 5° bevels, greatly reducing the deformation of the diamond anvil which may lead to fracture. Those diamond anvils were used once in a TiO_2 experiment, in which we were able to generate pressures above 100 GPa. To reach very high pressures, it is also possible to use much smaller diamond anvil tips, thus greatly increasing the pressure on the sample while keeping the same force provided by the leverage system.

1.2.2 Pressure Measurements

1.2.2.1 Using $Al_2O_3:Cr^{3+}$ as an Optical Pressure Gauge

Since the introduction of transparent diamond anvils for generating high pressures, several optical methods have been used to determine the pressure inside the sample chamber. All these methods work on the basis of a pre-calibration of the optical gauge by comparison with other types of gauges derived from materials with known EOS. Ruby ($Al_2O_3:Cr^{3+}$) has proven to be very useful and sufficiently accurate for pressure determinations up to the 100 GPa range.

The insertion of Cr impurities in aluminum oxide produces R-type colour centres, which present two characteristic fluorescence peaks around 694.2 nm, giving ruby its bright red colour. These fluorescence peaks correspond to transitions through the electronic states of the Cr^{3+} impurities in the Al_2O_3 lattice. Under static compression, these electronic levels change slightly, enabling us to determine the pressure, based on the shift from the uncompressed state. Because these fluorescence peaks occur in the visible red region, they can

be excited using an optical laser, and can also be faintly excited by X-rays.

Mao *et al.* [1978] have precisely calibrated the evolution of the R_1 fluorescence line in ruby using Cu, Mo, Pd and Ag and their respective isothermal EOS's and several DACs, for pressures ranging from 6 to 100 GPa. A non-linear model was shown to correctly reflect the shift of the R_1 line for quasi-hydrostatic pressures up to 100 GPa, replacing the linear relationship proposed earlier for pressures up to 20 GPa:

$$P\,(\mathrm{GPa}) = 380.8\left(\left[\frac{\lambda_0+\Delta\lambda}{\lambda_0}\right]^5 - 1\right). \qquad (1.13)$$

This is the calibration we used to measure pressure using ruby chips. A precise measurement of λ_0 has to be taken before every loading since it partially depends on the concentration of Cr in the ruby used.

1.2.2.2 Using Metals With a Known EOS for X-Ray Diffraction

When we did not have access to an optical system to record the ruby fluorescence while performing X-ray diffraction, a small quantity of a powdered metal with a well known EOS was placed with the sample in the chamber. It is very important to chose the metal according to the needs of the experiment, so that its diffraction and X-ray fluorescence lines interfere the least with the sample lines, that it be sufficiently compressible to get a good accuracy on the pressure and that its crystalline structure be simple and stable as a function of pressure. At high pressures, since the material becomes less compressible, a very high precision measurement of the pressure calibration compound's volume is needed, so any small experimental error (such as the positioning of the DAC) might produce a large error on the pressure estimate. Whenever possible, a ruby was thus used to measure pressure. Otherwise, we used either Pt or Mo, depending on the material being studied. In all the cases, the parameters for a third-order Birch-Murnaghan EOS were used.

2

EXPERIMENTAL METHODS

In this study, two experimental methods are used to get information about the crystalline structure of the samples: X-ray diffraction and Raman spectroscopy. Although the two methods involve substantially different physical phenomena, both are related to the underlying crystal structure, therefore producing two sets of complementary results. Since the phenomena we are dealing with are different by nature, experimental conditions can limit the use of one of the procedures, if it fails or is inconclusive. The strategy of using both of these methods is relatively standard and is very frequent in this type of research, since the analysis of only one type of data is usually insufficient to conclude on a given structure, and can sometimes even mislead the analysis. Whenever possible, we have therefore explored our sample by X-ray diffraction and Raman spectroscopy, and used both sets of data to obtain a corroborative solution.

Other probing techniques such as electron diffraction, neutron diffraction or infrared spectroscopy are also useful to determine crystal structures and should be used whenever possible, offering more insight on specific characteristics of the structure. Unfortunately, when studying samples in the DAC, we do not have the means to explore most of the other methods. However, we are confident that the two probing techniques we have selected give sufficiently convincing results. Generally X-ray diffraction was used to determine the possible space groups of the structure which could then be confirmed or accepted according to our Raman data; usually, the actual structure could not be identified by Raman analysis alone. Also, both methods were used to confirm the existence of phase transitions, and to determine the pressures at which they occur.

This chapter provides an introduction to the physics involved in X-ray diffraction and Raman spectroscopy as well as a description of the experimental aspects of data acquisition, with a prologue on crystal structures and their physical properties.

2.1 Crystal Structures

In this section, we discuss the properties of crystal structures, elaborated to view and classify them in useful and insightful ways.

2.1.1 The Unit Cell and the Bravais Lattices

A crystal is composed of atoms or molecules arranged according to a pattern which has long range spatial correlations. Unlike amorphous materials which present a short range correlated pattern, a crystal is highly ordered and is characterized by a small number of parameters pertaining to its atomic order.

Long range ordering means that if the atomic positions and the organizational pattern are known in one part of the crystal, they can be predicted exactly in any other part through translation of the pattern according to specific vectors. Such a pattern can then serve to describe the whole crystal. This permits us to define the *Bravais lattice* as an «infinite array of discrete points with an arrangement and orientation that appears *exactly* the same, from whichever of the points the array is viewed» [Aschcroft, 1976]. In 3D geometry, this is equivalent to defining 3 non-collinear vectors ($\vec{a}_i$) that are used to span the array of points: given any origin in the crystal, if $\vec{r}$ is a point in the array, then $\vec{r}' = n_1\vec{a}_1 + n_2\vec{a}_2 + n_3\vec{a}_3$, ($n_i \in$ Z) represents another point in the array. This translational property is what gives crystals long range spatial correlations. Also, one sees that a volume defined by $(\vec{a}_1,\vec{a}_2,\vec{a}_3)$ can be used to characterize the whole crystal by defining a *unit cell*. When using only non-translational properties (point symmetries), one can design only seven different crystal systems, forcing specific properties onto the unit cell vectors. These are known as *point groups* of the Bravais lattices. Additionally, when considering the complete set of properties, including translational properties, this generates fourteen distinct space groups, known as the *Bravais lattices* (**Table 2.1**).

Table 2.1 The seven crystal systems and the fourteen Bravais lattices

Symmetry requirements	Crystal system	Lattice parameters	Bravais lattices
1 or $\bar{1}$	**Triclinic**	no conditions	P
2 or $\bar{2}$	**Monoclinic**	$\alpha = \gamma = 90°$	P, C
three perpendicular 2-fold axes or mirror planes, or two mirror planes and one 2-fold axis	**Orthorhombic**	$\alpha = \beta = \gamma = 90°$	P, I, F, C
4 or $\bar{4}$	**Tetragonal**	$a = b$ $\alpha = \beta = \gamma = 90°$	P, I
3 or $\bar{3}$	**Trigonal**	$a = b$ $\alpha = \beta = 90°$ $\gamma = 60°$	P
	Rhombohedral:		or
	i) on Rhomb. axes	$a = b = c$ $\alpha = \beta = \gamma$	R
	ii) on Hex. axes	$a = b$ $\alpha = \beta = 90°$ $\gamma = 60°$	
6 or $\bar{6}$	**Hexagonal**	$a = b$ $\alpha = \beta = 90°$ $\gamma = 60°$	P
four 3-fold axes	**Cubic**	$a = b = c$ $\alpha = \beta = \gamma = 90°$	P, I, F

P: primitive cell
I: body-centred cell
F: face-centred cell
C: base-centred cell in $(\vec{a},\vec{b})$ plane (by convention)
R: rhobohedral cell

2.1.2 The 230 Space Groups and 32 Point Groups

For real crystals, the points referred to in the definition of the Bravais lattice correspond to an atom or a group of atoms and possibly molecules, which will be referred to as the *basis* of the lattice. In the definition of the Bravais lattice, this basis was attributed no

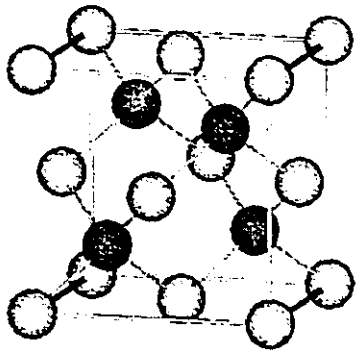

Figure 2.1 The unit cell of diamond. It is an FCC Bravais lattice with two atoms per point, at positions (0,0,0) (light atoms) and (¼, ¼, ¼) (dark atoms). The covalent bonds between atoms are represented, showing the characteristic tetrahedral configuration of carbon.

spatial dimension (or can have been considered to have the ideal spherical symmetry), giving it complete orientational and inversion invariance, but the real objects that serve as a basis do have specific orientational properties. The new possible symmetry groups obtained now depend on the symmetry of the Bravais lattice, but also on the symmetry of the basis object. These additional properties now create 32 possible crystallographic point groups, instead of the seven crystal systems previously discussed. The point groups represent symmetry operations that take the crystal structure onto itself, while leaving one point fixed (no translations involved: rotation

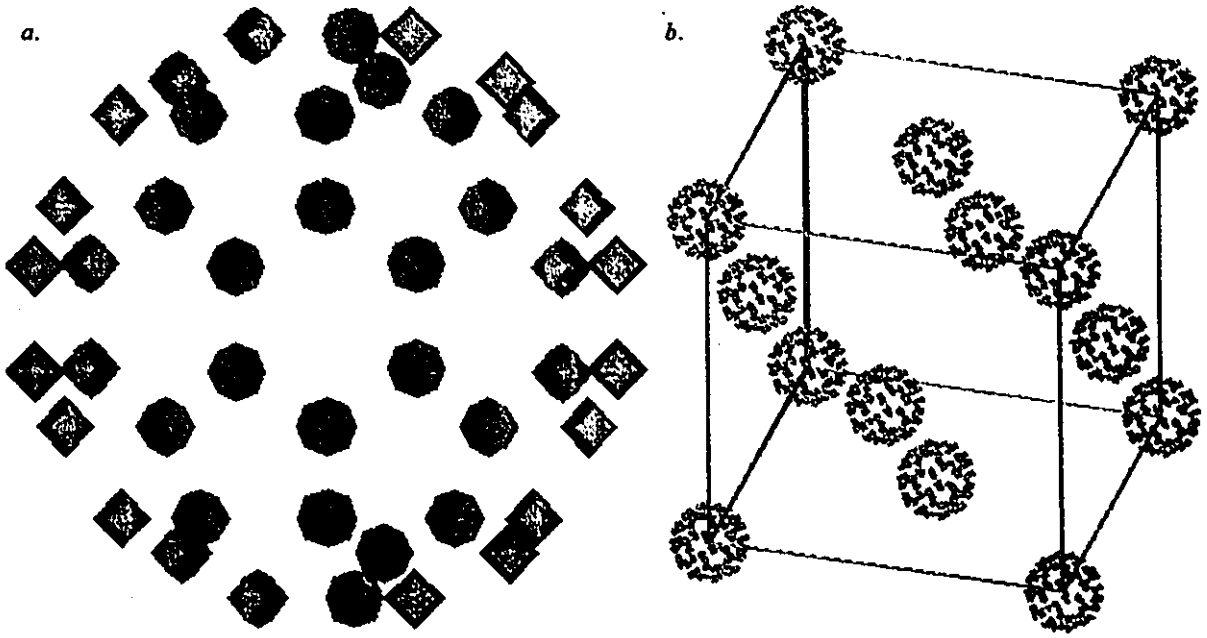

Figure 2.2 a. The soccer ball like molecule of C_{60}, composed of 12 pentagons and 30 hexagons and b. the FCC crystal the substance crystallizes in at room conditions. The space group of the crystal takes into account the point groups of both the molecule and the Bravais lattice (rotations, inversions, etc.) in these representations, the relative sizes of the crystal and the molecule are not correct. The actual structure is close-packed.

around an axis, rotation/reflection, rotation/inversion, reflection, inversion). When adding translational and combined translation-rotation operators, we generate 230 space groups, as opposed to the 14 (Bravais lattices) obtained when objects had spherical symmetry. For example, the diamond structure corresponds to a face-centred cubic (FCC) lattice with two carbon atoms at each point, located at (0, 0, 0) and (¼, ¼, ¼): the basis is a group of two atoms. Another much more complex example is that of a C_{60} crystal. C_{60} is a large icosahedral molecule (the carbon atoms are placed at the vertices of a soccer ball like shell composed of pentagons and hexagons) which has many internal symmetry properties, but has no translational properties and does not constitute a crystal on itself. This compound crystallizes in an FCC structure (at room conditions) with one such molecule at each point of the Bravais lattice. If the orientation of the molecule is fixed, then the complete space group must include that of the space group of the Bravais lattice and the point group of the molecule. However, if the molecule is spinning, the object (spinning molecule) has a spherical symmetry and the complete space group is simply that of the Bravais lattice.

The reason why there are a finite number of space groups is because we require that the crystal generated by a space group not have "voids", or areas of space which aren't spanned by translations through the lattice vectors. For example, in 2D, if we try to construct a cell that has a five-fold symmetry (a pentagon for example), we cannot fill the entire plane by translating the cell to other locations, without leaving gaps between adjacent cells. However, we can generate a unit cell which will span the entire plane and satisfy the Bravais lattice condition, but it loses its five-fold symmetry and falls into one of the 230 stated space groups (**Figure 2.3**). This example is one pertaining to the fact that only 1-, 2-, 3-, 4- or 6-fold rotations (rotations of angle $2\pi/n$ are called n-fold rotations) can lead to acceptable crystallographic point groups. When

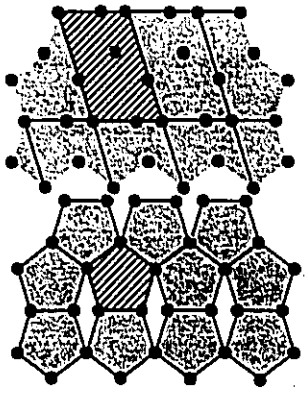

Figure 2.3 The attempt at making a five-fold symmetry unit cell in 2D

considering all possible operations that will generate a valid lattice, we obtain only 230 space groups.

There are several equivalent notations to describe a crystal structure according to its space group and point group, namely the Schoenflies notation and the International System. In the full international notation, a space group is characterized by a letter and point group-like notation. The letter represents the type of the Bravais unit cell: P for primitive, I for body-centred, F for face-centred and A, B or C for base-centred on the planes (bc), (ac) and (ab) respectively and R for rhombohedral. The symmetry code is based on the highest symmetry axis (usually chosen as $\vec{c}$ or $\vec{b}$ for the monoclinic system) and the symmetry operations relative to it. The following serve to identify the possible symmetry operations along specific axes: a number n (1, 2, 3, 4 or 6) represents an n-fold rotation symmetry, $\bar{n}$ represents an n-fold rotation and inversion symmetry, $\frac{n}{m}$ an n-fold rotation and mirror-reflection by a plane perpendicular to the rotation axis and so on for all the other operations. A short notation is commonly used, as an abbreviation when the full description is redundant: using a single letter usually indicate 2 or 2_1 (screw operation) over that letter. For example, *Pnma* is actually $P\frac{2_1}{n}\frac{2_1}{m}\frac{2_1}{a}$ and $P2_1/c$ is $P1\frac{2_1}{c}1$ which is a monoclinic space group so only axis y could have special a special symmetry. The Schoenflies notation does not involve any prerequisites for a primary axis, and each symmetry is assigned a specific letter, such as C_n for an n-fold rotation. This notation is the preferred one for vibrational spectroscopy (Raman or infra-red), whereas crystallographers usually use the international notation. A detailed description and derivation of space groups can be found in Burns [1990].

2.1.3 Computations Involving Crystal Structures

When dealing with crystal structures, we will need to calculate several properties of the crystal. First of all, it is necessary to calculate the volume of the unit cell. If $\{\vec{a}_i\}$ represents the basis vectors of the unit cell, then the volume is that of the parallelogram spawned by $\{\vec{a}_i\}$, i.e. $V = \vec{a}_1 \cdot (\vec{a}_2 \times \vec{a}_3)$. For the triclinic lattice (which is the general case), the volume expressed in

terms of the lattice parameters is

$$V = abc\sqrt{1-\cos^2\alpha-\cos^2\beta-\cos^2\gamma+2\cos\alpha\cos\beta\cos\gamma}, \tag{2.1}$$

where a, b, c are the lengths of the basis vectors and α, β and γ are the angles between the vectors ($\vec{b}$ and $\vec{c}$), ($\vec{a}$ and $\vec{c}$) and ($\vec{a}$ and $\vec{b}$), respectively.

To deal with the atomic planes in a crystal, we must introduce the reciprocal space of a lattice. The reciprocal lattice is the discrete set of all wave vectors $\vec{K}$ with the periodicity of the Bravais lattice. This means that we must have $e^{i\vec{K}\cdot\vec{R}} = 1$ for all $\vec{R} = n_1\vec{a}_1 + n_2\vec{a}_2 + n_3\vec{a}_3$ ($n_i \in Z$) in the Bravais lattice. Assume that $\vec{K}$ is spawned by a reciprocal space basis $\{\vec{a}_i^*\}$, such that $\vec{K} = k_1\vec{a}_1^* + k_2\vec{a}_2^* + k_3\vec{a}_3^*$ ($k_i \in Z$), then $\vec{a}_i^* = \epsilon_{ijk}\frac{2\pi}{V}\vec{a}_j \times \vec{a}_k$ is a suitable choice for a reciprocal basis, since $\vec{a}_i^* \cdot \vec{a}_j = 2\pi\delta_{ij}$. The equivalence between $\vec{K}$ and $\vec{R}$ in this formalism shows that the reciprocal lattice of a Bravais lattice is also a Bravais lattice whose reciprocal lattice is the original one (they are reciprocal to each other).

Now define a plane in the crystal by a vector normal to it, whose magnitude is the distance between two consecutive equivalent planes. Such a vector can be expressed in the reciprocal basis as $\vec{d} = h\vec{a}_1^* + k\vec{a}_2^* + l\vec{a}_3^*$ where h, k, and l are the smallest integers possible. The proof comes from the orthogonality of the reciprocal space to the direct space, and the reciprocity between the two (see Aschcroft [1976] for more detail). Integers *hkl* are known as the Miller indices of the plane, and will now be used to identify planes in a given lattice. One interesting fact about these indices, is that a given (*hkl*) plane intersects the three axes of the Bravais structure at positions h^{-1}, k^{-1} and l^{-1} .This was an *a priori* definition of the Miller indices, but the reciprocal space formalism is better suited for further plane related calculations, such as those involved in X-ray analysis. A zero Miller index means the plane is parallel to its corresponding axis. In general, when we use the notation (*hkl*), we actually include all the planes which are symmetrically equivalent to [*hkl*]. For example, in a tetragonal structure, (100) designates planes [100], [010], [$\bar{1}$00] and [0$\bar{1}$0]. In X-ray diffraction, we can measure the d-spacings of planes in a given structure, and it is necessary to determine the relation between the d-spacing of an (*hkl*) plane and the lattice parameters (direct or

reciprocal). In a general reciprocal space (no special symmetry), $Q_{hkl} = d_{hkl}^{-2}$ is given by

$$Q_{hkl} = h^2a^{*2} + k^2b^{*2} + l^2c^{*2} + 2hka^*b^*\cos\gamma^* + 2hla^*c^*\cos\beta^* + 2klb^*c^*\cos\alpha^*. \quad (2.2)$$

This expression reduces to simpler forms when special symmetries apply, and is the basis for the determination of the lattice parameters of a structure's unit cell.

2.2 X-ray Diffraction

2.2.1 Theory of X-ray Diffraction

2.2.1.1 General Description

As the name indicates, X-ray diffraction involves the diffraction of electromagnetic waves in the X-ray spectrum, which ranges in wavelength from roughly 125 Å to 0.06 Å (100 eV to 200 keV). Since diffraction of light by an object is most efficient when the light has a wavelength roughly the same size as the diffracting object, X-rays are perfect for diffraction by crystals, which usually have cell features of the order of a few angstroms. In a crystal, the X-rays scatter elastically off the atoms constituting it, or more specifically off the electrons around the nuclei, and interfere constructively under special conditions.

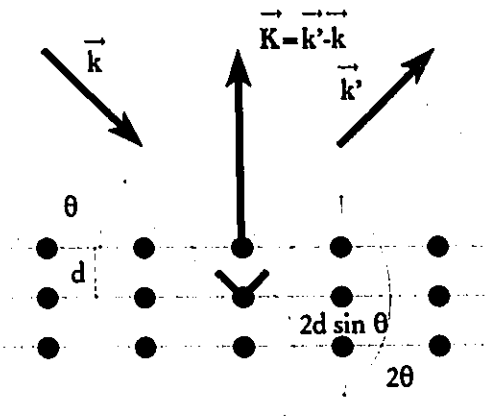

Figure 2.4 Illustration of Bragg's law, showing the requirements for diffraction off planes of atoms

Just as larger diffraction gratings diffract visible light in patterns representative of their

geometry, a crystal diffracts X-rays in a similar manner, yielding information about its structure from spots corresponding to maximized interference between diffracted beams. In crystallography, these are referred to as *Bragg reflections*. Consider **Figure 2.4** , depicting the constructive interference of monochromatic X-rays diffracting off atoms in a specific crystal plane. All the atoms in the planes will scatter a part of the beam quasi-isotropically, but because of their spatial configuration, the scattered beams interfere constructively to form a spot at a given angle θ. For any angle substantially different than θ, the scattered beams have random relative phases and will interfere destructively: only at the correct angle will there be a spot. Constructive interference of order m requires that the scattered beams be in phase at the observation point. Consider two atoms on the Bravais lattice with relative position $\vec{d}$ that diffract an incident beam with wave vector $\vec{k}$ in direction $\vec{k}'$ (with $k=k'=\frac{2\pi}{\lambda}$). The condition for interference, which requires that the path difference of two beams be an integral number of wavelengths, then becomes:

$$\begin{aligned} \delta &= \vec{d}\cdot(\hat{n}-\hat{n}') = m\lambda \quad , m \in \mathbb{N} \\ &\Rightarrow \vec{R}_{Bravais}\cdot(\vec{k}-\vec{k}') = 2\pi m. \end{aligned} \tag{2.3}$$

Since the atoms are located on the Bravais lattice, $\vec{d}$ is also a Bravais vector $\vec{R}_{Bravais}$ (that is, it can be expressed as an integer linear combination of the unit cell vectors). This relation, called the *Laue condition*, shows that constructive interference occurs when the change in wave vector $\vec{K}=\vec{k}'-\vec{k}$ is a vector of the reciprocal lattice, that is $e^{i\vec{K}\cdot\vec{d}}=1$. When considering the diffraction by a set of atoms in planes separated by a distance d, this condition reduces to *Bragg's law* which has a non-vectorial form:

$$\delta = 2d\sin\theta = m\lambda. \tag{2.4}$$

As represented in **Figure 2.4** , d is the spacing between equivalent planes in the crystal, λ is the wavelength of the monochromatic X-ray and θ is the angle of the incoming beam with respect to the diffracting planes, yielding a 2θ angle between the incident and the diffracted beams. A more detailed treatment of X-ray scattering by a crystal can be found in Ashcroft [1976].

2.2.1.2 Single Crystal X-ray Diffraction

In a single crystal, a particular diffracting plane only exists in a specific direction in the crystal, so it produces a single Bragg reflection, at an angle θ, in a plane perpendicular to the corresponding plane of atoms. It should be noted that the spatial intensity profile of the spot depend on the number of planes reflecting the beam, as well as the spatial configuration of the electrons around the atoms:

- if there is an insufficient number of planes to diffract, the spot will be broader, just as visible light diffraction by two slits gives substantially broader peaks compared to those obtained by more slits, since the angular width of the peak is inversely proportional to the number of slits. For angles close to θ, the scattering from a small amount of planes, does not produce a sufficiently random phase distribution to contribute to a complete destructive interference, hence resulting in a larger spot;
- if the diffracting atoms are not spherical, that is if the electron density is not isotropic, the diffracted beam will have an ellipsoidal (or some other non-circular) shape. The spherical distribution is equivalent to a point-source, whereas the ellipsoidal distribution will act as a slightly extended source, producing non-spherical wave fronts and a non-circular spot;
- the spot breadths also depend on the diffracting angle, due to geometrical factors involving the incoming beam's width and the diffraction angle.

Since all possible planes in the crystal produce a specific set of spots (corresponding to various orders, if they are visible), the whole pattern consists of a large number of spots corresponding

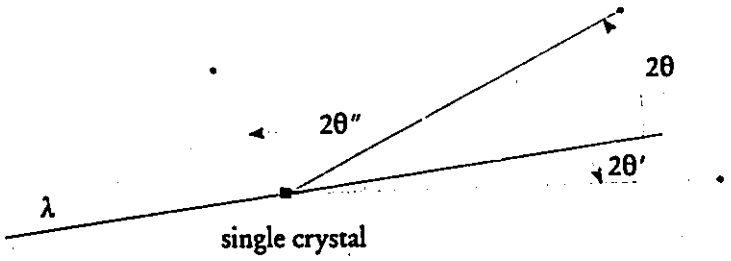

Figure 2.5 Bragg reflection from single crystal X-ray diffraction

to the different planes in the crystal, and changes according to the orientation of the crystal with respect to the incident beam.

2.2.1.3 Powder X-ray Diffraction

In high pressure research, it is uncommon and impractical to deal with single crystals: most samples are powdered, i.e. composed of many crystallites. When using powders, each plane that contributes for a single spot in single crystal diffraction can now be found in every randomly oriented crystallite, so a *cone* of light (or a *Debye ring* as it would appear when intersecting a plane) is actually diffracted at angle 2θ with respect to the direct beam (**Figure 2.6**). In this case, we can use Bragg's law to determine the angle of diffraction, since plane orientation is no longer relevant. Under ideal conditions, the diffraction pattern of a perfectly powdered sample is identical to that of a single crystal which is rotated in every possible direction during the observation, so the same factors that determined the shape of Bragg reflections also apply to Debye rings. Conversely, if there is an insufficient number of crystallites, one gets *poor powder averaging*: the diffraction cone is not complete because not all plane orientations are observed. Furthermore, the crystallites might not be randomly oriented, but aligned according to a *preferential direction*, or more specifically according to a distribution centred on a preferential direction. Once again the spots do not average out properly and, although complete rings are recorded, their relative intensities are different than expected because all the planes do not have the correct orientation to diffract. The two cases

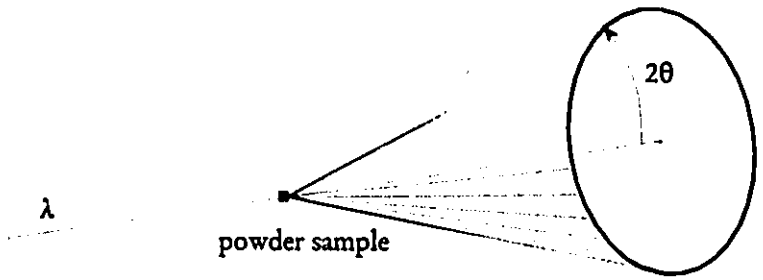

Figure 2.6 Debye ring from powder X-ray diffraction

are not to be confused and are distinct causes of similar effects on an integrated powder diffraction pattern: the observed intensities do not seem correct. *Preferred orientation* often occurs when the crystallites are platey or elongated which will cause them to stack along a common direction in a fibre like manner.

Already, one can see the incredible amount of potential information contained in the diffraction pattern. In practice, only intensities are measured and the phase of the diffracted beam is lost. This is important because the diffraction pattern appears to be centrosymmetric, even if the crystal is non-centrosymmetric. For this reason only 11 of the 32 point groups can actually be distinguished by X-ray diffraction. Also, the intensity must somehow be collected in a digitized form, in a specific geometry, etc., which contribute to the denaturation of the pattern. Fortunately, we are able to predict most of the experimental degradation and correct for it in simulated diffraction patterns, or try to reduce possible causes during the experiment.

In general, we use the following equation to calculate the intensity of the beam diffracted off a given (hkl) plane:

$$I(d_{hkl}) = aP_{hkl}m_{hkl}\left|\sum_{atoms\ j} S_j(d_{hkl})\right|^2 Exp(d_{hkl}), \qquad (2.5)$$

where the various factors are:

- a is a constant scaling factor which includes the relative concentration of the phase,
- $P(hkl)$, the preferred orientation factor, which depends on the angle between the (hkl) plane and a fibre-axis vector (the preferred orientation vector),
- m_{hkl}, the multiplicity factor, which also depends exclusively on the (hkl) plane and structure symmetries (its crystal system),
- $S_j(d_{hkl})$, the structure factor of each atom in the unit cell, which describes the scattering of the unit cell and depends on atomic species, positions and thermal parameters,
- $Exp(d_{hkl})$, the experimental contributions, which take into consideration all the factors which aren't specific to the sample itself, but rather the setup geometry, the X-ray

beam distribution, *etc.*, as well as possible sample absorption, which also depends on the geometry and method.

A detailed description of these contributions can be found in Appendix A. Some additional factors exist but are usually of minimal importance for the high-pressure spectra we obtain, since experimental conditions are far from ideal and the crystals are substantially strained and imperfect.

2.2.2 The Energy Dispersive X-ray Diffraction Method (EDX)

2.2.2.1 Description

For powder diffraction, the single requirement to have a plane diffract X-rays is given by Bragg's law, which is independent of the experimental setup. Traditionally, because it was practically unrealistic to have a "white" source of X-rays, a single wavelength λ was used to diffract at various angles θ off the crystal planes. More recently however, synchrotron sources have been used for the EDX method. As described in Appendix B, the storage ring of synchrotron particle accelerators (usually electrons or positrons) can be used to generate a very intense "quasi-white" X-ray beam with a usable bandwidth of 1 to 100 keV (12.4 to 0.124 Å range), which is perfectly suited for X-ray crystallography. Note that the EDX method can only be used for powdered samples because the detector is at a fixed position.

In this technique, the diffracting angle is kept constant, but the energy, or wavelength, of the beam has a continuous distribution: all planes eventually diffract in the right direction, but at different energies. By using an energy-resolving detector (an intrinsic Ge detector), we obtain a spectrum very similar to that generated by the traditional angle dispersive method. Since the measurements are done in energy rather than angle, we use a variation of Bragg's law, which involves the energy of the X-ray:

$$E = \frac{hc}{\lambda}, \quad m\lambda = 2d\sin\theta$$
$$\Leftrightarrow Ed = \frac{hc}{2\sin\theta} \text{ (for order 1) is a constant.} \tag{2.6}$$

With $\frac{hc}{2} = 6.1993$ (keV·Å). When Ed is calibrated (i.e., the angle is calibrated), we can find the d-spacing of a plane according to the energy of its diffraction peak:

$$d_{hkl} = \frac{Ed}{E_{hkl}}. \tag{2.7}$$

So large d-spacings are observed at low energy, just as they are observed at low angle in ADX measurements. Thus, in EDX experiments, Ed is the calibration constant (rather than λ), and E_{hkl} is the measured energy of the diffraction peak of the (hkl) plane..

The following sub-sections deal with the experimental setup for EDX diffraction, as well as the intensity contributions particular to EDX diffraction spectra.

2.2.2.2 Experimental Setup

We now describe the experimental setup designed to take EDX measurements on our samples. Although this particular setup (**Figure 2.7**) corresponds to the CHESS B1 station where we have done most of our experiments, it is somewhat standard. The setup is relatively simple, but the alignment of all the components requires a great deal of care. The beam coming from the synchrotron is collimated by a fine 15 to 200 μm Pb collimator which can be adjusted with 6 motors corresponding to three translations and 3 rotations. For 15 μm collimators, this procedure is very delicate. For our experiments, we have used two types of collimators. The more general kind is made by perforating a 5 to 10 mm thick Pb disk with a cone shaped hardened tool. Unfortunately, the size and shape of the hole cannot be precisely manufactured, so a different kind has been developed to replace them. It consists of two tungsten slits placed perpendicular to each other, effectively forming a square collimator.

When performing the experiments, we simply chose the collimator size most appropriate for the sample size (i.e., smaller). The DAC itself is located on the table using two kinematic positioners to allow us to take out and reposition the DAC precisely, to an accuracy better than 5 μm, if done carefully. The table on which the DAC resides can also be aligned using 5 motors, to control the translational motion and the titlting of the table. It is itself placed on a goniometer with a sturdy aluminum extension on which the Compton and detector slits and the Ge detector are mounted. The goniometer and the table on which it resides also have a motorized motion and tilting. Each slit can be opened or closed by a motor. A beam stop serves to absorb the direct beam which is not diffracted, to reduce the scattering in air and the radiation background in the experimental area. The Compton slit is placed as close as possible to the sample to cut off any scattering by the diamonds, and to define the angle of diffraction as well as possible. A detector slit is placed in front of the detector to cut off any extra scattering from the air. It also serves to define the diffraction angle. Both slits are made of parallel tungsten plates. Typically, the Compton slit is set around 100 or 150 μm and the detector slit is kept at 200 or 250 μm. A spectroscopy amplifier (CANBERRA 2020) and an MCA (multichannel analyser) are connected to the detector to recover the data on a computer. All the motors can also be adjusted from outside the experimental area, while the X-ray beam shutters are open and the area is unaccessible.

When using ruby ($Al_2O_3:Cr^{3+}$) as an optical pressure gauge, we must have an optical system to measure the wavelength of the R_1-luminescence line. For this purpose, a microscope reflective objective (Schmidt 15×, Ealing) is inserted to focus the light from an Ar^+ laser onto the ruby, and to recover the luminescence from the ruby and to redirect it to a ⅛ m spectrometer for spectral analysis. A yellow glass filter is inserted before the spectrometer to filter out the light from the unscattered part of the laser beam. The data from the spectrometer is viewed on a computer for rapid determination of the pressure, as is the diffraction pattern measured by the detector.

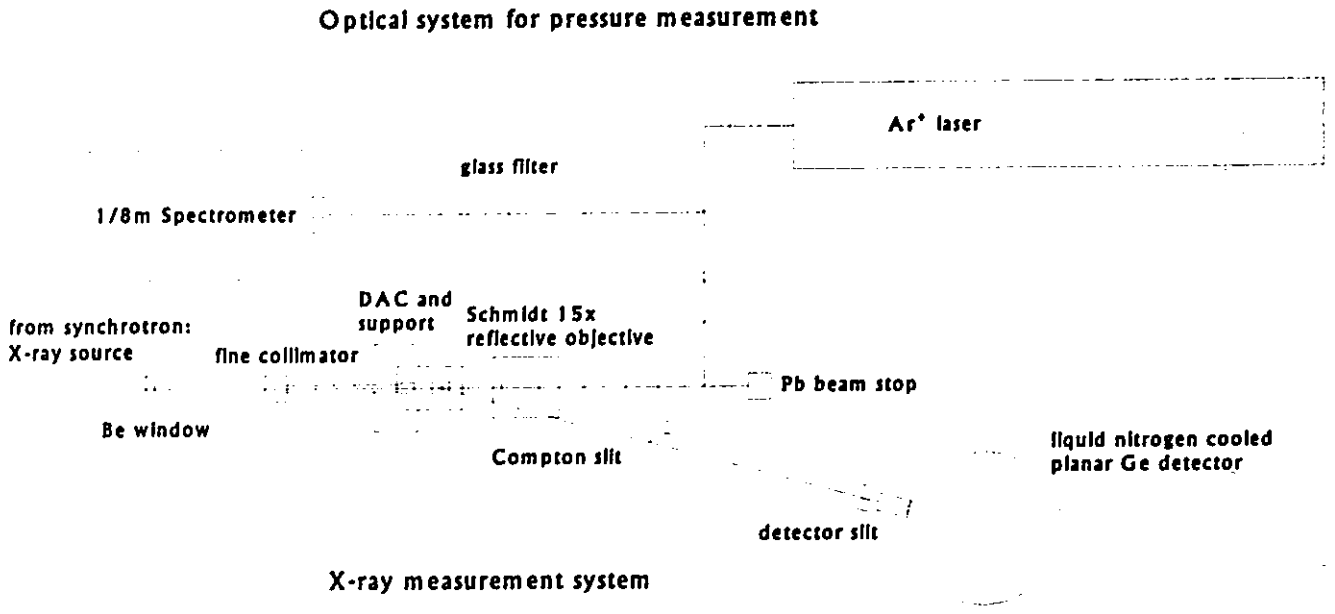

Figure 2.7 Experimental setup for energy dispersive X-ray diffraction measurements at the CHESS B1 station.

2.2.2.3 Energy Dispersive Specific Intensity Contributions

To determine the intensity of a diffracted peak, we use equation (2.5) for which we now interpret the *Exp(E)* term. Recall that this term represents the contributions specific to the method of measurement used.

2.2.2.3.1 Synchrotron Source Distribution

As detailed in Appendix B, synchrotron radiation is distributed on a continuous spectrum of energies. For typical sources with a simple *bending magnet* (like the CHESS B1 line), the critical energy is around 10 keV, producing most of the photons between 1 keV and 80 keV. Additionally, the synchrotron can include an insertion device such as a *wiggler*, which is composed of several magnets generating an oscillating field perpendicular to the electrons orbit, making the electrons themselves oscillate at high frequencies. These oscillations contribute to a motion with a much smaller bending radius than that of the orbit itself, resulting in a higher critical energy, in the 20 to 30 keV range. As a result, the source spectrum

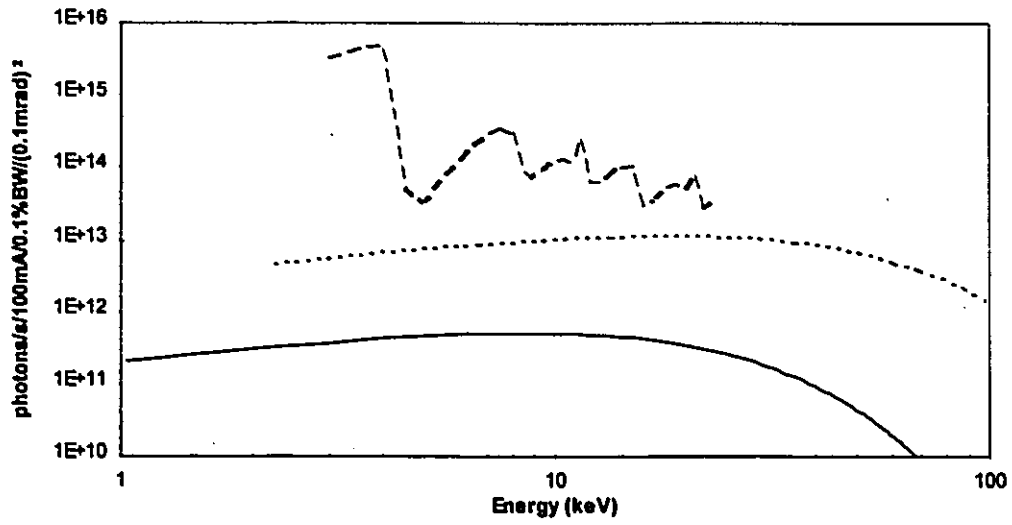

Figure 2.8 Brightness of the CHESS X-ray sources (photon flux for a 100 mA current, 0.1% bandwidth, in a solid angle (0.1 mrad)^2), with from top to bottom the 123-pole undulator, the 25-pole wiggler (ε_c = 22.4 keV) and the hard-bend magnet (ε_c = 10.3 keV)

is roughly 50 times brighter (at 20 keV) than for bending magnets. Yet another more recent insertion device to produce high intensity beams is an *undulator*. Like a wiggler, the undulator makes the electrons oscillate rapidly, but at a frequency where the radiation produced at each oscillation is in phase for a given wavelength, so the total radiation produces a coherent, very intense beam at that energy, acting in a sense like an X-ray laser. Photons corresponding to other energies are also produced, but at some energies, the interference is destructive. Consequently, the spectrum is very irregular, containing peaks and valleys. The brightness of the source is another order of magnitude larger than from a wiggler device, but it cannot be used for EDX experiments because the spectrum is not smooth enough: within the spectrum itself, there are orders of magnitude difference between different energies. The undulator is, however, perfectly suited for ADX experiments, when using an X-ray monochromator is used to produce a monochromatic beam. **Figure 2.8** illustrates the spectra produced using the three methods cited, as measured at the CHESS facility (the undulator is not permanent but was tested in August 1994). In comparison, a conventional rotating anode source produces a spectrum at best 60 times dimmer than that of a syncrotron with a bending magnet.

2.2.2.3.2 Sample and DAC Absorption

Just as any other type of light which is absorbed by matter, materials have an X-ray absorption coefficient which depends on its energy. In general, the absorption *A(E)* of X-rays in matter is an exponential function of the thickness *t* of the sample and a linear absorption coefficient μ:

$$A(E) = 1 - e^{-\mu t}, \Rightarrow T(E) = e^{-\mu t} = e^{-\frac{\mu}{\rho}\rho t}. \qquad (2.8)$$

where *T(E)* is the transmission coefficient and $\frac{\mu}{\rho}$ is called the mass absorption coefficient, which for the range of energies we work at is simply due to photoelectric absorption. The absorption coefficient contains certain sharp features near the electronic energies in the material. When the energy of the X-ray is equal to that of an electronic transition (usually

from the inner K or L shells), the absorption coefficient increases sharply because the excitation of electrons from that shell becomes possible, then decreases as a power law until it reaches another shell energy. As an example, **Figure 2.9** shows the absorption coefficient of gold (Au), where the various K and L edges are clearly visible.

When set up at an angle 2θ, the thickness of the up-stream diamond anvil is just its height h, whereas the path through the downstream diamond is $\frac{h}{\cos\theta}$. Absortion in the sample is different since every crystallite along the direct beam can diffract at the given angle 2θ, so the average transmission inside the sample of thickness t must include all possible paths which produce that diffraction:

$$\begin{aligned}\langle T\rangle &= \frac{1}{t}\int_0^t e^{-\mu\left(x+\frac{t-x}{\cos 2\theta}\right)}dx \\ &= \frac{1}{\mu\beta t}e^{-\frac{\mu t}{\cos 2\theta}}\left(1 - e^{-\mu\beta t}\right), \text{ where } \beta = 1-\frac{1}{\cos 2\theta} \\ &= T_0\left(\frac{e^{\mu\beta t}-1}{\mu\beta t}\right), \text{ with } T_0 = e^{-\mu t}.\end{aligned} \tag{2.9}$$

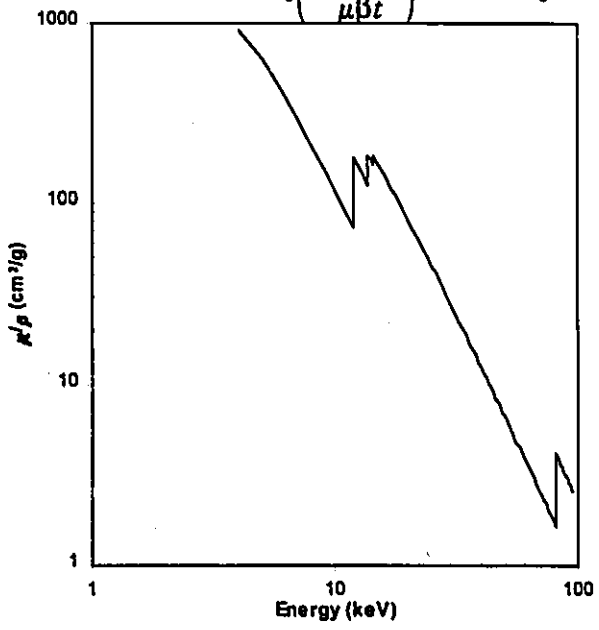

Figure 2.9 Mass absorption coefficient of Au, showing the K (88 keV), L_I (14.3 keV), L_{II} (13.7 keV) and L_{III} (11.9 keV) edges which create discontinuities.

It is easy to see that for $2\theta=0$, $\beta=0$ and we recover the normal transmission T_0, for which the thickness is simply t. Some other absorption contributions can be included, other than that of the diamonds and the sample, such as absorption by the 1 mm thick Be window that keeps the synchrotron tube sealed and the air travelled through from the Be window on the synchrotron to the

detector. However, these contributions are negligible or irrelevant to us, because Be is essentially transparent to X-rays, except at very low energies (less than 5 keV), and air has such a low density that in comparison to other factors, it is imperceptible (**Figure 2.11**).

2.2.2.3.3 Detector Efficiency and Resolution

Two other contributions to the observed spectrum come into account when collecting the data using an energy sensitive detector: the detector efficiency (its capacity of actually detecting an incoming photon) and its resolution (the degree of uncertainty on the observed photon's energy). Solid state detectors are widely used when using synchrotron radiation because of their good energy resolution and high count rate. The one we used is a high purity planar Ge detector, presenting the best resolution of all the solid state detectors, with a resolution of around 135 eV at 5 keV. Basically, the detector efficiency and resolution are governed by the photon-electron interaction processes: at energies lower than 70 keV, the detection process is dominated by photoelectric absorption; Compton scattering plays an increasing role for higher energies. The high precision electronics are set up to accept and detect each photon individually. In the detection process, an electron is liberated from an atom and given a kinetic energy equivalent to the photon energy, minus its binding energy. This freed electron then looses its energy by producing electron-hole or electron-ion pairs

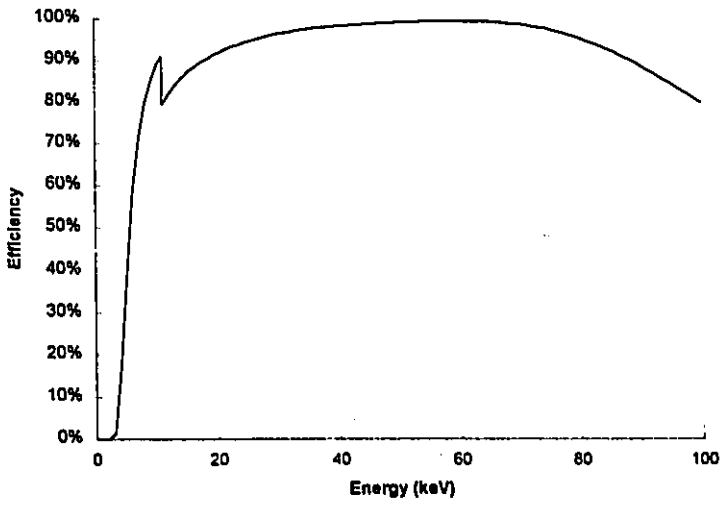

Figure 2.10 The efficiency curve of a high purity planar Ge detector (5 mm thick). Notice the absorption due to the Be window on the detector (below 10 keV) and the Ge K edge (11.1 keV) above which escape peaks reduce the efficiency. At energies higher than 50 keV, the efficiency is given by the absorption in the Ge.

which are collected and counted as a current intensity pulse. To avoid trapping of the electron or hole and to avoid counting thermally excited electrons, the detector is kept at 77°K at all times. When the electron is freed from the atom, X-rays are emitted when the atomic shell electrons rearrange themselves. These photons also contribute to free another electron which also produces electron-hole pairs which are counted. The complete energy of the incoming photon is thus converted to a charge proportional to that energy. Using a preamplifier, an amplifier and a multichannel analyser, the data is sent to a computer for real-time observation of the spectrum. A particular phenomenon known as an *escape peak* is produced when one of the fluorescence X-rays escapes the detection, so the energy balance is not preserved and the observed energy for the peak will be incorrect. The intensity of this observed peak depends on the fluorescence yield of the transition from which the escaped photon was produced. For germanium, these peaks correspond mostly to the K_α and K_β transitions and correspond to a 9.89 and 11.0 keV difference, respectively. The intensity of these escape peaks decrease from 16% of the "real" peak's intensity at 11.1 keV (energy of the Ge K edge) to 0 with increasing energy (at 50 keV, the ratio has dropped to ~2%). However, when there are very intense peaks, the escape peaks must be accounted for, so that they are not assumed to be diffraction peaks. For the photoelectric detection, the efficiency of the detector is simply its absorption, which, for Ge is nearly constant between 20 and 80 keV. A 1 mm Be window absorbs most photons at energies less than 5 keV, impeding the detection process. The resolution of the detector also depends on the energy: the FWHM of a mono-energetic beam will be proportional to the square-root of its energy, with a value around 150 eV at 5.9 keV, depending partially on the timing setting of the detector electronics. This means that the intrinsic resolution of the detector at 30 keV is $\frac{\Delta d}{d} = \frac{\Delta E}{E} \approx 10^{-2}$, for any value of Ed.

2.2.2.3.4 Compton Scattering

One contribution to the spectrum which is not directly involved in the diffraction peaks intensities but rather in the background is *Compton scattering*. A photon can scatter

elastically off an electron in the diamonds, the sample or the air by giving it some energy, without necessarily ionizing an atom. The outgoing photon energy is then slightly shifted according to the scattering angle, but this shift is imperceptible at the working energy resolution, so it doesn't affect the positions or widths of the peaks. However, these scattered photons produce a significant amount of background which can be partially eliminated by using a *Compton slit* in the setup. By inserting this slit, we effectively cut off all scattering from electrons which is not in the desired diffraction path. This is especially important when we have diamonds on either side of the sample as they produce an important background scattering. Since the cross-section of Compton scattering does not vary much on the range of the energies observed, a background proportional to the synchrotron spectrum is measured. Unfortunately, we cannot get rid of all Compton scattering with these slits because the scattering produced by electrons in the 2θ path cannot be filtered out from the diffraction signal.

2.2.2.3.5 Combined Experimental Factors

The complete *Exp(E)* factor can now be plotted to view to what value we must set *Ed* to get the most information possible in the best range possible. One should also try to avoid having diffraction peaks overlap with fluorescence lines from the sample, or K edges which absorb most of the photons around those energies, effectively eliminating any diffraction signal in those regions. **Figure 2.11** represents a plot of all the experimental factors that enter into account when calculating diffraction peak intensities, which shows that for the given synchrotron source (CHESS B1), the useful energies (> 10% of maximum intensity) range from 10 to 55 keV.

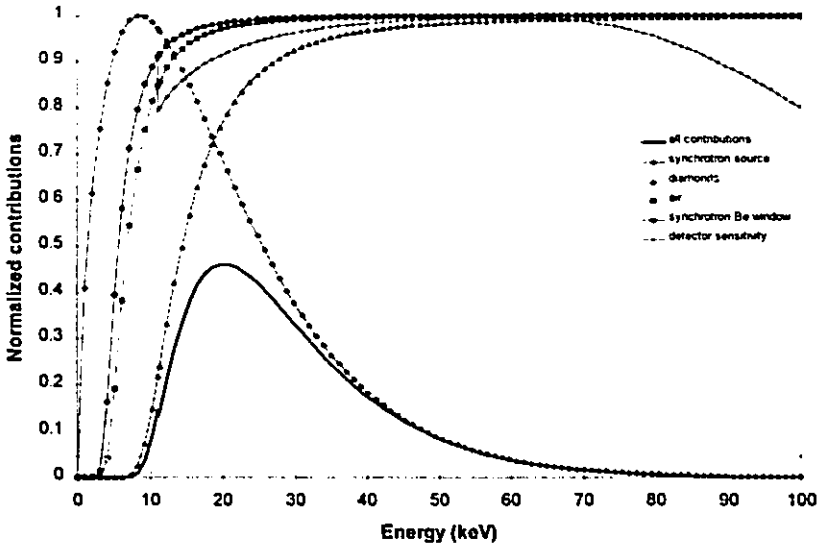

Figure 2.11 The various experimental intensity contributions for EDX diffraction measurements. The bold solid line represents the product of all the contributions, which represents the useful beam spectrum. The dashed line represents 10% of the maximum intensity, showing the potential range where a maximum number of peaks should be located. In general, because of statistical fluctuations in the data, anything outside this range is poorly resolved from the background.

2.2.2.4 *Ed* Calibration Measurements

Even though the detector is setup on an accurate goniometer, we must take a reference diffraction spectrum to calibrate *Ed*. For all our EDX experiments, we used a gold foil (polycrystalline sample). It is important to note that if the slits are too wide, the measure of the position of the sample is compromised, because the uncertainty on 2θ is very large, as will be the uncertainty on *Ed*. The slits must therefore be closed to have a sufficient restraint on the sample position in the X-ray beam so that it can be reproducible and that we could place the gold foil at the same position. They must not however cut off too much the diffraction signal. To position the sample or the gold foil, a scan in the direction of the direct beam is performed, to locate the position where the diffraction is largest. The signal itself consists of a

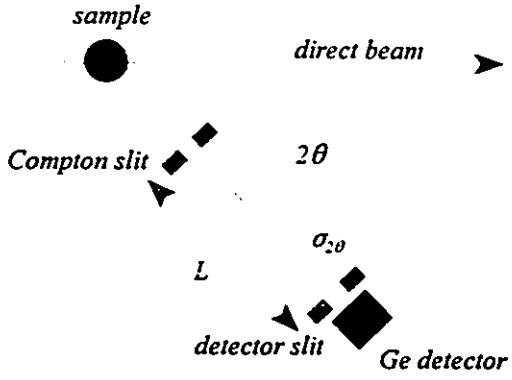

Figure 2.12 Schematic representation of the Compton and detector slits, and how they relate to the uncertainty on 2θ.

peak with a very large tail which corresponds to the Compton scattering off the diamonds. If the gold foil and the sample are not placed at the same position, or if the sample is moved during the experiments, then the spectra recorded are not compatible with the calibration, and consequently erroneous d-spacings for the observed peaks are calculated. With the Compton slit/detector slit geometry as explained previously, we find that the angular uncertainty is $\sigma_{2\theta} = \frac{c+d}{L}$, where *c* and *d* are the widths of the Compton and detector slits, and *L* is the distance between the slits (**Figure 2.12**). Typical values for c and d are 100 and 200 μm respectively and L is 50 to 70 cm, giving $\sigma_{2\theta} \approx 5 \cdot 10^{-4}$. The uncertainty on Ed can be calculated based on the uncertainty on 2θ: $\sigma_{Ed} = Ed\frac{\sigma_0}{\tan\theta}$, which gives $\sigma_{Ed} \approx 100$ eV for $Ed = 50$ keV·Å ($2\theta \approx 14°$). We can also get this uncertainty by fitting the calibration spectrum's peaks and determining the average observed *Ed* and finding its standard deviation. It must be taken into account when calculating the uncertainty on the d-spacing of an observed peak reflection, on top of the uncertainty on the energy from to the fitting of the data to a specific profile shape function:

$$\sigma_d^2 = \left(\frac{\sigma_{Ed}}{E}\right)^2 + \left(\frac{Ed\,\sigma_E}{E^2}\right)^2. \qquad (2.10)$$

This uncertainty on d will eventually be used as the weight for the peak in a structure fit, and will serve to determine the uncertainty on the lattice parameters.

2.2.3 The Angle Dispersive X-ray Diffraction Method (ADX), Using Imaging Plates (IP)

2.2.3.1 Description

Contrarily to energy dispersive diffraction, angle dispersive diffraction measures the diffraction of a single wavelength X-ray beam incident on the sample, on a range of 2θ angles. To determine the position of diffraction peaks, we rely on Bragg's law, to get the d-spacing of an observed peak, or to evaluate the angle, based on a known d-spacing. Imaging plate technology is very recent, dating from the past ten years, and has proven much more useful than traditional diffractometer geometries for several reasons. Essentially, the imaging plate is a phosphor coated plate measuring around 200×250 mm^2 which is used to temporarily store the complete diffraction pattern before the intensities are read and digitized by a scanning device. The plate is inserted perpendicularly to the direct beam so that it intersects the diffraction rings we want. When excited by X-rays, the phosphor is put in an excited state. The IP is then placed inside a scanner, where a laser is used to illuminate a pixel and record the induced luminescence, therefore measuring usable intensities. Since we use powdered samples, the diffraction pattern consisted of rings which intersect the IP in the form of ellipses if the IP is not perfectly perpendicular to the direct beam. Intensities had to be integrated along the ellipses in order to convert the data to a usable 2θ-intensity format. When integrating on complete rings, any poor powder averaging gets corrected. This was accomplished using a IPA, a program written by myself and described in Appendix D.

2.2.3.2 Angle Dispersive Specific Intensity Contributions

Because we obtain the complete Debye rings on the IP, there is only one experimental factor to consider when calculating intensities: the polarisation factor, which represents the

intensity of the scattered radiation as a function of angle. As seen in Appendix A, it is given by $p \propto \cos\theta$. Recall that the Lorentz factor is solely due to the fact that only a part of the Debye ring is actually measured. If desired, one might also consider the absorption in the air, which would be given by $A = 1 - e^{-\mu_{air}\frac{L}{\cos\theta}}$, and through the downstream diamond, if the sample is in a DAC. These contributions are usually negligible at the wavelength we used (0.4079 Å which is 30.4 keV).

It should be noted that because the monochromator used to filter the radiation to a single wavelength works by diffraction off a high purity Ge or Si crystal, there may be some higher order wavelength corresponding to $\lambda/2$ and $\lambda/3$. In our case, the (111) plane of a Ge crystal is used, so there will be no $\lambda/2$ component. The $\lambda/3$ component is naturally very weak, and the scattering power of the materials is usually much smaller at such high energies, so it was never observed. In fact, higher order diffraction from our sample was not observed either, even though this one should be more intense than the $\lambda/3$ diffraction. Also, the shape of the incident beam profile due to the monochromator could have been of importance if we had very high quality data, but it was of no concern in our experiments.

2.2.3.3 Experimental Setup

Figure 2.13 represents a typical setup for an ADX experiment with an imaging plate. The setup of the DAC or any sample is identical to the one for EDX experiments, but the Ge detector is replaced by an imaging plate which is aligned with the direct beam. Also, a much smaller lead beam stop was used to avoid the direct beam to saturate the plate, without absorbing it completely, since the spot where the direct beam intersects the plate is required to get an accurate integration of the rings. **Figure 2.14** shows the diffraction image of HfO_2 at ambient pressure, inside a Merill-Basset type DAC. The base of the image is cut off by the aluminum table on which the DAC is placed. Typically, when working at 0.4079 Å, we would obtain diffraction rings for angles 2θ up to 35°. The FUJI BAS2000 scanner which was

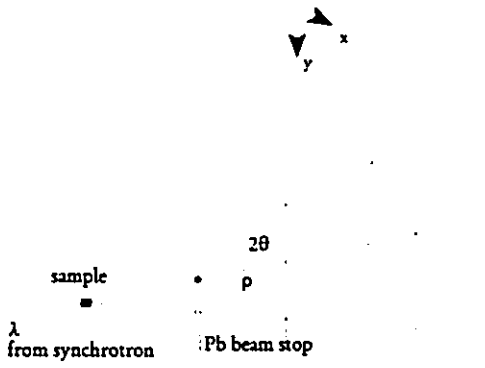

Figure 2.13 Schematic experimental setup for ADX experiments using an imaging plate.

used to read the information from the imaging plate was located in another room and linked to a computer. The data generated represent a 2560×2048 pixels^2 image of 10 MB. The intensities are stored in a 10 bit (0 to 1024) logarithmic format, $I_{stored} = 256 \log_{10} I_{obs}$, giving a dynamic range of 10^4 for the observed intensities.

2.2.3.4 Calibration Measurements

To integrate the data into a 2θ profile, a precise measurement of the sample-to-plate distance is required (the pixel dimensions are known: 100 μm×96 μm). Unfortunately, because the plate itself is in a metal frame, such an accurate measurement is impossible. Instead, we must once again use a known material and take a calibration spectrum, in this case an NBS Si calibration powder. Usually, for each sample or pressure, two spectra are taken at different sample-to-plate distances, so once we fix these two plate positions, there is no need to retake a calibration spectrum every time we move the sample: simply take a spectrum for each distances. Using the position of a peak on each plate, we can get the sample-to-plate distance for either plate position. This method is preferred over repeating calibration because we could

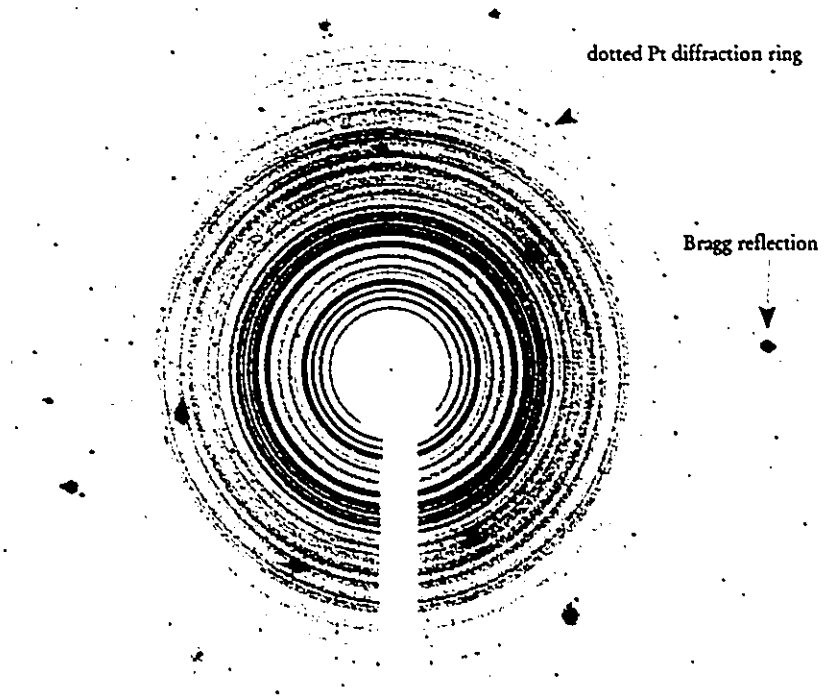

Figure 2.14 Imaging plate ADX diffraction pattern of HfO_2 at ambient pressure in a Merril-Bassett type DAC with a Be anvil support. The sample to plate distance is 14.70 cm, and λ=0.4079 Å. The very intense spots correspond to Bragg reflections from the diamond. Pt is used as a pressure calibrant, and due to its very small quantity, there is poor powder averaging resulting in dotted rings, whereas the HfO_2 produces continuous rings. The Pb beam stop is inserted on an Al rod whose "shadow" can be seen on the image. The contrast has been set to improve the visibility of the rings.

not place the calibrating sample exactly at the same position: a measure of the distance to within 10 μm is necessary for reliable data. Another advantage of this method is that we can vary the resolution of the experiment according to our needs. For very good (unstrained) samples, the diffraction lines have an angular divergence roughly equivalent to the width of two pixels, for a medium (20-25 cm) sample-to-plate distance. By setting the plate closer, we get a wider angle range, but loose resolution because some peaks might overlap on a single pixel. At greater distances, we get a smaller angular range, but an increased resolution, where several pixels will serve to define a peak. A typical sample-to-plate distance is 15 cm, for which

pixels 100 μm$\times$100 μm represents an angular resolution $\sigma_{2\theta} = \frac{w}{\rho}\cos 2\theta$ or a resolution on the d-spacing of $\frac{\sigma_d}{d} = \frac{\sigma_\theta}{\tan\theta} \approx 2{\cdot}10^{-3}$. By setting the plate at 25 cm, we decrease that to $\frac{\sigma_d}{d} \approx 10^{-3}$ for d = 1.7 Å. See the description of IPA for more details on the calibration procedure.

2.2.4 Comparison Between the EDX and ADX Methods

As we have seen, both methods should provide suitable results for accurate refinement of the structure. However, because the EDX spectra have a substantial and irregular background and that there are many intensity contributions which are very approximative, the actual intensities of calculated peaks would not sufficiently match the observed intensities of peaks to let us perform atomic position refinement. We could only do structural parameter refinements, that is the a, b, c, α, β, and γ lattice parameters. The space group of the sample had to be known beforehand, as well as the indexing of the peaks. For high pressure data, the peaks are usually so wide that an accurate and irrefutable indexing scheme is practically impossible. We could only guess what the Miller indices of the peaks could be and see if that structure produces the correct peaks. There are several computer programs which do this, but even then, we have to specify a crystal system. For a given sample, there is very little possible improvement of the number observed of peaks and their resolution, which makes the EDX method improper to determine precisely a new structure. It is very well suited however for higher symmetry structures, where the peaks are well resolved yet in sufficient amounts to index. This was usually not the case with our samples which have monoclinic and orthorhombic cells. EDX is, however, roughly 2 to 4 times faster than the ADX method to acquire the data, when using the same source. The ADX method gives more leeway to improve the experiment, as described previously, and gives much more predictable intensities than EDX measurements. In particular, remember that the intrinsic resolution of the ADX method is roughly an order of magnitude better than that of the EDX method. Also, to be able to see the whole diffraction ring enables us to see the degree of crystallinity of the sample,

if there is poor powder averaging. Recall that in the EDX method, a fixed arc of the complete diffraction ring is observed. As for the analysis of ADX data, the same prerequisites apply, that is knowing the space group of the structure. Because of the reliability on peak intensities, we can use Rietveld refinement to get much more information than with EDX data. Essentially, Rietveld refinement optimizes a number of parameters to fit a calculated diffraction pattern to the observed one. Several computer programs are available to do this. By seeing exactly to what degree a structure is well fitted, we can compare complete patterns, not just d-spacings and approximate intensities. All these reasons make ADX measurements with imaging plates the best method of the two. However, the experimental procedure to align and produce good ADX spectra is much more complicated, as is the data analysis, so EDX, with its real-time display and readily usable data remains a very important tool to determine lattice parameters and equations of state.

2.3 Raman Spectroscopy

2.3.1 The Raman Effect

The Raman effect was first discovered in 1928 by Raman while studying the emission spectrum of several liquids when irradiated by a mercury lamp. Since then and especially since the advent of the laser in the 1970's, many physicists and chemists have used Raman spectroscopy to identify vibrational and rotational modes in solids and liquids.

Unlike infrared spectroscopy in which the vibrational and rotational modes in a compound are identified by the absorption of light with the correct energy, the Raman effect produces the emission of light at frequency shifts characteristic of the sample.

In our case, there are no freely rotating molecules in the sample, so only vibrational modes (phonons) will be dealt with. Nearly the same treatment can however be applied to rotational modes of a molecule. A treatment of the Raman effect can be found in several solid state or quantum mechanics text books [Kittel 1986, Aschroft 1976, Cohen-Tannoudji 1977].

2.3.1.1 Photon-Photon Interaction Model

Consider a solid which has vibrational normal modes of frequencies ω_i and wave vectors $\vec{k}_i$. When irradiated by light with frequency Ω and wave vector $\vec{K}$, the scattered light spectrum contains the elastic Rayleigh scattering component of frequency Ω plus additional emission lines of frequencies $\Omega \pm \omega_i$, which are called the anti-Stokes (+) and Stokes (-)

Figure 2.15 The scattering of a photon with *a.* absorption of a phonon (anti-Stokes) and *b.* emission of a phonon (Stokes). In both cases n is the refractive index of the material.

components arising from inelastic scattering of the photon. Essentially, they correspond to the absorption of a phonon, increasing the photon energy, and the creation of a phonon, which decreases the photon energy. The energy and momentum conservation laws for such a process are thus

$$\begin{aligned} \hbar\Omega' &= \hbar\Omega \pm \hbar\omega \\ \hbar n\vec{K}' &= \hbar n\vec{K} \pm \hbar\vec{k} \end{aligned} \tag{2.1}$$

where n is the refractive index of the sample. The conservation of momentum is not possible across a Brillouin zone because the wave vector of the photon is much smaller than the size of a Brillouin zone. **Figure 2.15** illustrates the Raman scattering processes graphically. By analysing the light scattered by the sample with a spectrometer, it is thus possible to identify the vibrational frequencies of the material. Once again, the same picture applies to rotations of a molecule in a solid or a liquid.

2.3.1.2 Photon-Electric Dipole Model

We will now give a more detailed explanation as to what happens when a photon interacts with matter. Consider two atoms, interacting much like a harmonic oscillator would. If they are not identical atoms, they form an electric dipole which will react with the incoming radiation. The elastic mode of interaction (Rayleigh scattering) involves the vibration of the molecule at the same frequency as the incoming photon, producing the emission of light with that frequency. If the molecule is vibrating, then the dipole will vibrate under the effect of its intrinsic oscillation mode, and under the effect of the photon's oscillation. The dipole motion is then described by the product of a $\cos(\Omega t)$ term and a $\cos(\omega t)$ term. The resulting motion is thus the sum of a $\cos((\Omega+\omega)t)$ and a $\cos((\Omega-\omega)t)$ term[†]. This shows that the light emitted from the oscillation of the dipole will contain terms with frequencies $\Omega\pm\omega$. The same is applicable to a more general phonon, for which the collective dipole will emit light at those frequencies.

It is also possible to observe the Raman spectrum of such a diatomic molecule even when both atoms are of the same species and if there is no static electric dipole, in which case the mode is inactive in infrared spectroscopy. In general, the polarizability of the molecule depends on the distance r between the atoms. When vibrating, this induces an electric dipole whose response (susceptibility) varies in time with frequency ω, resulting in the same phenomenon as previously described. Raman spectroscopy is thus a tool which differs from infrared spectroscopy, enabling the observation of additional modes. It is also possible that some infrared modes not be visible in Raman spectroscopy because of the conservation laws and the phonon characteristics.

[†]Recall that $2\cos(a)\cos(b) = \cos(a+b) + \cos(a-b)$

2.3.1.3 Shape of a Raman Line

As stated previously, the emitted light contains frequency shifts relative to the incident photon frequency. Experimentally, the width of the Raman line is always larger than the intrinsic spectral width of the exciting laser, indicating that it has a finite width and peak profile shape. This is expected, since these shifts correspond to the normal modes of vibration in the solid. The power spectrum of a damped harmonic oscillator in response to an external frequency is known to be of a Lorentzian peak shape, with a FWHM which depends on the dampening constant. It is thus normal to observe the same behaviour in Raman spectroscopy and to identify the Raman peak profiles as Lorentzian.

2.3.2 Experimental Setup

In order to perform Raman spectroscopic measurements, we used an *in situ* micro-Raman facility. In consists, in a cloaked room, of a vibration dampening optical table on which the complete optical system is arranged. **Figure 2.16** represents a layout of the experimental area.

2.3.2.1 The Incident Laser Beam

As an excitation source at a reference wavelength, we used a Lexel Model 95 Ar^+ ion laser, which can be tuned to several wavelengths, most commonly 514.5 nm and 488.0 nm. To filter out any possible plasma (non-lasing) lines which could interfere with Raman peaks, the beam passes through a 1/10 m monochromator, acting as a spectral filter. The beam from the laser is polarized vertically, so a polarization rotator is also added to provide alternative linear polarizations. In our experiments, we did not perform any polarization specific experiment, so it was kept vertical since the beam splitter in the microscope was most efficient for that

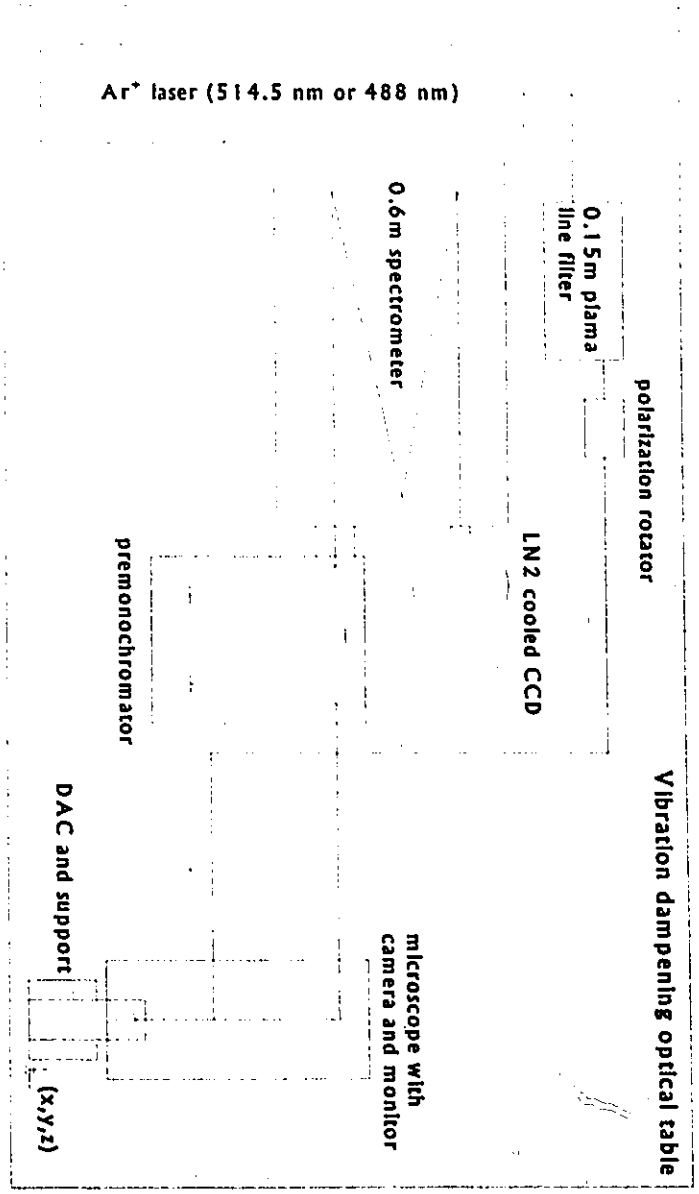

Figure 2.16 Schematic diagram for Raman spectroscopic experiments.

setting. Several high reflectivity coated Al mirrors were then inserted to direct the beam into the microscope. After the beam splitter and other optics in the microscope, the several mirrors, the beam polarizer and the plasma line filter, the power reaching the sample is around 10% of the initial laser setting. A specific measurement of the power at the sample depends mostly on the width of the slit on the spectral filter, the polarization of the beam and the objective used.

2.3.2.2 The Microscope and DAC Support Stage

An Olympus BH-2 microscope is used to focus the laser on the sample (or the ruby) and to recover the emanating (scattered) light which is subsequently analysed using a spectrometer. To position the sample under the microscope, a color CCD video camera is linked to a monitor with which the focus can be set. The monitor also helps to determine the color, texture or other optical features of the sample. In most cases, it can also be used to inspect, e.g., determine when the pressure medium inside the DAC solidifies. Several objectives can be used to focus the beam, ranging from 5× to 100×. Unfortunately, the 50× and 100× Olympus objectives have very short (< 1 mm) working distances, so they cannot be used with the DAC. Instead, when using the DAC, two long working distance (15 mm in air) Leitz objectives (10× and 25×) are used. An additionnal 5× objective is also used in other circumstances and for coarse alignment. One unfortunate consequence of taking measurements inside the DAC is that an important part of the signal is lost. Because of the difference in numerical aperture of the two types of objectives, the signal ratio obtained from the Leitz objective to the Olympus objectives is roughly 1:100. It is therefore very difficult to measure weak signals inside the DAC, and it therefore requires much longer integration times.

Because the DAC and its lever are very bulky, an auxiliary support stage was built to accomodate it. It is positionned in front of the microscope and consists of a stage with coarse and fine vertical adjustment, as well as fine lateral and forward adjustments.

With this setup, a back scattering geometry is used, meaning that the incident beam

and the measured signal are perpendicular to the DAC. Because of the high refractive index of diamond (n ≈ 2.4), the different interfaces introduce important losses due to reflection (air-diamond, T ≈ 83%), and a Brewster angle geometry would be preferred. A setup for this geometry was not completed in time to perform the experiments.

2.3.2.3 The Spectrometer and CCD Detector

The light recovered by the microscope is focused on the entrance slit of a Jobin-Yvon S3000 spectrometer which is used to measure the scattered light spectrum.

As a preliminary filtering process, the light passes through a vertical premonochromator consisting of two 1800 groves/mm holographic diffraction gratings working in a subtractive mode, which has for effect to filter the beam in a specified bandpass and then refocus it before it enters the spectrometer. This greatly inhibits any stray laser light (at the reference wavelength) from entering the spectrometer and being recorded. Additionally, it reduces the amount of light entering the spectrometer, which lessens the amount of stray light produced inside the spectrometer due to dispersion in air and on the diffraction gratings.

The spectrometer itself is composed of one 1800 lines/mm holographic reflective diffraction grating which, along with the CCD detector produces an intrinsic resolution of 0.04 nm (or 1.6 cm^{-1}) around 500 nm. The diffraction gratings can be moved using calibrated motors which provide a reproducibility of better than 0.05 nm on the complete scannable range. This is very important because our Raman spectra are taken around 500 nm, but the ruby luminescence must be measured around 700 nm. The system must be able to alternate between these two positions without requiring a recalibration.

A SPEX SpectraView 2D CCD (Charge-Coupled Device) detector is used to recover the light which is now spatially spread out in wavelength. To reduce the amount of thermally activated charges in the device and to increase the efficiency of the detector, it is kept cold, using liquid nitrogen, at 140K. The observed intensities for a given wavelength are produced

by summing the intensities on a vertical range and converting the position to a wavelength. The height of this vertical window can be adjusted with the program used to acquire the data. A complete image of the CCD can also be obtained to determine if it is positioned correctly (with no vertical tilt).

2.3.2.4 The Computerized Data Acquisition

As most spectrometry systems today, the acquisition process can be totally automated and controlled by computer using the J-Y Prism software. In this system, the premonochromator slit and the premonochromator and spectrometer positions can be set using a program provided to control the system. Additionally, the CCD image is collected and integrated to produce intensity vs. wavelength spectra. As a special use for Raman spectroscopy, the spectrometer position can be entered in wave numbers (in cm^{-1}) relative to a specified laser wavelength. The acquisition process then consists in specifying a range (e.g. 50 to 900 cm^{-1}) and an integration time. Since the intensities are stored internally as 16 bit integers, a saturation intensity of 65536 can be reached when some peaks are much stronger than others and the integration time is too long. Also, if the signal to noise ratio is very poor and if there is a large background, it is possible that the signal saturates without being satisfactorily identifiable. When using a DAC, this is sometimes a problem if the chosen diamonds didn't have a very low fluorescence, since the fluorescence, which increases when the diamond is stressed, form a very strong background.

With the level of automation provided by this system, once properly set up, a complete run in pressure is usually limited by the time it takes to get proper spectra and some pressure-related experimental problems which might arise.

3

STUDY OF ZrO_2 AND HfO_2

Both Zr and Hf have stable cations of the type M^{4+}, which have closed electronic shells and ionic radii of 0.84 and 0.87 Å respectively. Their oxides are both of the MO_2 type and have very similar chemical properties, in particular, they are both ceramics. In view of the identical charge and similar radii of the cations, it is reasonable that both compounds could also have similar pressure induced behaviour.

Since ZrO_2 is a very important compound in the ceramics industry, it has been more extensively studied than HfO_2. However, most of their high pressure phases have not been clearly identified until very recently, and not until this study for HfO_2.

At atmospheric pressure and room temperature, both compounds have a baddeleyite structure (space group $P2_1/c$) and transform to an orthorhombic structure (*Pbca*) around 5 GPa. Although a higher pressure phase has been observed for both compounds, its structure has been the source of many debates and has never been clearly and irrevocably identified. The most recent works propose a cotunnite-type phase (orthorhombic *Pnma*) for ZrO_2 and some tetragonal structure for HfO_2.

For this study, both energy and angle dispersive X-ray diffraction methods were used, with some Raman spectroscopic data to figure out the pressure dependence of both oxides' structures. The results are shown to be in agreement with other observations and establish unequivocally that both compounds have a cotunnite-type structure that is stable to 80 GPa, and quenchable to atmospheric pressure. The new high density phases are optically transparent and very hard, which might prove useful in technological applications.

The experimental procedure is briefly presented, followed by the results, analysis and discussion of each phase of the compounds and their pressure related properties. Both compounds are studied simultaneously, due to their identical behaviour under pressure.

3.1 Sample Preparation and Experimental Procedure

3.1.1 ZrO_2 and HfO_2 Samples

Both the ZrO_2 and HfO_2 samples are white powdered samples, with crystallite sizes less than 0.1 μm. The powders themselves consist of grains ranging from 0.1 μm to 2 μm. The ZrO_2 sample was purchased from Johnson-Matthey and is stated to have a 99.9+% purity, while the HfO_2 sample was purchased from STREM, with a purity of 99.998%.

3.1.2 DAC Preparation

Several samples were studied, using different diamond anvil cells and various pressure media. HfO_2 was the most studied, using the 500 and 300 μm cullet diamonds, in either a methanol/ethanol (4:1 ratio) or silicone oil pressure medium, or packed with no pressure medium. In every case, rubies ($Al_2O_3:Cr^{3+}$) were used for pressure calibrations. ZrO_2 was also studied in these three cases, but only in the 300 μm culet DAC. The most important difference between the two DACs is the maximum attainable pressure below the diamond anvils' breaking points, and it had no influence on the actual results. All other relevant information about the DACs has already been covered in the first chapter.

3.1.3 Energy Dispersive X-ray Diffraction

Energy dispersive X-ray diffraction was done at the Cornell High Energy Synchrotron Source (CHESS) B1 and D1 stations, for which the synchrotron source has a simple bending magnet, providing a critical energy of 10 keV (*ref.* Appendix B). The layout used is the same as explained in the section on the EDX method, and the detector angle was usually set at $2\theta = 14°$, giving Ed≈50 keV·Å. In the 20 keV to 50 keV range, we therefore can observe plane reflections with d-spacings 2.5 to 1.0 Å.

3.1.4 Raman Spectroscopy

Both these samples were observed using Raman spectroscopy with, usually, very poor results under pressure. However, the several good spectra obtained turned out to be very important to prove that both samples had the same high-density phase. The ambient pressure Raman spectrum of baddeleyite ZrO_2 and HfO_2 rapidly decayed with increased pressure, yielding no substantial signal above 5 GPa. The spectra of the quenched (outside of DAC) samples were also observed clearly (outside the DAC). The setup for Raman spectroscopy is the one provided in Dr. Desgreniers's laboratory, with an Ar^+ laser, using the 488 nm or 514 nm line. A 50× Olympus objective was used to focus the laser and recover the scattered radiation. Lines were observed in Stokes and anti-Stokes modes, between 150 and 800 cm^{-1}.

3.1.5 Angle Dispersive X-ray Diffraction

We have also had the chance to do angle dispersive X-ray diffraction at CHESS D1 using imaging plates on the quenched ZrO_2 sample. This experiment was clearly necessary to resolve with sufficient confidence what the quenched phase of ZrO_2 and HfO_2 could be. By EDX measurements, a simple structural fit (lattice parameters) could not isolate a single specific structure. A high quality ambient pressure spectrum of HfO_2 was also refined to test the experimental and refinement procedures and get very precise measurements on the lattice parameters of the baddeleyite phase (*ref.* Appendix D).

3.2 Combined Results and Analysis

Figure 3.5 and **Figure 3.6** represent the observed EDX spectra of HfO_2 and ZrO_2 at several pressures, as well as the spectrum of the quenched samples at atmospheric pressure. A complete display of the observed d-spacings, calculated from the observed peaks' energies and

the calibration is given in **Figures 3.1** to 3.4. The evolution of the d-spacings give information on any possible phase transitions, and they are used to calculate the lattice parameters of the structures. In addition, **Figure 3.7** and **Figure 3.8** show the atmospheric pressure Raman spectra of HfO_2 and ZrO_2, respectively, whereas **Figure 3.9** and **Figure 3.10** show the Raman spectra of the quenched phases. For each phase, relevant graphs and tables accompany and complement the text. Following the discussion on observed phase transitions, a paragraph details the properties of each of the observed phases.

3.2.1 Experimental Results

The EDX data clearly show the existence of three distinct phases under pressure, for both ZrO_2 and HfO_2. The first phase, labelled as Monoclinic I (or MI) has the baddeleyite-type structure usually associated with both compounds. The name *baddeleyite* actually refers to the monoclinic zirconia mineral. The d-spacing data clearly indicate the appearance of a new phase at 4 ± 0.5 GPa for both HfO_2 and ZrO_2, with the existence of a new peak between the $(11\bar{1})$ and (111) peaks of the MI phase (the two peaks with largest d-spacings in **Figure 3.1** and **Figure 3.3**). The coexistence of this second phase with the initial one occurs over a very large pressure range, as the $(11\bar{1})$ and (111) monoclinic peaks are still present up to around 25 GPa. Furthermore, the d-spacings of the second phase are very similar to those of the previous phase, suggesting that both structures are quite similar. This second phase is labelled as Orthorhombic II (or OII). Above 30 GPa in HfO_2 and 25 GPa in ZrO_2, yet another phase is present, for which the transition pressure range from OII phase is short. The disappearance of the OII phase is quite definite. The Orthorhombic III (or OIII) phase is stable to 73 GPa, the highest pressures reached, and is quenchable to ambient conditions in both HfO_2 and ZrO_2.

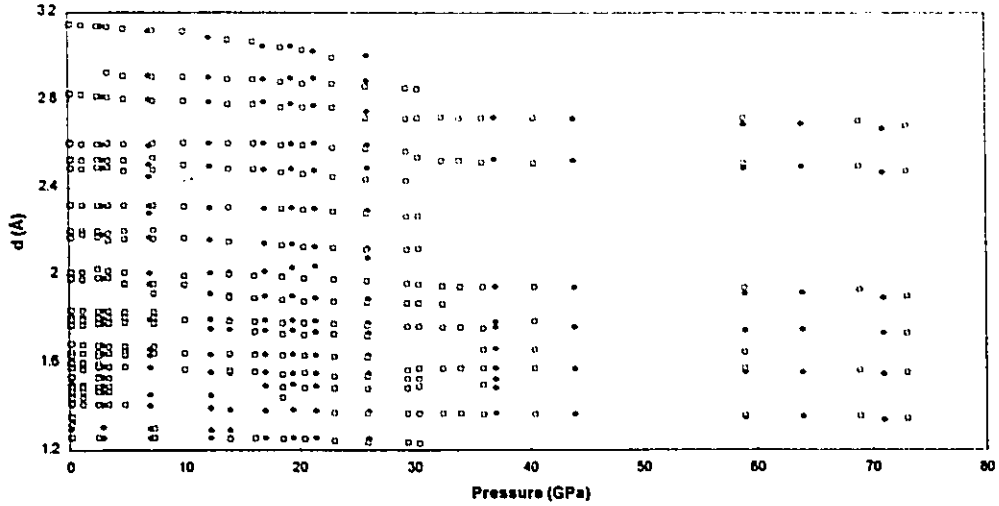

Figure 3.1 Evolution of the d-spacings in HfO_2 with increasing pressure, as measured by energy-dispersive X-ray diffraction. The square and diamond symbols correspond to different runs: □ with silicone oil as the pressure medium and ◆ without a pressure medium).

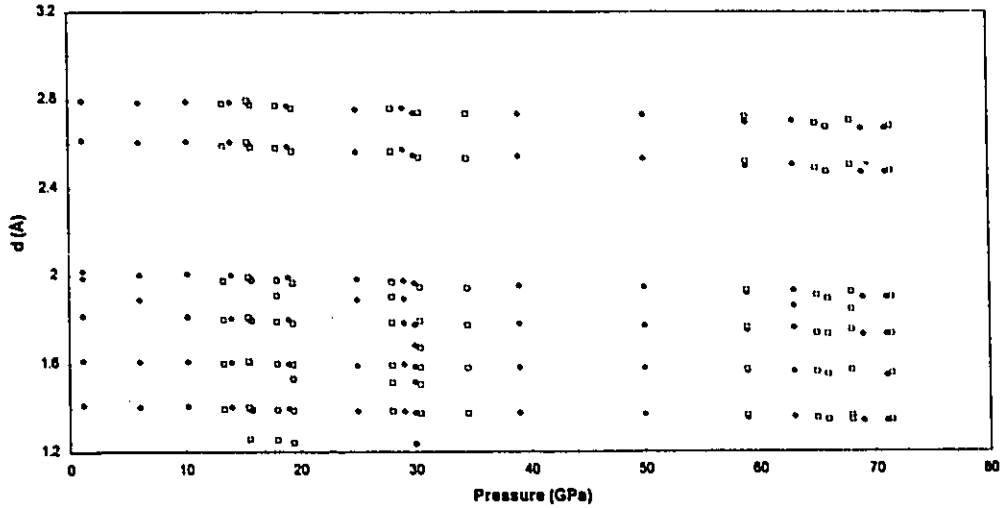

Figure 3.2 Evolution of the d-spacings in HfO_2 with decreasing pressure, measured by energy dispersive X-ray diffraction. The symbols correspond to the same runs as in **Figure 3.1** . The consistent interplanar distances clearly indicate that no phase transition has occurred and that the high-pressure phase has been quenched.

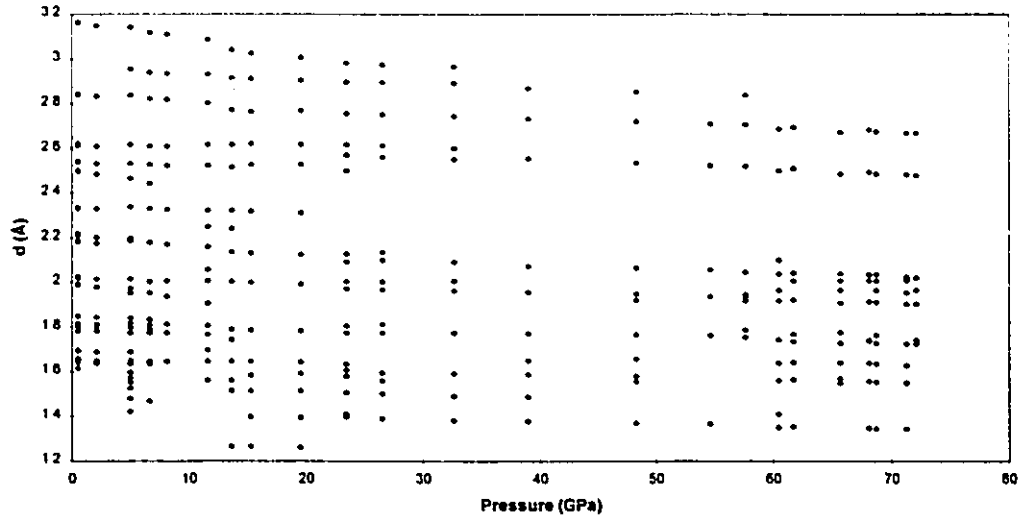

Figure 3.3 Evolution of the d-spacings in ZrO_2 with increasing pressure. The large number of peaks in the high pressure phase between 1.4 and 2.2 Å correspond to very weak peaks of the cotunnite structure. Because they are very weak, they are not consistently recorded. Also, the peak at 2.1 Å corresponds to a weak peak of the cotunnite structure which did not appear in the HfO_2 spectra. Some experimental errors due to the DAC placement can be noticed where all the d-spacings at a given pressure are shifted compared to an otherwise smooth evolution. These shifts are more visible at large d-spacings because the relative shift is constant.

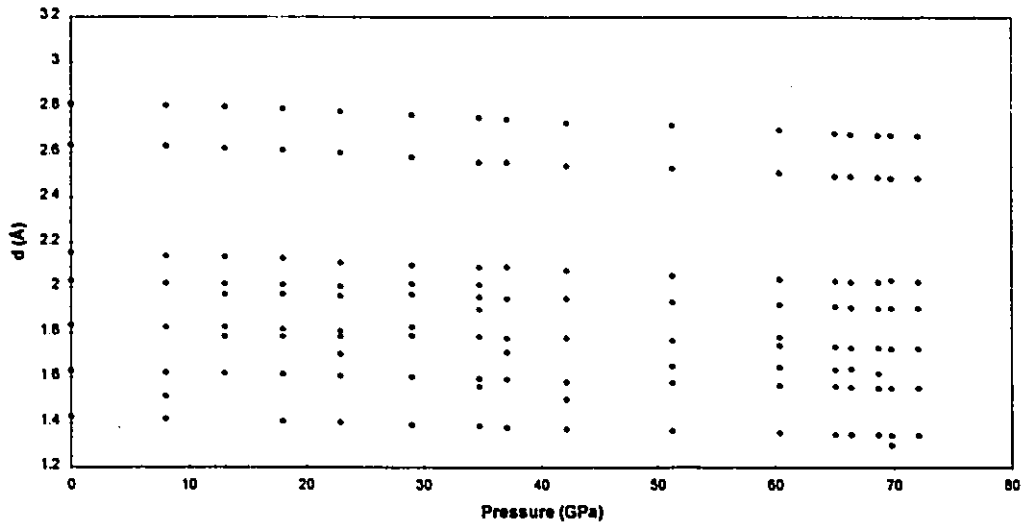

Figure 3.4 Evolution of the d-spacings in ZrO_2 with decreasing pressure, showing the quenching of the cotunnite phase.

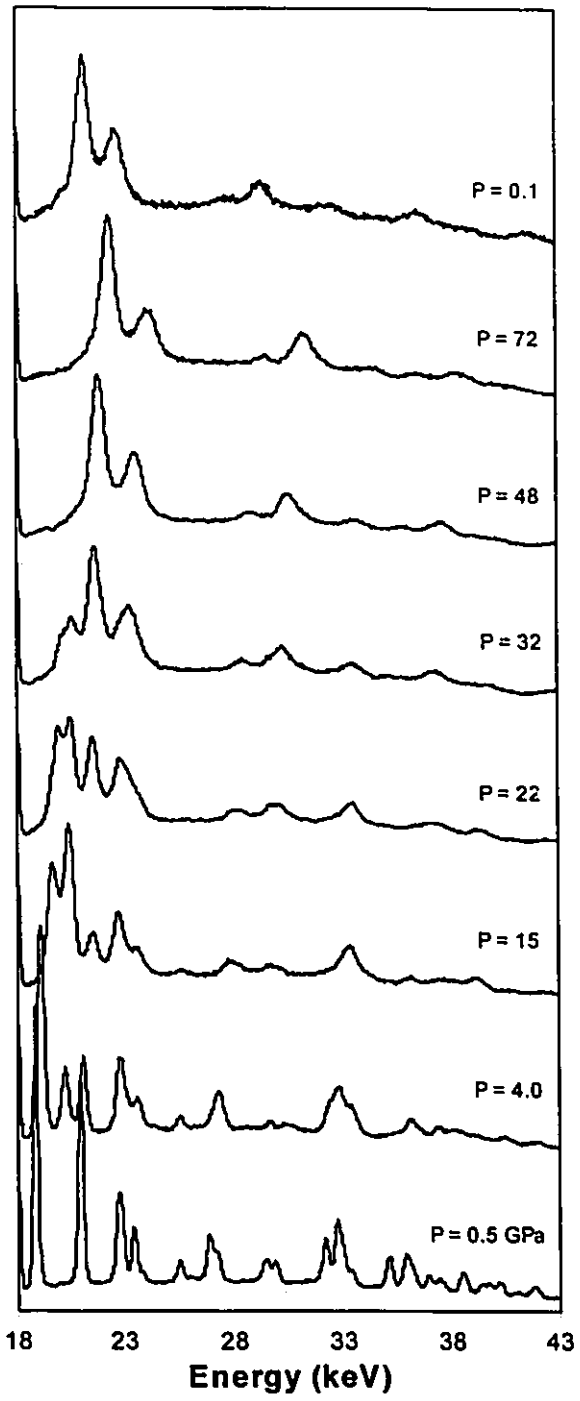

Figure 3.5 Selected EDX diffraction spectra of ZrO_2 at various pressures, illustrating the pressure behaviour of the three phases, and the quenching of the high pressure phase.

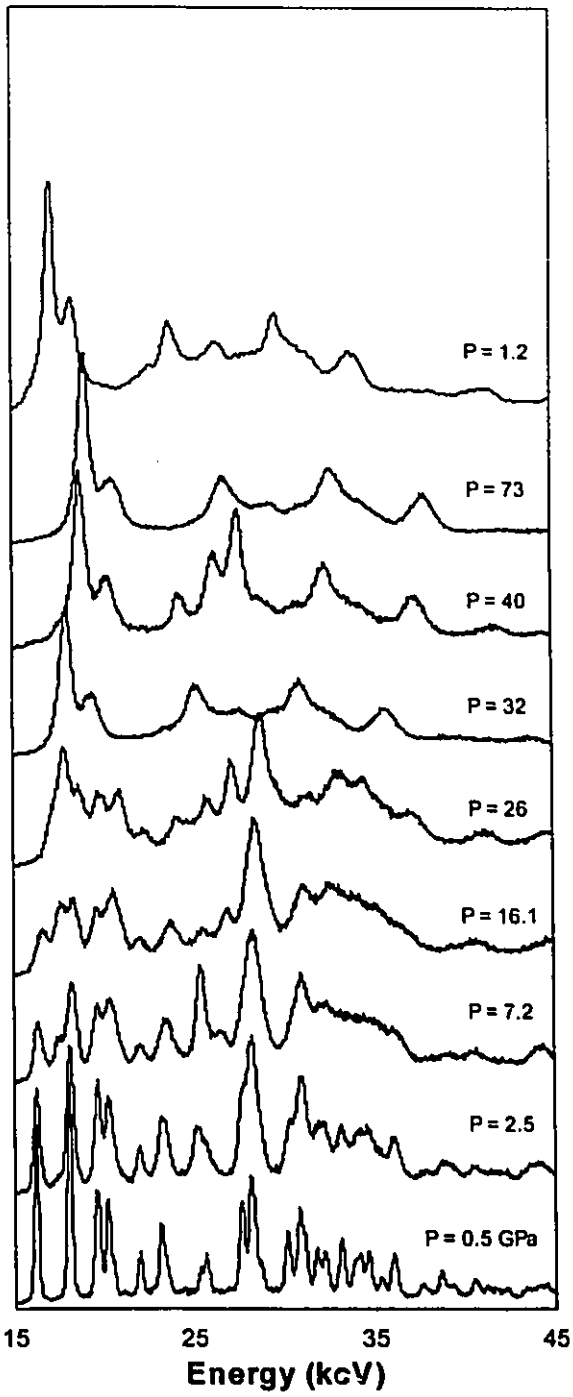

Figure 3.6 Selected EDX diffraction spectra of HfO_2 at various pressures. These spectra show the clear similarity between the high pressure phases of HfO_2 and ZrO_2.

3.2.2 The Baddeleyite, Monoclinic I Phase ($P2_1/c$)

The room temperature, ambient pressure phases of ZrO_2 and HfO_2 have been identified as monoclinic, with the $P2_1/c$ (Z=2) space group [Ruh, 1970], and described as a baddeleyite-type structure. Very often, the structure of a mineral rather than a space group is used to describe a phase, because it gives not only the space group of the unit cell but also the site symmetries of all the atoms in the crystal. For example, the baddeleyite structure corresponds to three distinct bases or atoms, each associated with four atoms according to a $P2_1/c$ arrangement. In our case, they are the cation (Zr or Hf) and the two oxygen atoms. Essentially, specifying the structure is more detailed than specifying only the space group. In this case, the baddeleyite mineral actually relates to monoclinic zirconia.

Though this phase has been well studied in the past, *in situ* pressure experiments have been scarce, and several attempts at the determination of its compressibility lead to substantially different results from one study to another [Adams 1991, Léger 1993a and 1993b, Jayaraman 1993, Nevitt 1988].

Our experiments show the coexistence of the baddeleyite phase with the second high pressure phase from pressures as low as 4 GPa in both compounds, but we were nevertheless able to obtain refined lattice parameters for the monoclinic phase up to 8 GPa in ZrO_2 and 10 GPa in HfO_2 (**Figure 3.13** and **Figure 3.14**). Additionally, as reported in other studies, the $(11\bar{1})$ and (111) peaks were visible to 25 GPa. As shown in **Table 3.2** and **Table 3.3** , this leads to a value of the room conditions bulk modulus of $B_0 = 284\pm30$ GPa ($B_0'=4.6\pm2.0$) for HfO_2 and $B_0 = 212\pm25$ GPa ($B_0'=8.0\pm4.0$) for ZrO_2. These values do not depend much on B_0' because the range and number of points used for the fit is very limited. However these bulk moduli are much larger than those observed in the stated references, which give values of 95 ± 8 GPa ($B_0'=4$) [Léger 1993a], 135 GPa [Smith 1965] and 185 GPa [Nevitt 1988, Cohen 1988] for ZrO_2 and 145 [Léger 1993b] to 185 GPa (estimated) [Jayaraman 1993] for HfO_2 respectively. Adams *et al.* [1991] have reported a linear compressibility of $1.2\cdot10^{-3}$ GPa^{-1}, which

gives an unrealistic bulk modulus of 833 GPa (for comparison, B_0=450 for diamond). From their graph, we have calculated a bulk modulus of 400 GPa, which is still very large. According to the bulk modulus-volume relation [Anderson, 1972], B_0(GPa) = 700 S^2 $Z_A Z_C / V_0$, where S^2=0.5 for oxides, Z_A and Z_C are the formal charges of the anion (2 for O^{2-}) and the cation (4 for Hf^{4+} and Zr^{4+}), and V_0 is the mean molar volume of an atomic pair. For monoclinic HfO_2, this would give a value of 200 GPa, and 195 GPa for ZrO_2, which indicates that the results we have obtained are sufficiently accurate.

Because the following phase is structurally similar to the baddeleyite phase, most peaks appear very close to those of the initial phase, so an accurate determination of the volume of these compounds would require very good data, specifically generated to determine the properties of the phases during the transition. Because we were more interested in the higher pressure phases, few pressure points were generated, and only the EDX method was used, resulting in less than optimal conditions to study this transition. A high resolution single crystal X-ray diffraction experiment would be much better, as would be other methods to determine the bulk modulus and its derivative from atmospheric pressure experiments, such as ultrasonic measurements.

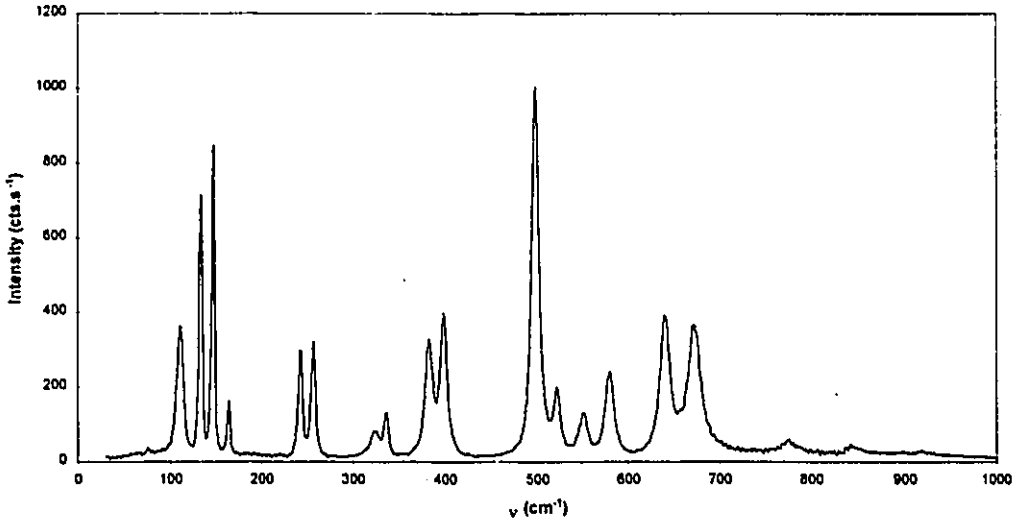

Figure 3.7 Raman spectrum of the baddeleyite phase of HfO_2 at ambient pressure and temperature. The spectrum was taken outside of the DAC, using a 50× microscope objective.

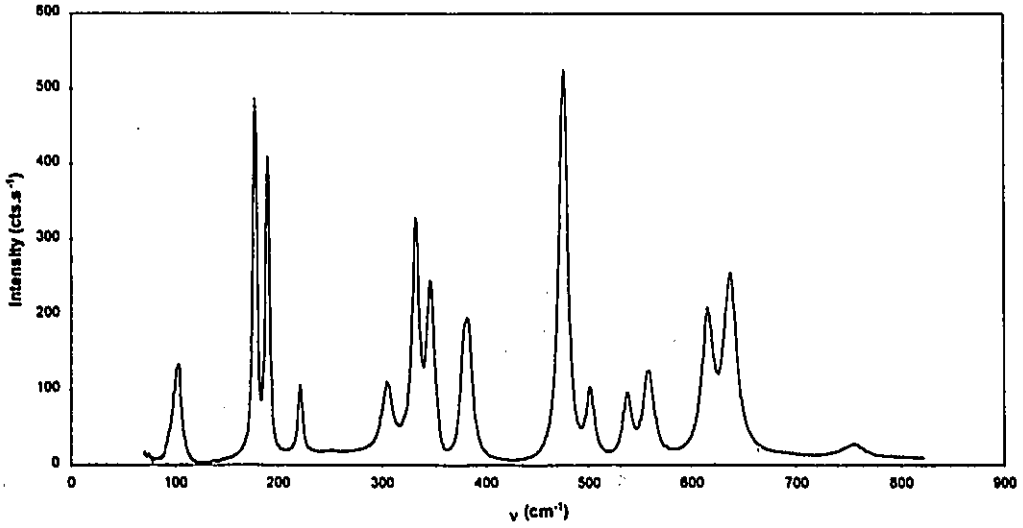

Figure 3.8 Raman spectrum of the baddeleyite phase of ZrO_2, taken in the same conditions as that of HfO_2. Notice the similar features in both spectra, which differ mainly in the position of the peaks.

3.2.3 The Orthorhombic II Phase (*Pbca*)

From pressures as small as 4 GPa, a new line appears in both samples' diffraction patterns, corresponding to the (211) reflection of the new phase. Even though this second phase had been observed long ago from quenched experiments [Bendeliani 1967, Kulcinski 1968], the actual structure has not been solved until recently [Ohtaka 1990, Ohtaka 1991] . An orthorhombic cell with space group *Pbca* (Z=8) was determined to be the best solution compatible with the neutron and the X-ray diffraction data, for both compounds. Previously, in several studies of ZrO_2 and HfO_2, the authors had thought it to be either tetragonal [Liu 1980] or orthorhombic with space group *Pbcm* for ZrO_2 [Kudoh 1986], but recent high resolution neutron diffraction experiments [Ohtaka 1990, Howard 1991] have shown it to be *Pbca*. Similar X-ray diffraction results have shown that the OII phase of HfO_2 belongs to the *Pbca* space group [Ohtaka 1991, Suyama 1987]. The structure is derived from an alternate stacking of cells with $Pbc2_1$ symmetry. Kudoh *et al.* [1986] studied this phase using single crystal X-ray diffraction, and assumed a centro-symmetric *Pbcm* type cell based on the observed extinction rules and the fact that previous Raman data [Arashi 1982] had shown that the space group should have a centre of inversion. The other space group considered was $Pbc2_1$; however this space group is non-centrosymmetric. High resolution neutron diffraction on quenched samples [Ohtaka 1990] showed that the structure actually consisted of the stacking of two cells with $Pbc2_1$ (non-centrosymmetric) symmetry yielding a centrosymmetric *Pbca* space group. This comes from the fact that two types of the O1 atoms exist in each of the two $Pbc2_1$ cells (in an obverse and reverse geometry), producing a doubling of the real unit cell. The centrosymmetry is consistent with the Raman data, and the extinction rules which come from the $Pbc2_1$ symmetry are those observed by X-ray diffraction, where the averaging of the two types of O1 atoms produce a *Pbcm*-like space group.

The transition from the $P2_1/c$ to the *Pbca* phase is displacive and corresponds to an order-disorder transition in the oxygen atoms. The cations do not move much, but the O1

atoms' net is substantially reorganized, producing the higher *Pbca* symmetry. This new phase is intermediate between the monoclinic ($P2_1/c$) and high-temperature tetragonal ($P4_2/nmc$) phase of both ZrO_2 and HfO_2. Because this transition is mainly due to the reorganization of the oxygen atoms, the diffraction pattern is very similar to that of the monoclinic phase, except that there is a doubling of the *h* Miller index (because of the doubling of the a lattice parameter), and lines with positive and negative *l* index occur at an intermediate d-spacing, as seen for the $(11\bar{1})$ and (111) monoclinic lines resulting in the (211) orthorhombic line. Kudoh *et al.* [1986] determined from a single crystal study that the [010] and [001] directions of the MI and OII phases are identical throughout the transition. Because of the close similarity of the structures, the coexistence of the two phases is possible in powdered samples, which explains why the MI $(11\bar{1})$ is still observed up to 25 GPa even though the OII (211) line is visible from 4 GPa. Arashi *et al.* [1982] showed that a single crystal of baddeleyite ZrO_2 could transform without twinning to a single crystal of OII ZrO_2. The transition is accompanied by a slight 2.9% reduction in the molar volume. It should also be noted that for the MI to OII transition there is no change in the coordination number for the cations. It remains at seven, even though previously proposed tetragonal cells suggested it might be eight. In general, higher pressure phases have higher coordination numbers, corresponding to a better atomic packing.

3.2.4 The Cotunnite, Orthorhombic III Phase (*Pnma*)

Another transition takes place above 25 GPa for ZrO_2 and 30 GPa in HfO_2, giving rise to a new orthorhombic structure. In 1980, Liu [1980] recorded X-ray diffraction spectra of both compounds that had been quenched from 1000°C and pressures ranging from 8 to 30 GPa, and discovered a new quenched phase that he associated with a cotunnite-type ($PbCl_2$) structure. Since then, there has been much discussion regarding the determination of the high-pressure behaviour of the two compounds. Ming *et al.* [1985] repeated the experience *in situ* at 1000°C, confirming the existence and stability of the cotunnite phase between 15 and 30 GPa,

as well as its quenching when receding back to room conditions.

3.2.4.1 The Controversy in Recent Literature

Since these experiments, several were performed on each of the two compounds, using X-ray diffraction and Raman spectroscopy. Among these experiments, Arashi *et al.* [1990] studied ZrO_2 *in situ* by ADX diffraction and Raman spectroscopy but could not confirm that the third phase observed between 15 and 32 GPa has a cotunnite-type structure. They reported a fourth phase at pressures above 32 GPa and quenchable to room conditions. Based on the Raman spectrum and only four diffraction peaks, Arashi and coworkers proposed a tetragonal symmetry for this phase. Jayaraman *et al.* [1988] subsequently studied HfO_2 by Raman spectroscopy up to 50 GPa, starting with a single crystal. Based on the results of Arashi *et al.*, in their study of ZrO_2, they identified the OII phase from 4 GPa and above. Also, at 29 GPa, a transition to a phase assumed to have the tetragonal symmetry proposed by Arashi *et al.* was observed. This high-pressure phase persisted to the maximum pressure attainable and is quenchable to room conditions. Its spectrum strongly resembled that obtained by Arashi *et al.* on the quenched sample of ZrO_2. Between these two transitions, they also observed a transition around 12 GPa. By inspection of the Raman shifts, it is very hard to ascertain that a transition does actually take place, because there is no really clear break in any of the Raman shifts' evolutions with pressure. It should be pointed out that 12 GPa is very close to the freezing point of the 4:1 methanol-ethanol mixture used as the pressure medium, which would create a small shift in the lines because of the slight anisotropy of the pressure field induced by the solid phase of the pressure medium. Based on our own results, which appear conclusive in showing the quenching of the cotunnite phase for both samples according to *in situ* X-ray diffraction, and the Raman spectra of the quenched phases being nearly identical to those obtained by Arashi *et al.* and Jayaraman *et al.*, we believe they have mistakenly observed an inexistent transition, and that they actually quenched the cotunnite, OIII, phase. Two other

studies performed on ZrO_2 and HfO_2 by Léger and coworkers observe a new orthorhombic phase in ZrO_2 [Léger 1993a] above 40 GPa, which, according to the d-spacings is very similar to the third phase which occurred between 28 and 40 GPa, and a new tetragonal phase in HfO_2 [Léger 1993b] above 42 GPa, which coexists with the third phase for which the transition pressure is between 23 and 28 GPa. None of these new high pressure phases are quenchable to room conditions. This shows how much controversy there is about the high pressure phase diagram of both compounds, and why a clear, unequivocal solution is needed. It should be noted that none of the X-ray studies done so far used digitized data, so only d-spacings could be observed on films and be used to determine structures, transitions, or any other phenomenon.

3.2.4.2 An Attempt to Find an Acceptable Solution

Recently, Haines *et al.* [1995], published a thorough X-ray diffraction study of ZrO_2 up to 50 GPa, on laser-heated and unheated samples where patterns were recorded using standard film and imaging plates (ambient spectrum) which were digitized and analysed by the Rietveld refinement method. The same three phases as we observe ($P2_1/c$ - MI, *Pbca* - OII and *Pnma* - OIII) were identified, with the cotunnite phase appearing above 25 GPa. The heating of the sample increased the amount of the cotunnite phase, which was quenchable to room conditions. They were not, however, able to obtain a quenched sample with a pure cotunnite-type structure: there was some residual OII phase in the sample which was taken to 50 GPa. They did observe, however, that the complete portion of the sample that had changed to the OIII phase was quenched in that phase, whereas the OII portion receded back to the MI phase. This group had previously published another study on ZrO_2 [Léger 1993a] and data published in 1993 were reanalysed. They digitized the data on the films from which ring positions had previously been extracted. Instead of observing a new transition after the OIII cotunnite phase, they ascertained the stability of the cotunnite phase between 25 and 50 GPa, in

agreement with our results, as we demonstrate in the following paragraph.

3.2.4.3 Our Evidence for a Cotunnite-Type Phase

The X-ray diffraction spectra indicate the quenching from high pressure of a similar high pressure phase for both compounds (**Figure 3.6** and **Figure 3.5**). The Raman spectra of the quenched phase (**Figure 3.9** and **Figure 3.10**) also display the same characteristics (one peak at low ν, a group of two then a group of three), proving that the high pressure phase is quenched, and that it is identical for both compounds. This result in itself is very important because it is the first time both Raman data and X-ray diffraction data for both compounds clearly indicate this similar behaviour. It is still necessary to identify this common phase, which we have successfully linked to a cotunnite-type structure with the help of full pattern profile fitting (Rietveld analysis) on ADX data.

As seen in the X-ray diffraction spectra of the OIII phase, diffraction peaks are really broad, suggesting some form of residual stress inside the sample, either between grains or by dislocations or point defects in the crystallites. Intrinsic line broadening has hence limited the resolution of any experiment, irrespective of the instruments and experimental technique used. A definitive identification of the phase was not initially possible based solely on a d-spacing analysis. We tried annealing several quenched samples by heating them to reduce the imperfections in the crystallites. This was done in a conventional oven in a 1/3 atm N_2 atmosphere, at 600°C for 6 to 24 hours. Unfortunately, the samples always transformed back to the monoclinic phase, as indicated by Raman spectroscopy, which showed the limited temperature stability of the quenched OIII phase.

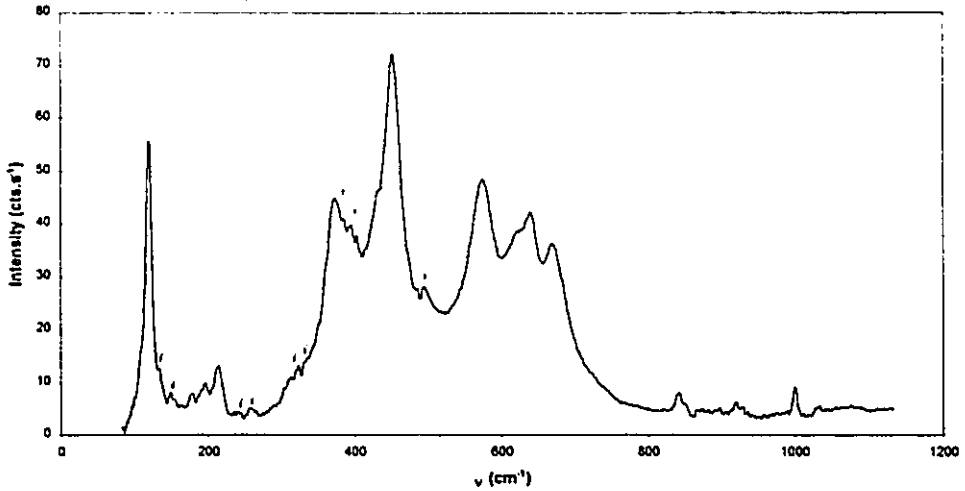

Figure 3.9 Raman spectrum of the quenched cotunnite phase in HfO_2, mixed with a small proportion of the baddeleyite phase (**Figure 3.7** with visible peaks indicated by arrows). The spectrum was also obtained outside of the DAC with the 50× objective. No *in situ* measurements were possible because the signal decayed before reaching sufficient pressures to obtain this phase. For reference, this was from a sample taken to 50 GPa, which shows that higher pressures are needed to obtain a pure cotunnite-type phase.

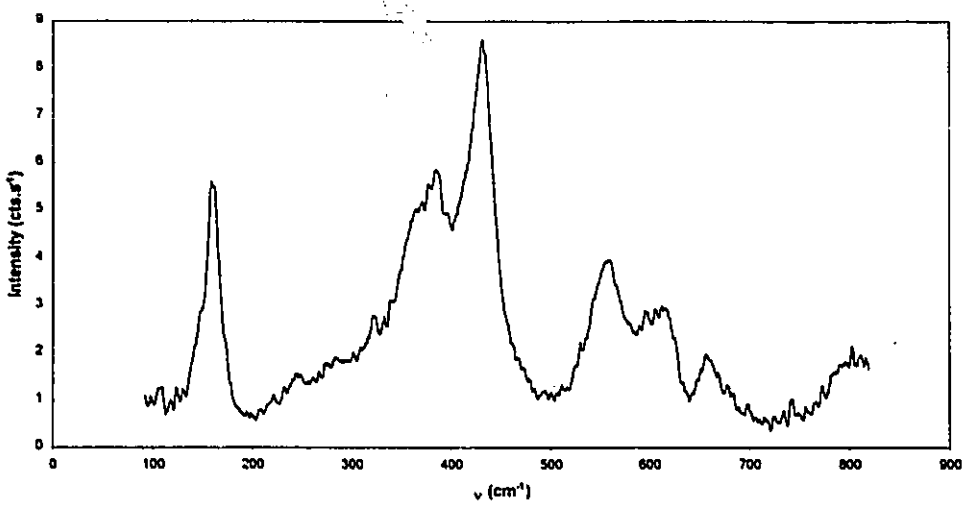

Figure 3.10 Raman spectrum of the quenched cotunnite phase of ZrO_2, taken in the same conditions as that of HfO_2. Even though the signal is much worse than for HfO_2, we can notice the very similar features between the two spectra, which, along with the X-ray spectra, proves that ZrO_2 and HfO_2 have the same high-pressure phase, identified as a cotunnite-type structure.

IPA, a program written by myself and described in Appendix D, was used to analyse the imaging plate data and integrate it into intensity vs. 2θ data, refinable with the Rietveld method. The program used for Rietveld analysis is DBWS 9411 [Young, 1994]. A space group must be assumed for the refinement process, as well as initial parameters. The initial atomic positions used were those of Haines *et al.*, as were the lattice parameters. The other parameters, such as preferred orientation, were initially omitted, then incorporated to get a better fit. There is a slight difference between our results and those obtained by Haines *et al.*, but both represent very good fits to relatively low resolution data, because the peaks are very broad and that the low d-spacing data are quite insignificant. Results obtained from this study do however explain the complete spectrum using only one ZrO_2 phase (apart from the HCP and BCC phases from the AISI T301 gasket (Fe/Cr/Ni)), rather than the three phases (plus one Ni-gasket phase) as assumed by Haines *et al.*, clearly showing the phase purity of our quenched sample. Haines *et al.* required the presence of the MI and OII phases to explain all the peaks that were observed, resulting in greater latitude during the refinement process. In our case, there was no evidence that any of the MI or OII phases were present, since the cotunnite-type structure of the OIII phase was clearly sufficient to explain the data. A preferred orientation was included, as it was done by Haines *et al.*, based on the irregular observed relative intensities of (*h0l*) peaks. This is a common effect when one lattice parameter, in this case b, is much smaller than the others, usually such structures generate platey crystallites which orient preferably.

The strong peaks' d-spacings have been identified and used to analyse the EDX data using XRDA [Desgreniers 1994 and Appendix C]. These data, recorded as a function of pressure, were analysed to determine the lattice parameters of the unit cell at high pressure, and consequently the equation of state parameters. **Table 3.1** and **Figure 3.11** represent the results of the Rietveld refinement and **Figure 3.12** proposes a view of the corresponding structure, as projected along the b axis, and showing the clear coordination of the Zr atoms with nine surrounding O atoms. Considering that the oxygen atoms contribute very little to

Table 3.1 Results of the Rietveld refinement performed on the diffraction pattern of a quenched sample of ZrO_2.The refinement includes the BCC and HCP phases from the gasket, with massic proportions of 0.07% and 0.67%, respectively.

Space group		*Pnma* (n° 62), Z=4 Cotunnite-type structure	
cell parameters			
	a	5.620 ± 0.004	Å
	b	3.347 ± 0.002	Å
	c	6.503 ± 0.004	Å
	V	122.32 ± 0.14	$Å^3$
atomic positions			
Zr	x	0.2622 ± 0.0009	
	y	0.2500 (fixed)	
	z	0.1094 ± 0.0005	
O1	x	0.4589 ± 0.0035	
	y	0.2500 (fixed)	
	z	0.4523 ± 0.0034	
O2	x	0.1065 ± 0.0058	
	y	0.7500 (fixed)	
	z	0.3243 ± 0.0029	
preferred orientation		March-Dollase function	
	PO vector	(0, 1, 0)	
	r	1.408	
refinement statistics			
	R_{wp}	1.37	
	R_p	1.11	
	$d_{Durbin-Watson}$	0.25	this small value indicates that the calculated uncertainties are underestimated
	R_{BRAGG}	2.30	

the spectrum ($\Sigma|F_O|^2 \approx 7\% \Sigma|F|^2$), resulting in a larger uncertainty of their parameters, this closely resembles the structure proposed by Haines *et al.* [1995].

The ADX data thus helped us solve the structure, and using the EDX data we could generate an equation of state for the quenched phase.

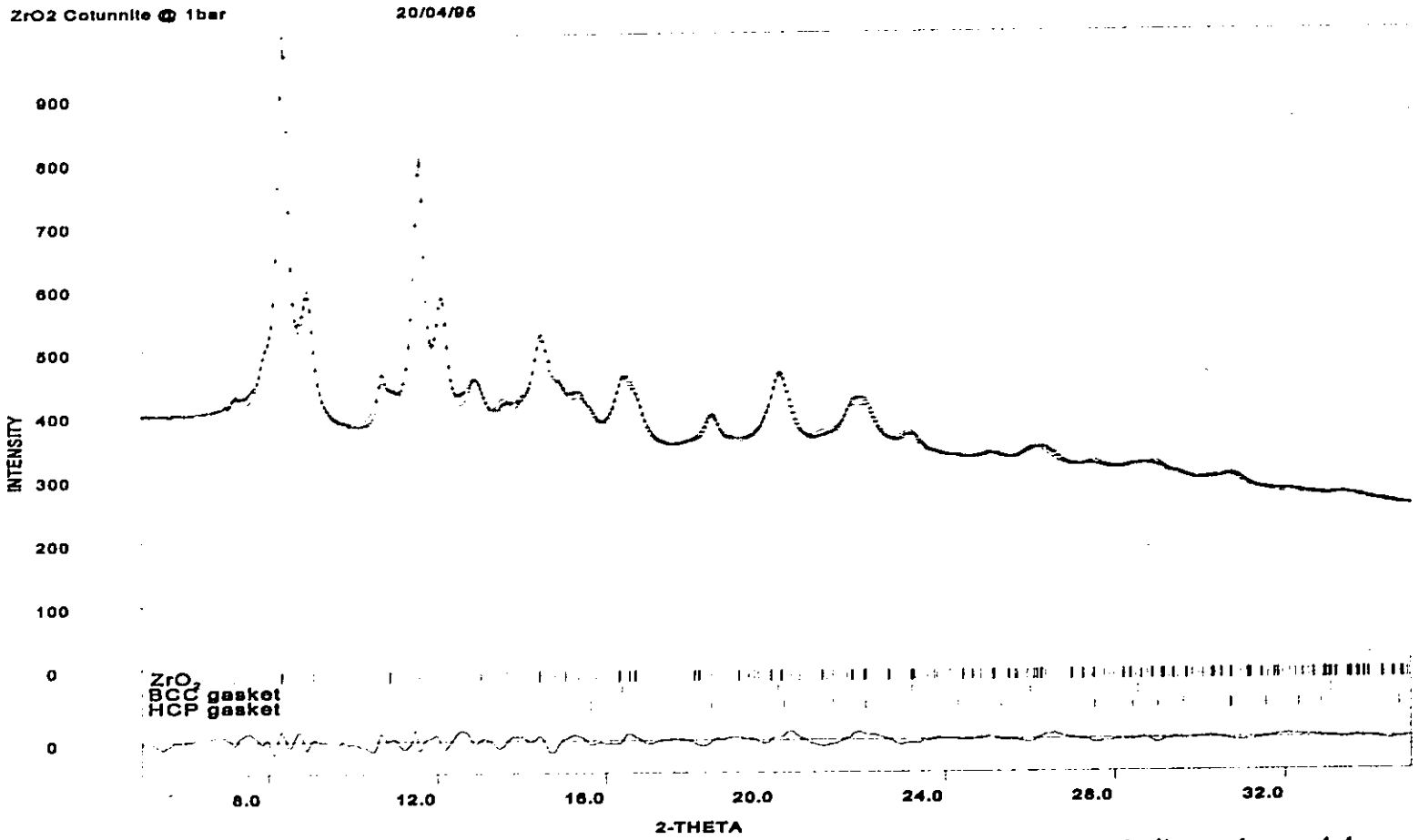

Figure 3.11 Result of the Rietveld analysis performed on a quenched sample of ZrO_2. Crosses indicate observed data, and the continuous curve the calculated spectrum, according to the data from Table 3.1 . The fit also contains the HCP and BCC phases of stainless steel gasket. The Bragg R-value is 2.3.

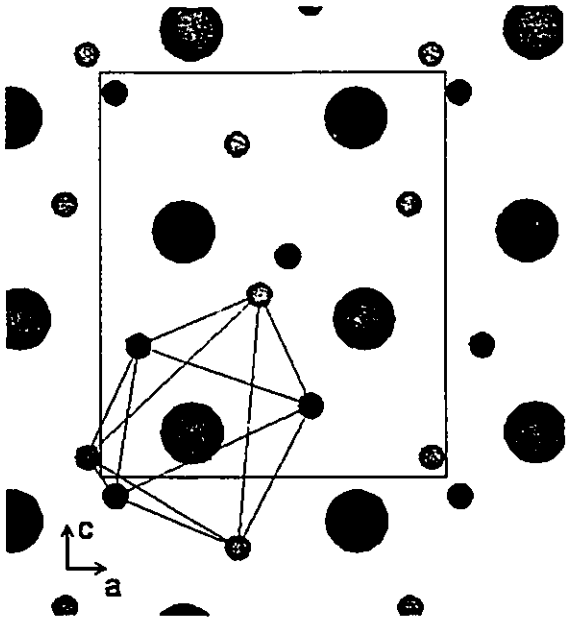

Figure 3.12 Projection of the quenched cotunnite-type structure of ZrO_2 along the y axis. Large circles represent Zr atoms, whereas small ones represent O atoms. The light colour atoms are those located at in the y = 0.25 plane and the darker ones are in the y = 0.75 plane. The figure also shows the nine-fold coordination of a Zr atom, with three oxygen atoms in the same plane (y= 0.25), and three on each nearest plane (y = 0.75 and y = -0.25).

3.2.5 Equations of State

In these regards, we have obtained very important results. The Pressure-Volume relation for both compounds is very peculiar in that the pressure derivative of the bulk modulus, B_0', is very low compared to the normal value of 4 or 5 in other materials. This is readily observable by the nearly linear V vs. P curves for the OIII phase (**Figure 3.14** and **Figure 3.13**). This also results in large bulk moduli, since smaller B_0' usually produce larger B_0 when the fit is performed with fixed B_0' on the same set of data. **Table 3.2** and **Table 3.3** give the fitted parameters for the Birch-Murnaghan equations of state. All three parameters were refined simultaneously, except in the case of cotunnite-ZrO_2 (OIII) where B_0' was fixed to 1.0; this value for B_0' was chosen for this phase because, in the observed pressure range, this

correponds to a linear relation between V and P, which is what it seems to be, according to **Figure 3.13** . The actual refinement lead to a value of 0.3, which produced a nearly identical result as with a fixed value of 1.0, but this is physically absurd because the compressibility increased slightly at higher pressures. It should be noted that the uncertainties on the volumes and the pressure are large, giving a substantial lattitude on the refined parameters, these uncertainties were not used as weights in the fitting process. Although such small values for B_0' have been obtained in other reports, no explanation was ever given. It has been shown by Hofmeister [1993] that the Birch-Murnaghan EOS is known to be applicable for solids with $3.9 \leq B_0' \leq 6$. This seems to be a perfect example where the assumption of finite strain is quite inadequate. An extreme case like that of ZrO_2 has forced us to look for an explanation of the phenomenon. Also, the bulk moduli of both compounds are greatly affected by the values,

Table 3.2 Birch-Murnaghan Equation of State Parameters for HfO_2

	[this work]			*[Léger 1993b]*			
	Mono I	***Ortho II***	***Ortho III***	***Mono I***	***Ortho II***	***Ortho III***	***Tetra IV***
B_0 (GPa)	284 ± 30	281 ± 10	340 ± 10	145	210	475	550
B_0'	4.6 ± 2.0	4.2 ± 1.0	2.6 ± 0.3	5	5	5	5
V/V_{MI} @ 0 GPa	1.000	0.955	0.876	1.000	0.955	0.881	0.815

Table 3.3 Birch-Murnaghan Equation of State Parameters for ZrO_2

	[this work]			*[Léger 1993a]*		*[Haines 1995]*
	Mono I	***Ortho II***	***Ortho III***	***Mono I***	***Ortho II***	***Ortho III***
B_0 (GPa)	212 ± 25	243 ± 10	444 ± 15	95 ± 8	220	332 ± 8
B_0'	8.0 ± 4.0	6.7 ± 1.7	1.0 (fixed)	4 - 5	5	2.3 ± 0.4
V/V_{MI} @ 0 GPa	1.000	0.966	0.870	1.000	0.952	0.862

and the extremely low compressibility of the samples must be linked to this curious EOS. A simple increase in the density of the sample is not sufficient to explain such a large compressibility, and an increase in a covalent-type bond would increase the bulk modulus, but this does not account for the low B_0' value. Upon observation of the quenched sample with a simple microscope, the grain size was found to be extremely small (smaller than the resolution of the microscope). The presence of residual stress between grains or within crystallites, as assumed because of the extreme width of the peaks in the ADX measurements, would obviously invalidate the finite strain assumption of the Birch-Murnaghan EOS. Instead, these interactions could store a sufficient amount of energy to make the sample be so stiff under compression.

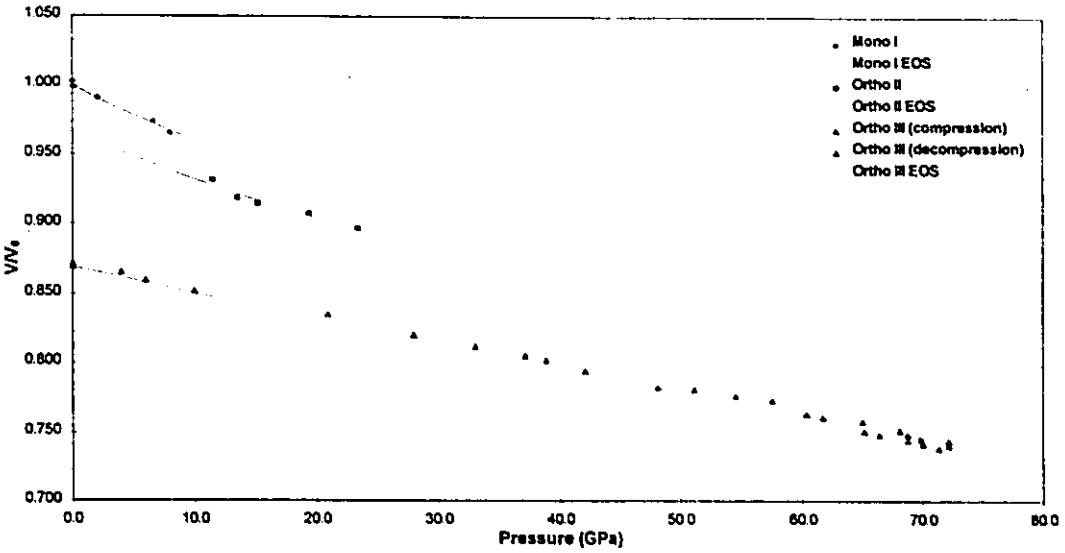

Figure 3.13 Pressure dependence of the volume of the high pressure phases of ZrO_2, along with the fitted Birch-Murnaghan equations of state with the parameters given in **Table 3.3** .

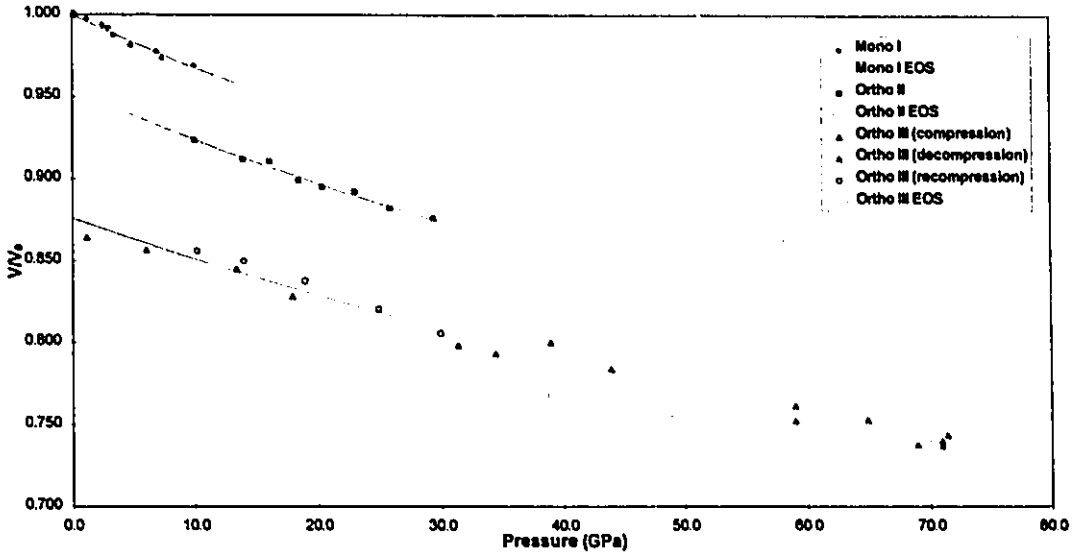

Figure 3.14 Pressure dependence of the volume of the high pressure phases of HfO_2, along with the fitted Birch-Murnaghan equations of state with the parameters given in **Table 3.2** .

3.3 Conclusion

The study we performed to identify the high pressure phases of HfO_2 and ZrO_2 was successful in identifying the dense phase as a cotunnite-type structure and establishing its stability between 25 GPa for ZrO_2 and 28 GPa for HfO_2, to pressures exceeding 70 GPa. Additionally, this phase is quenchable, when submitted to pressures of 70 GPa at room temperature, to room conditions and presents an extremely low compressibility and high density. In both compounds, we were able to obtain pure cotunnite-type phases in the quenched materials, which had not yet been performed so far. It seems that generating pressures greater than 50 GPa, the largest tested on these compounds was the determining factor in obtaining truely pure phases. Additionally, according to Haines *et al.* [1995], the heating of the materials at high pressures should also prove useful to purify the phase.

The evidence of a cotunnite-type structure is very important in the global scheme of transition metal dioxides, since this structure is proposed for many high pressure phases of other compounds, but was never clearly identified, except really recently for ZrO_2. The complete experimentation required to ascertain the properties of the high pressure phase also indicates how important it is to use different experimental methods to validate findings. Even though the Raman spectroscopy data could be considered to have failed, it was crucial for us to verify that we had obtained a quenched sample when we did not have access to a synchrotron, and also to compare it to other studies, to show we are discussing the same phase. The EDX data is much simpler to acquire, but the ADX data was crucial to actually perform a full pattern adjustment, rather than a simple d-spacing analysis.

Finally, our findings may lead to important contributions to the future search of stable, potentially harder-than-diamond materials.

4

STUDY OF ANATASE AND RUTILE TiO_2

Titanium (Ti) is also a transition metal element of the group IVB which produces a closed shell Ti^{4+} cation. Its most common oxide is TiO_2 which is found naturally in four different structures. Rutile is the most common and, according to recent calculations, is the most stable at atmospheric pressure and room temperature [Fahmi, 1993]. The other polymorphs are anatase, brookite and a columbite-type (α-PbO_2) structure [Dachille 1968, Linde 1969].

The radius of the Ti^{4+} ion is 0.64 Å, which is substantially smaller than that of the Zr^{4+} and Hf^{4+} ions. Among dioxides of transition metals elements, it is considered to be part of the group with the smaller cations, which usually share common phase diagram characteristics, most notably they usually have a stable rutile-type phase, and a high density fluorite-type phase.

Both anatase and rutile have been studied here, to give more evidence for a high pressure baddeleyite-type phase [Sato, 1991] and to attest to the discovery of a new phase transition at pressures around 80 GPa [Endo, 1993]. For this purpose, both Raman spectroscopy and X-ray diffraction were used to determine the high-pressure structures' characteristics.

TiO_2 is known to transform to an α-PbO_2-type structure at around 4 GPa, depending on the initial structure and its degree of crystallinity [Bendeliani, 1966]. When starting with rutile, this transition does not occur, and rutile is observed to 20 GPa. A second phase transition occurs at 13 GPa to a structure identified as baddeleyite. This transition is very slow, and temperature annealing of the sample is said to be necessary to obtain a pure baddeleyite-type phase at 20 GPa [Sato, 1991]. The data from our study of ZrO_2 and HfO_2 is valuable here to corroborate this identification, as both compounds have a baddeleyite-type structure at room conditions.

A Raman study on a single crystal of anatase up to 70 GPa is presented, followed by energy-dispersive X-ray diffraction data starting with both anatase and rutile samples to establish their respective equations of state.

4.1 Raman Study of Single Crystal Anatase[†]

4.1.1 Introduction

The pressure induced behaviour of a single crystal of anatase was studied by Raman spectroscopy, up to a pressure of 70 GPa. This study is the first to be performed on a single crystal, since only recently have high purity single crystals of anatase been available [Berger, 1993]. This is important, especially with respect to the pressure of the first transition to the columbite-type phase. Very few studies have been performed on anatase [Gou 1989, Haines 1993], from which this transition has been observed as being sluggish and to start at around 6 or 7 GPa. The next transformation to the baddeleyite-type phase occurs around 15 GPa, and is stable to at least 80 GPa. A new modification of TiO_2 above 80 GPa has been reported by Endo *et al.* [1993] on the basis of a new reflection in an X-ray diffraction study, and some change in the Raman spectrum. This result had not since been confirmed. To complement the Raman study, a few EDX diffraction spectra of TiO_2 up to 105 GPa were obtained to try to ascertain this result.

4.1.2 Sample and DAC Preparation

Single crystals used in this study were grown by chemical vapour transport reactions, as detailed by Berger *et al.* [1993]. These crystals have a very high phase purity, as confirmed

---

[†]The results discussed in this section have been reported in K. Lagarec and S. Desgreniers, "Raman Study of Single Crystal Anatase TiO_2 up to 70 GPa", *Solid State Commun.*, 94, 519 (1995).

by the Raman spectroscopy data, whereas commercially available anatase crystals are often contaminated by other polymorphs of TiO_2, especially rutile. Because of the high purity, any effects due to these phase impurities can be avoided.

A crystallite of approximately 50 μm in diameter by 30 μm width was placed in a 150 μm hole drilled in a pre-indented AISI T301 gasket. The DAC with 300 μm culets was used to generate the pressure, and a 4:1 methanol-ethanol solution was used as a pressure medium. Pressure was measured optically using ruby chips (Al_2O_3:Cr^{3+}) [Mao, 1978].

To generate the higher pressures for the EDX spectra, diamond anvils with culets bevelled to 5° were used. The flat central region was 100 μm in diameter, so a 75 μm hole was drilled in the preindented gasket. A polycrystalline sample obtained by grinding a single crystal was inserted in the DAC, with some Pt for pressure calibration and silicone oil as a pressure transmitting medium.

4.1.3 Experimental Setup

Raman spectra were obtained using the 488 nm line of an Ar^+ laser in a back-scattering geometry. They were recorded using a Jobin-Yvon S-3000 spectrometer and a liquid nitrogen cooled CCD detector. The spectrometer slits were adjusted to keep a spectral width of roughly 2 cm^{-1} throughout the experiment. The laser was focused using either a 10× or a 23× Leitz objective: initially, the focus spot was 50 μm in diameter, but was decreased to 20 μm above 52 GPa to reduce the effect of a small pressure gradient on the sample. This improved the quality of the spectra, for which several lines were once again clearly resolved. The laser power was adjusted from 30 mW to 90 mW at the sample to compensate for the weakening of the signal with increased pressure. Integration time was kept relatively constant, sufficiently long to get spectra with suitable statistics.

The EDX diffraction spectra were obtained at CHESS using the same setup as the other EDX experiments we have performed (§2.2.2).

4.1.4 Results and Discussion

Figure 4.1 and Figure 4.2 show the evolution of the spectrum and the Raman shifts with increasing pressure, exhibiting the presence of at least the three known high-pressure polymorphs of TiO_2. The Raman shifts of each of the three phases are given at several pressures in **Table 4.1** . Additionally, above 60 GPa, **Figure 4.1** displays a major change in the intensity of a line near 300 cm^{-1} as well as significant modifications in the rest of the spectrum, showing the possible appearance of a new phase, as reported by Endo *et al.* The X-ray diffraction spectrum at 105 GPa (**Figure 4.3**) also shows the presence of a new reflection between the baddeleyite $(11\bar{1})$ and (111) reflections, with a d-spacing of 2.47 Å. This is the same d-spacing as that reported by Endo *et al.* and is clear evidence for a new high-pressure form.

Table 4.1 Raman shifts in the three high pressure phases of TiO_2 at selected pressures. The columbite-type structure at atmospheric pressure is the quenched phase.

Phase	**TiO_2 I**	**TiO_2 II**		**TiO_2 III**	
Structure	**Anatase**	**Columbite**		**Baddeleyite**	
Pressure (GPa)	**0.1**	**9.8**	**10^{-4}**	**25.9**	**63.0**
Raman shifts (cm^{-1})	137.8 E_g	164.4	145.3	209.6	220.8
	193.2 E_g	178.9	169.4	218.7	267.3
	392.6 B_{1g}	192.3		238.1	280.8
	513.7 A_{1g}/B_{1g}	268.5	283.7	266.0	291.8
	635.6 E_g	289.4			306.8
		311.0	310.9	283.4	347.1
		345.6	335.2	325.5	354.2
		376.1	351.9		381.6
		441.7	406.7	393.4	423.7
		451.9	424.0	439.3	474.5
		481.0	440.9	455.0	493.3
		579.5	528.0	492.3	541.4
		619.1	567.4	501.2	564.7
		652.6	609.1	527.6	582.8
		680.3		670.5	714.1
				726.6	774.2
				767.2	821.7
					916.0

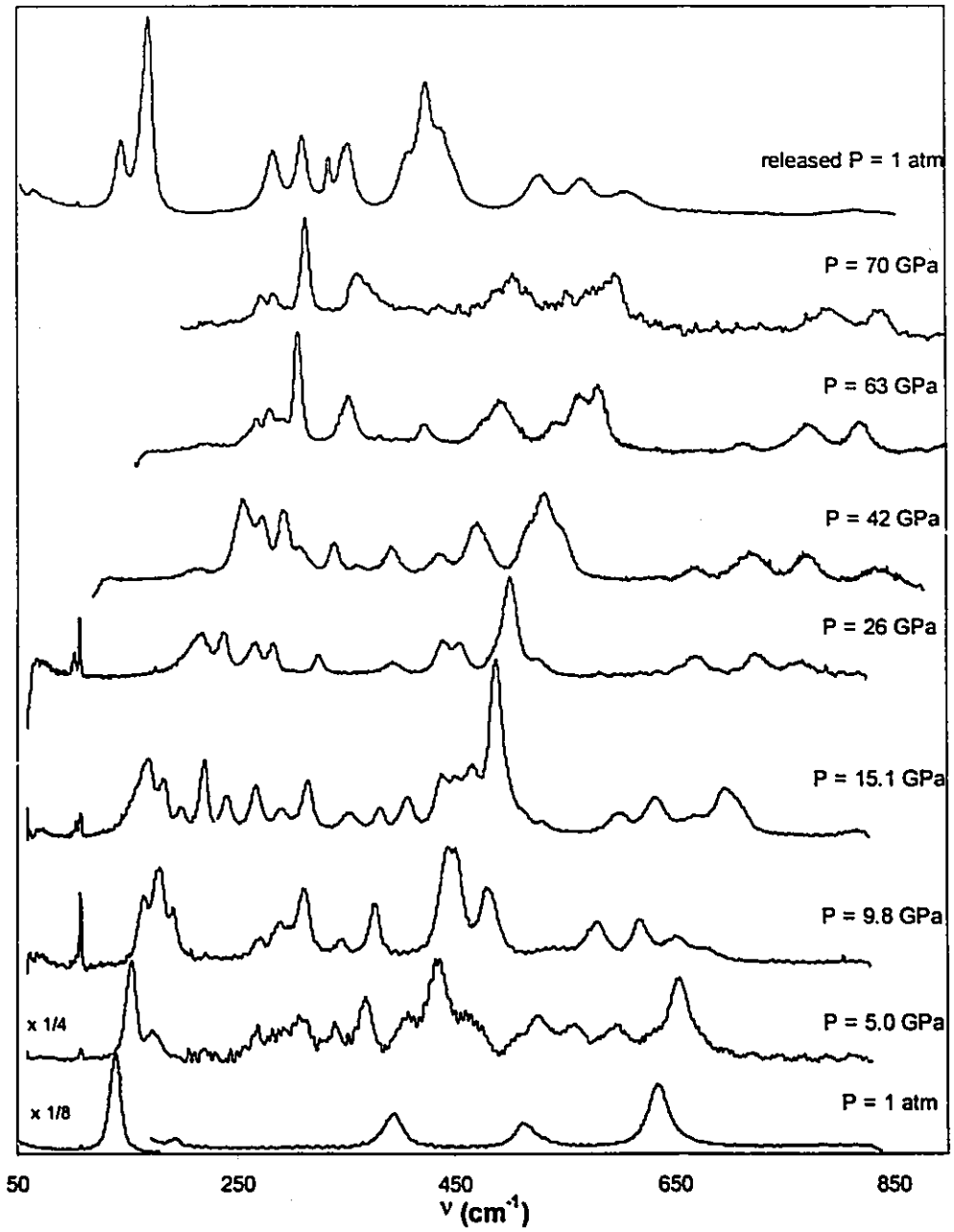

Figure 4.1 Raman spectra of TiO_2 at selected pressures. The initial structure is anatase, which transforms to a columbite-type structure around 5 GPa. Between 12 GPa and 15 GPa, this phase transforms to a baddeleyite-type structure. Above 60 GPa, the important change in relative intensities of the lines around 300 cm^{-1} clearly indicates some modification of the structure, possibly evolving to a fluorite-type structure which is expected to comprise only 4 Raman-active modes. When the pressure is released, the sample reverts to the columbite-type structure which is quenched at atmospheric pressure.

4.1.4.1 The Anatase Phase

The Raman spectrum of anatase is very simple, comprising only five peaks (**Figure 4.1** and **Table 4.1**), of which one is very weak (@ 193 cm^{-1}). Just before 5 GPa, a substantial number of new peaks appear, marking the transition to the TiO_2 II phase which has an α-PbO_2 type structure. The lines from the anatase phase disappear within 2 GPa, resulting in a rapid transition. This transition occurs much faster in our single crystal experiment than in other powered samples experiments [Gou 1989, Haines 1993] which describe a sluggish transition. Around 7 GPa, there is no sign of the anatase phase and the α-PbO_2 type phase can be readily quenched, which is clearly different from Gou *et al.*'s results showing only a partial transition to TiO_2 II when quenching from 17 GPa [Gou 1989].

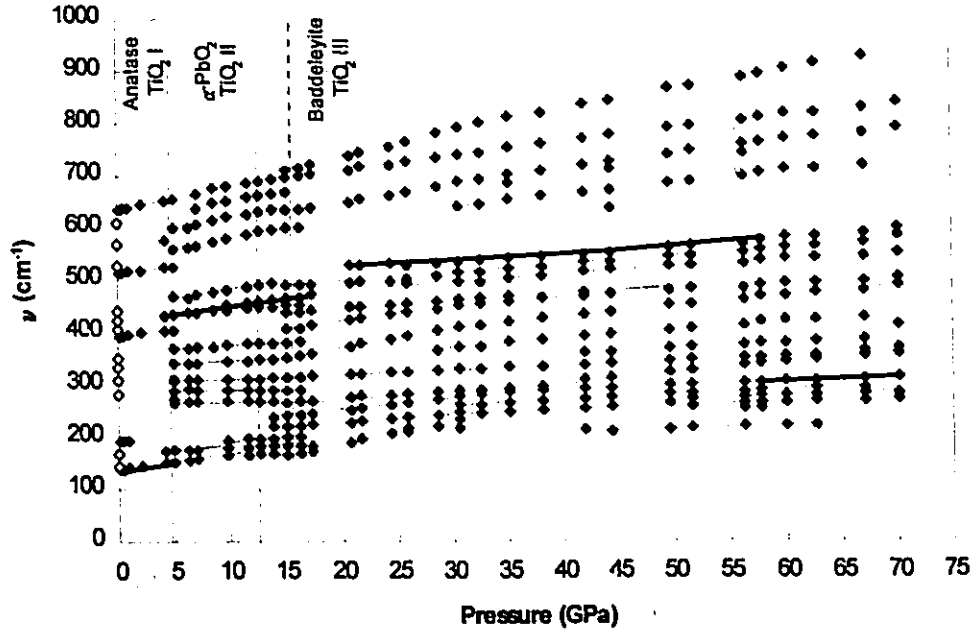

Figure 4.2 Evolution of the Raman shifts in TiO_2 with increasing pressure. Each phase's range is indicated, with the overlap corresponding to the more sluggish II→III transition. The quenched phase's shifts are also indicated.

4.1.4.2 The Columbite-Type (α-PbO_2) Phase

The TiO_2 II phase is characterized by 14 Raman lines at 9.8 GPa. Compared to the quenched, atmospheric pressure spectrum, two new lines appear from shoulders of the lines at 170 at 284 cm^{-1}. As reported previously, this phase can be quenched to atmospheric pressure, resulting in a polymorph that is sometimes found naturally. During the I → II transition, the crystal has broken into several smaller crystallites, probably because of small pressure gradients within the sample. At 13 GPa, several new lines start appearing, indicating the transition to the TiO_2 III phase.

4.1.4.3 The Baddeleyite-Type Phase

Between 13 and 17 GPa, several new lines appear, while several TiO_2 II lines vanish, marking the emergence of yet another high pressure polymorph, labelled TiO_2 III. Using *in situ* X-ray diffraction, Sato *et al.* [1991] have definitely identified TiO_2 III as having a baddeleyite-type structure. When performing Raman spectroscopy experiments, Arashi pointed out that the Raman spectrum of TiO_2 III had features which were characteristic of the ZrO_2 and HfO_2 baddeleyite-type structures' Raman spectra [Arashi, 1992]. The Raman spectrum at 26 GPa can be compared to the spectra of ZrO_2 I and HfO_2 I from chapter 3, and the same conclusion can be reached. After this transition, the monoclinic phase has been refined up to 49 GPa [Haines, 1993] and observed (by the $(11\bar{1})$ reflection) up to 105 GPa [Endo, 1993].

The existence of a monoclinic phase at such high pressures is surprising because it has a low symmetry compared to other typical structures obtained in high pressure polymorphs of MO_2 compounds. For example, SnO_2 undergoes the following phase transitions under pressure [Liu, 1986]

rutile → columbite → fluorite

and RuO_2 also transforms to a fluorite structure [Léger]

rutile → orthorhombic ($CaCl_2$-type) → fluorite

It is thus expected that TiO_2 would also ultimately transform to a fluorite structure. Using molecular dynamics and first principals calculations, Tse and Klug determined that TiO_2 should ultimately transform to the 8-coordinated fluorite structure [Tse, 1993].

The existence of a baddeleyite-type structure in the TiO_2 phase diagram seems to indicate that TiO_2 is a link between the two types of dioxide compounds. In this case, TiO_2 might evolve like a typical rutile-type compound and then, when reaching the baddeleyite-type phase, continue transforming like ZrO_2 and HfO_2. Higher pressure modifications should thus be expected.

When studying TiO_2 to pressures up to 105 GPa using *in situ* X-ray diffraction and Raman spectroscopy, Endo *et al.* observed a new modification above 80 GPa, which coexisted with the monoclinic phase up to 105 GPa [Endo, 1993]. Even though a clear phase transition is not definite in their Raman spectroscopic data, there is a change in several peaks' intensities. In our Raman experiment, we also see substantial changes in relative intensities of several peaks above 60 GPa. In particular, of the group of peaks around 300 cm^{-1} one of them grows substantially to become the strongest peak in the spectrum, whereas the other peaks fade away. Another distinctive feature is a peak which grows out of the shoulder of another and also becomes very intense. At 70 GPa, the spectrum comprises mainly 6 peaks, with

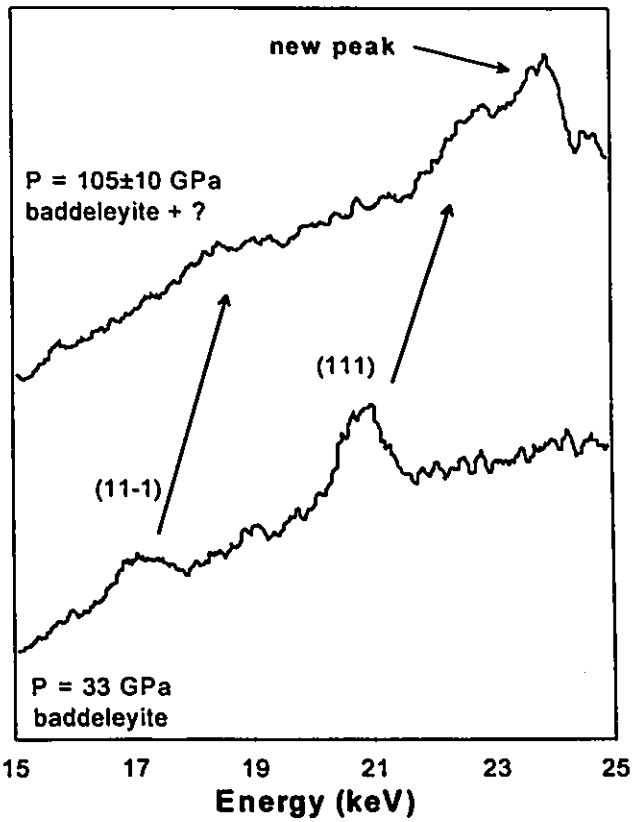

Figure 4.3 EDX diffraction spectra of TiO_2 showing the appearance of a new peak with d = 2.47 Å at 105 GPa.

some additional very small peaks. This spectrum has the same features as that obtained by Endo *et al.*

To verify the appearance of a new peak in the range of 100 GPa, new diamond anvils had to be used to record the proposed transition. Some scarce EDX data were taken with sole purpose to try to see this new peak. **Figure 4.3** represents a part of two spectra obtained at 33 GPa (pure monoclinic) and 105 GPa, where a new peak is clearly visible. No other special features could be discerned from the rest of the spectrum, where most peaks had become too large and too weak to clearly identify. When returning to atmospheric pressures to new peak disappeared and the sample reverted to a columbite-type structure. At 102 GPa, the new peak is observed at d=2.47 Å, which is the same value as the one obtained in the study by Endo *et al.* This new modification of TiO_2 seems quite evident.

4.1.5 Conclusion

The pressure behaviour of single crystals of anatase TiO_2 has been studied using Raman spectroscopy and X-ray diffraction. The results obtained are in good agreement with the results obtained in other studies of TiO_2. However, in regards to the first transformation, it is the first time that it could be observed for a single crystal. The effect of the crystallinity is quite clear: it makes it a fast transition, rather than a sluggish one as observed in powdered samples studies. Very high quality high pressure Raman spectra of the baddeleyite-type phase were obtained up to 70 GPa, illustrating the appearance of a new modification above 60 GPa. The X-ray diffraction data also confirmed the assertions of Endo *et al.* regarding this new phase transition. Unfortunately, an identification of the structure could not be made. Upon reversal of the pressure, the baddeleyite-type phase transforms to the α-PbO_2 type phase at 5 GPa, showing a significant hysteresis.

4.2 Equations of State of TiO_2 High Pressure Phases from *in situ* Energy Dispersive X-ray Diffraction Measurements

4.2.1 Introduction

As mentioned in the preceding section, at room temperature, TiO_2 adopts two known high pressure structures, besides the atmospheric pressure polymorphs. Rutile is the most common natural mineral of TiO_2. The tetragonal rutile structure belongs to the space group $P4_2/mnm$ and contains two TiO_2 groups per unit cell. The Ti atoms, located at (0, 0, 0) and (½, ½, ½), are each surrounded by a slightly distorted octahedron of O atoms. These TiO_6 octahedra form the basic grouping in the various polymorphs of TiO_2, which differ mainly in the number of edge-shared octahedra (2 in rutile, 3 in brookite and 4 in anatase and the columbite-type structure). For this reason, the coordination of Ti atoms with O atoms is 6 for all four structures. In rutile, the adjacent octahedra are arranged in ribbons in the [110] direction, whereas in anatase, the octahedra produce a zig-zag pattern perpendicular to the c direction [Glassford, 1992]. **Table 4.2** gives a description of the structural properties of each polymorph.

Table 4.2 Structural properties of the atmospheric pressure polymorphs of TiO_2

Structure	a (Å)	b (Å)	c (Å)	Space group	Z	Ref.
Rutile	4.5936	-	2.9587	$P4_2/mnm$	2	[Abrahams, 1971]
Anatase	3.7852	-	9.5139	$I4_1/amd$	4	[PDF]
Brookite	5.4558	9.1819	5.1429	*Pcab*	8	[PDF]
Columbite-type	4.55	5.46	4.92	*Pbcn*	4	[Linde, 1969]

In light of the structural differences between rutile and anatase, one might expect these structures to behave quite differently when applying pressure. In the previous section, the phase transitions of anatase were studied by Raman spectroscopy. In this section, we will establish the pressure dependence of rutile and anatase by X-ray diffraction measurements. By using powdered samples, we will also determine if the degree of crystallinity of the sample affects the transition rates and pressures in anatase.

4.2.2 Sample Preparation and Experimental Procedure

The anatase powder was obtained by grinding crystals which were grown by chemical vapour transport reactions [Berger, 1993]. These crystals were shown to contain only the anatase phase, as observed by Raman spectroscopy. The rutile powder was obtained from Johnson-Matthey, and are stated to be 99.999% pure. Their purity of phase was also verified by Raman spectroscopy.

Energy dispersive measurements were performed using synchrotron radiation at the CHESS B1 station, in the setup detailed in chapter 2. In all cases, small quantities of the sample were inserted into the pressure chamber of a DAC with 300 μm culets. A standard AISI T301 gasket was used, as were ruby chips for pressure calibration. A 4:1 mixture of methanol and ethanol was used as a pressure transmitting medium.

4.2.3 Results and Discussion

Figures 4.4 through **4.7** show the EDX diffraction spectra of TiO_2 starting from the rutile phase and the anatase phase. **Figure 4.8** shows the pressure dependence of the rutile phase up to 20 GPa, with the fitted Birch-Murnaghan EOS results, and **Figure 4.9** shows the evolution with pressure of the lattice parameters of rutile. The only actual results which could be obtained through these experiments were the transition pressures, the pressure range of the transition, and an EOS modelling of the rutile phase. An EOS could also be obtained for the

anatase phase, from three spectra with the anatase phase, hence the results are very uncertain and very dependent on any possible calibration error for a spectrum. For reference, with $B_0' = 5$, a bulk modulus of 350 ± 100 GPa was obtained for the anatase phase.

When starting with the anatase phase, the same transitions as observed with Raman spectroscopy are observed here. However, as observed in other experiments [Gou 1989, Haines 1993] with fine powdered samples, the transition from the anatase phase to the columbite-type phase is much more sluggish than when we observed it in the single crystal Raman spectroscopy experiment. An additional interesting artifact in these spectra is the change in the anatase spectra which is due to the low polycrystallinity of the sample: only several grains of the crushed single crystals were used as a sample, resulting in important preferred orientation and possible poor powder averaging effects. Recall than in EDX measurements, only a very small portion of the Debye ring is detected, so a *spotty* spatial diffraction ring (at a specific energy) might not be detected. This, incidentally, is a great problem of the EDX method, since the small samples used in high pressure experiments often result in poor powder averaging. The anatase transforms to a columbite-type phase between pressures of 4.5 and 12 GPa (there are still traces of anatase at 12 GPa). The columbite-type phase was confirmed by the presence of peaks at the correct energies. However, because of the low resolution of the spectra, a good identification of the peak positions was rare (mostly because of doublets in the structure's spectrum) and thus the determination of the lattice parameters was not very accurate. Around 15 GPa, the baddeleyite-type phase appears, characterized by the $(11\bar{1})$ and (111) peaks near 23 and 28 GPa respectively. Once again, this is a low symmetry (monoclinic) structure which has many overlapping peaks, so an accurate determination of the lattice parameters was impossible.

When starting with the rutile phase, the transition to the columbite-type phase does not occur, as observed by Sato *et al.* [1991]. In several other studies of rutile [Bendeliani 1966, Mammone 1980, Arashi 1992] the new columbite-type phase was observed at a pressure around 10 GPa. In most cases is there a consensus that the grain size and degree of crystallinity of the sample had an important effect regarding the pressure of the transition and the possible

non-existence of the transition, in that very small grains delay the transition pressure, whereas single crystal measurements clearly indicate the transition. At 12 GPa, the baddeleyite phase appeared, but the rutile phase was still observed at 20 GPa. In the study where he identified this phase as having a baddeleyite-type structure, Sato *et al.* [1991] had to heat the sample at 20 GPa to 770°C to eliminate the remaining rutile phase. Once again, the baddeleyite-type phase was identified by ascertaining the positions of the expected peaks. It was also clearly characterized using Raman spectroscopy by Arashi [1992] and ourselves.

With the unfortunate quality of the data, we were only capable of determining the EOS parameters for the rutile phase. According to high precision ultrasonic measurements on single crystals [Manghnani, 1969], the bulk modulus of rutile is $B_0 = 211 \pm 0.07$ GPa, with $B_0' = 6.84$. With the data acquired during several runs, a calculated value of $B_0 = 243 \pm 22$ GPa was obtained, for data between 0 and 20 GPa. The values for the volume and B_0' were kept constant at 62.432 Å^3 and 6.84, respectively.

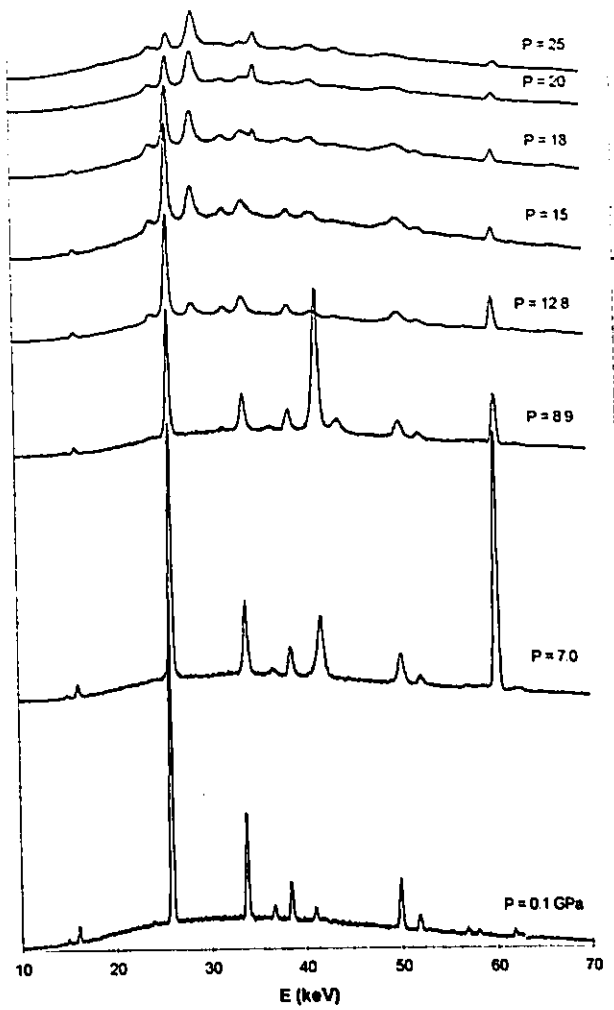

Figure 4.4 EDX diffraction spectra of TiO_2 starting from the rutile phase.

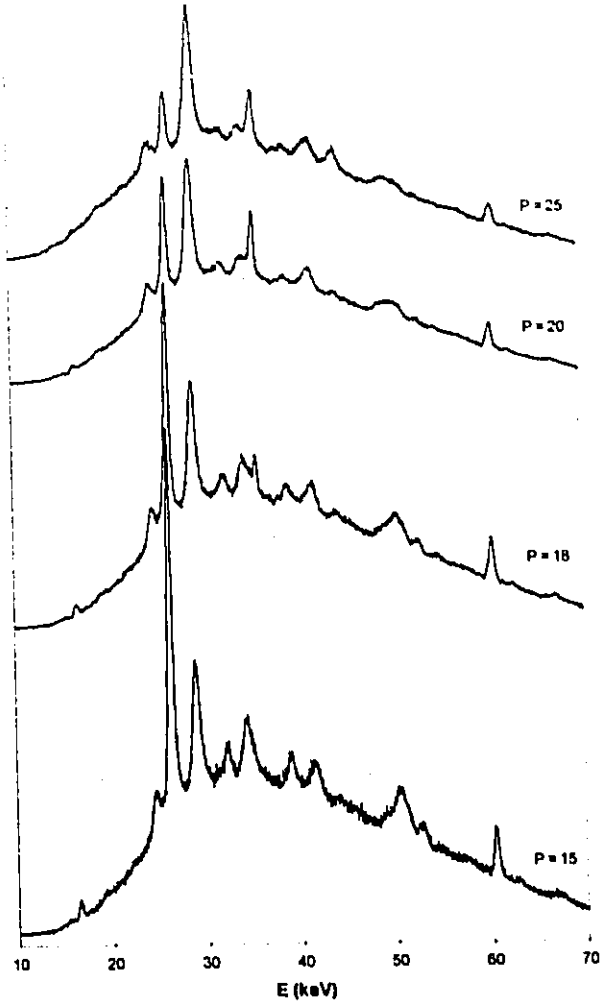

Figure 4.5 Enhanced view of the higher pressure spectra showing the appearance of the baddeleyite-type phase and the persistence of the rutile phase.

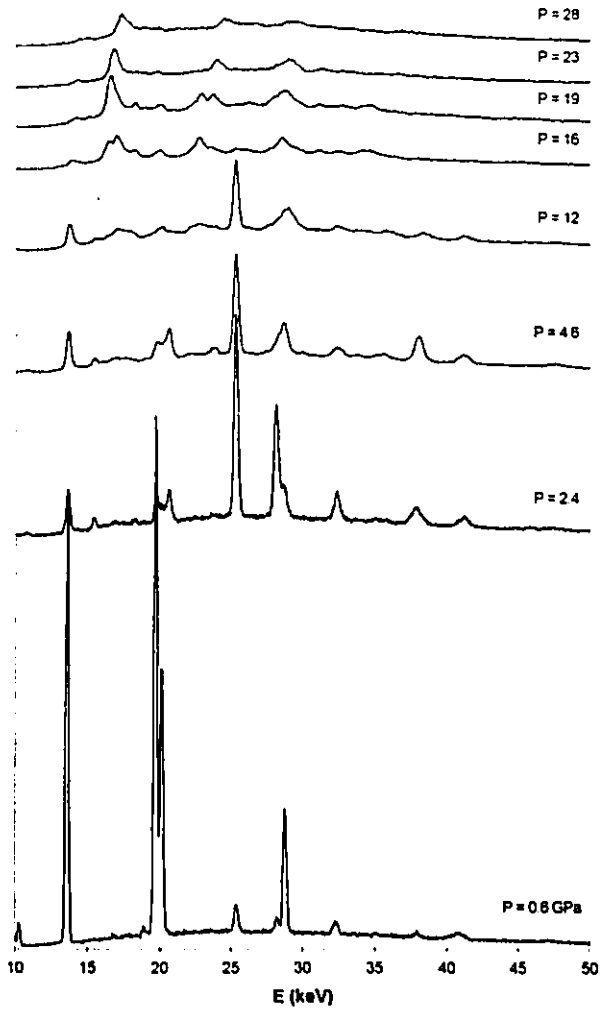

Figure 4.6 EDX diffraction spectra of TiO_2 starting with the anatase phase. These spectra show the slower transition rate of the transition from anatase to the columbite-type phase compared to this transition observed from a single crystal of anatase.

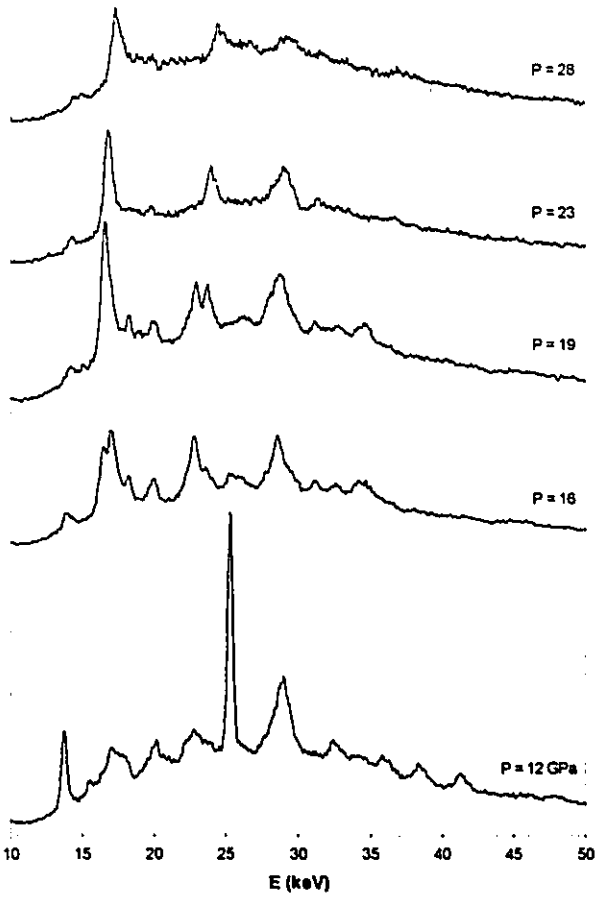

Figure 4.7 Enhanced view of the spectra, showing the columbite-type (α-PbO_2-type) and the baddeleyite-type phases. These spectra also show the low resolution of these low-symmetry phases which made an EOS analysis infeasible.

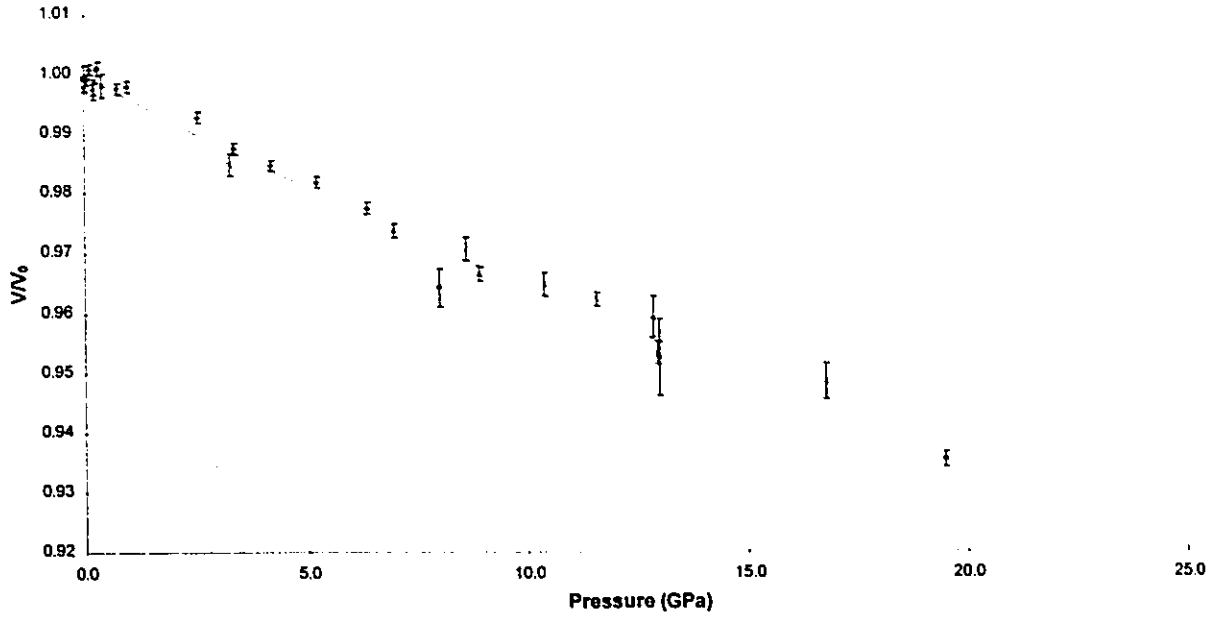

Figure 4.8 Pressure dependence of the relative volume of rutile. The various symbols correspond to different runs. The solid line corresponds to a fit to the Birch-Murnaghan EOS, resulting in $B_0 = 243 \pm 22$ GPa ($B_0' = 6.84$).

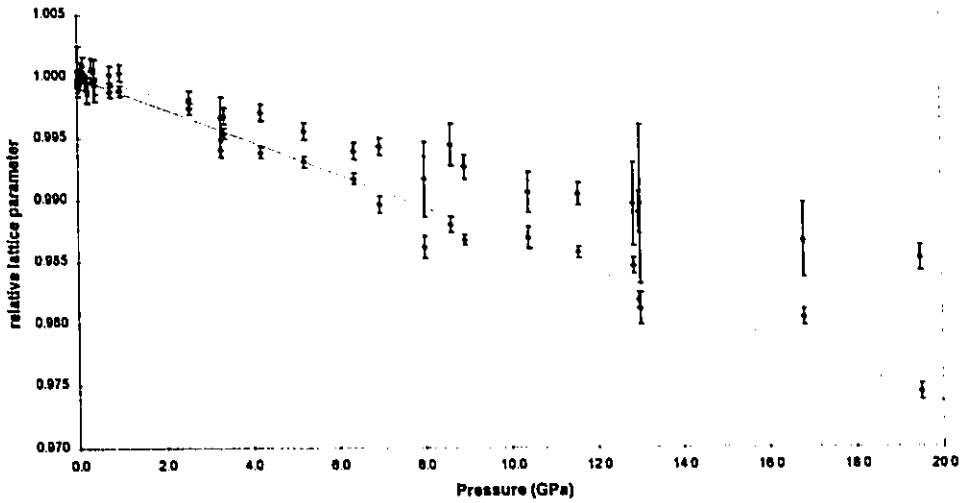

Figure 4.9 Evolution of the lattice parameters in rutile TiO_2, normalized to their null pressure values. The open symbols correspond to a/a_0, and the solid symbols to c/c_0. The lines correspond to linear fits to the data, yielding compressibilities of $1.28(\pm 0.08)\cdot 10^{-3}$ GPa^{-1} for a/a_0 and $0.81(\pm 0.15)\cdot 10^{-3}$ GPa^{-1} for c/c_0, compared to values of $1.64\cdot 10^{-3}$ and $0.91\cdot 10^{-3}$ GPa^{-1} as obtained by Ming *et al.* [1979]. This clearly shows the lower compressibility of the structure along the c axis due to the arrangement of the TiO_6 octahedra.

4.2.4 Conclusion

A study of TiO_2 using energy dispersive X-ray diffraction was performed on powdered samples of anatase and rutile. The anatase sample was observed to transform to a columbite-type structure between 4.5 and 12 GPa. The sluggishness of this transition indicates how dependent it is on the degree of crystallinity of the anatase. This phase then transformed to the baddeleyite-type phase around 15 GPa. In the rutile sample, no transition to the columbite-type structure occurred. Instead, a partial transition to the baddeleyite-type structure is observed, starting at 12 GPa. The rutile phase coexists with this new phase to at least 20 GPa. The bulk modulus of rutile was thus determined as being $B_0 = 243 \pm 22$ GPa ($B_0' = 6.84$), in very good agreement with the value given in the literature.

Appendix A

X-Ray Diffraction Intensity Calculations

A.1 Powder Diffraction Intensity Calculations

According to chapter 2, when the crystal lattice is known, one can generate d-spacings for all possible Miller index combinations and find their equivalent in an angle or energy dispersive spectrum. However, the internal structure of the unit cell has not yet been taken into account. Since the diffraction occurs at the atomic level, the positions of atoms in the cell will determine which planes actually diffract, as well as the intensity of the scattered light, depending on the scattering power of the atoms.

A.1.1 Monatomic Structure Factor

Consider the electric field of an incident x-ray beam $\vec{E}_{\vec{k}}$ with wave vector $\vec{k}$ on a crystal containing identical atoms at positions $\vec{r}_i$. These atoms act as point sources and scatter the beam in all directions $\vec{k}'$ with an initial phase depending on $\vec{k}\cdot\vec{r}$. The sum of all diffracted beams scattering in a direction $\vec{k}'$ is then given by (not considering possible polarization effects during scattering):

$$\begin{aligned}
\vec{E}_{\vec{k}'}(\vec{R}) &= \sum_j \vec{E} e^{i\vec{k}\cdot\vec{r}_j} \frac{e^{i\vec{k}'\cdot(\vec{R}-\vec{r}_j)}}{|\vec{R}-\vec{r}_j|} \\
&\approx \frac{1}{R}\sum_j \vec{E} e^{i(\vec{k}-\vec{k}')\cdot\vec{r}_j} e^{i\vec{k}'\cdot\vec{R}} \quad \text{if } R \gg r_j, \forall j \\
&= \frac{\vec{E} e^{i\vec{k}'\cdot\vec{R}}}{R} \sum_j e^{i(\vec{k}-\vec{k}')\cdot\vec{r}_j} \\
&= \vec{E}_{\vec{k}'}(\vec{R}) \sum_j e^{i\vec{K}\cdot\vec{r}_j} \quad \text{where } \vec{K}=\vec{k}-\vec{k}',
\end{aligned} \tag{A.1}$$

where $\vec{E}_{k'}(\vec{R})$ is simply a beam from a point source far enough away from the crystal ($R \gg r_j$) and the summation is over all atoms in the crystal. This essentially represents a sum of incoherent beams which will cancel out, *i.e.* interfere destructively, for any $\vec{K}$, except those specified by Bragg's law (in terms of $K = \frac{2\pi}{\lambda}$, plus a specific orientation of the crystal), for which the atoms form planes that create a constructive interference of the beams. Now consider those $\vec{K}$ which do diffract. By definition of the Bravais lattice, each of the N unit cells containing n atoms can be defined by a translation through a Bravais lattice vector (an integer linear combination of the $\{\vec{a}_i\}$) of another unit cell. In these conditions, any atom in the crystal is an atom in a specific cell (taken as the origin) translated by those vectors. The beam amplitude therefore can be greatly simplified:

$$\begin{aligned}\frac{\vec{E}'_{k'}(\vec{R})}{\vec{E}_{k'}(\vec{R})} &= \sum_{j}^{Nn} e^{i\vec{K}\cdot\vec{r}_j} \\ &= \sum_{m}^{N}\sum_{j}^{n} e^{i\vec{K}\cdot(\vec{r}_j^{\,0}+\vec{R}_m)}, \text{ where } \vec{R}_m = \sum n_i\vec{a}_i \\ &= \sum_{m}^{N}\sum_{j}^{n} e^{i\vec{K}\cdot\vec{r}_j^{\,0}} e^{i\vec{K}\cdot\vec{R}_m} \\ &= N\sum_{j}^{n} e^{i\vec{K}\cdot\vec{r}_j^{\,0}}, \text{ since } \vec{K}\cdot\vec{R}_{Bravais} = 2\pi l.\end{aligned} \tag{A.2}$$

The diffracted beam's amplitude can then be calculated according to a sum limited to the atoms in one unit cell, and that summation is known as the *geometrical structure factor:*

$$S_{\vec{K}} = \sum_{j=1}^{n} e^{i\vec{K}\cdot\vec{r}_j}. \tag{A.3}$$

Already we can see why some calculated Bragg peaks might not appear in an actual spectrum of crystals of a particular space group, because the summation for a particular plane, or $\vec{K}$, might be zero.

A.1.2 Polyatomic Structure Factor

If the atoms in the structure are not the same, then the intensity of the scattered beam will not be the same, so we must include an *atomic form factor* to get a valid structure factor. As previously stated, the scattering occurs at the level of the electrons, whereas the structure factor was considered for identical point source atoms. To get a correct structure factor, we should do the same derivation by using electron positions rather than atomic positions. However, we couldn't do a sum because of the delocalization of electrons, so we should integrate on the charge density of the cell. It is easy to show, however, that it can be reduced to an integral over the charge density around each atom, and summed over the atoms in the unit cell:

$$S_{\vec{K}} = \sum_{j=1}^{n} e^{i\vec{K}\cdot\vec{r}_j} \rightarrow \propto \frac{1}{V}\int_{cell} \rho(\vec{r}) e^{i\vec{K}\cdot\vec{r}} d\vec{r}$$

$$\text{but } \rho(\vec{r}) = \sum_{j=1}^{n} \rho_j(\vec{r} - \vec{r}_j)$$

$$\rightarrow S_{\vec{K}} \propto \frac{1}{V}\sum_{j=1}^{n}\int_{\Omega_j} \rho_j(\vec{r}_a) e^{i\vec{K}\cdot(\vec{r}_a + \vec{r}_j)} d\vec{r}_a \qquad \text{(A.4)}$$

$$\propto \frac{1}{V}\sum_{j=1}^{n} e^{i\vec{K}\cdot\vec{r}_j}\int_{\Omega_j} \rho_j(\vec{r}_a) e^{i\vec{K}\cdot\vec{r}_a} d\vec{r}_a$$

$$\text{finally, } S_{\vec{K}} = \sum_{j=1}^{n} f_j(\vec{K}) e^{i\vec{K}\cdot\vec{r}_j},$$

where f_j is known as the *atomic form factor*:

$$f_j = -\frac{1}{e}\int d\vec{r}\; e^{i\vec{K}\cdot\vec{r}} \rho_j(\vec{r}), \qquad \text{(A.5)}$$

which shows that for $\vec{K} = 0$, $f_j = Z_j$, the number of electrons in the neutral atom. Tables of calculated atomic form factors are available in literature for all atoms and some common ions for various values of K.

According to the Laue condition for diffraction (§2.1), $\vec{K}$ is a vector perpendicular to the (*hkl*) plane and can be expressed as $\vec{K} = m(h\vec{a}^* + k\vec{b}^* + l\vec{c}^*)$ for an *m*th order diffraction. If the atomic positions are expressed in terms of the unit cell vectors $\vec{r}_j = x_j\vec{a} + y_j\vec{b} + z_j\vec{c}$, then we have $\vec{K}\cdot\vec{r}_j = 2\pi m(hx_j + ky_j + lz_j)$. This notation will be used whenever it is more convenient, that is when referring to an explicit (*hkl*) plane.

A.1.3 Isotropic and Anisotropic Thermal Factors

Atomic vibration due to thermal activation will also affect the structure factor, since the apparent electron distribution will be expanded as a larger average distribution, which affects the atomic form factor. Two models are usually proposed to estimate that effect: assigning to each atom an isotropic thermal parameter *B* or defining six anisotropic thermal parameters b_{ij}. The structure factor now becomes:

$$S_{\vec{K}} = \sum_{j=1}^{n} f_j(\vec{K})\,\Theta_j(\vec{K})\,e^{2\pi i(hx_j + ky_j + lz_j)}, \qquad \text{(A.6)}$$

where $\Theta(\vec{K}) = e^{-B\left(\frac{1}{2d_{hkl}}\right)^2}$ in the isotropic case, or $\Theta(\vec{K}) = e^{-(b_{11}h^2 + b_{12}hk + b_{13}hl + b_{22}k^2 + b_{23}kl + b_{33}l^2)}$. According to these equations, the peaks of smaller d-spacings are more reduced, as would be expected: the thermal motion of the atoms is relatively more important for planes that are very close rather than for planes relative to which the actual atomic radii are small.

A.1.4 Multiplicity Factor

When calculating the intensity of the peak from a given plane, we must also take into account the basic symmetries of the crystal system for degeneracies. As an example, consider a tetragonal lattice, and its (100), (010) and (001) planes. Because a=b in a tetragonal lattice, (100) and (010) have the same d-spacing and will both contribute to the same peak. To avoid these repetitive indices, only (100) will be used, knowing it also corresponds to (010) and its multiplicity must be double that of the (001) plane for this reason. However, we must realize

that (100) represents planes (100), (010), ($\bar{1}$00) and (0$\bar{1}$0) while (001) represents only (001) and (00$\bar{1}$). The multiplicity of (100) is thus 4, whereas the multiplicity of (001) is two for a tetragonal structure. In a triclinic system, all peaks have equal multiplicities because there are no explicit (non accidental) degeneracies. Tables of multiplicities for (*hkl*) planes in a given crystal system are well known and available [Kittel, 1986]. The calculated intensity of the peak must thus be multiplied by its multiplicity factor.

A.2 Angle Dispersive Specific Factors

A.2.1 Lorentz and Polarization Factors

The interaction between x-rays and atoms does not result in isotropic scattering, so the intensity intrinsically depends on the angle at which it is scattered. The factor taking this anisotropy into account is the *polarisation factor*, which is given by $p = \cos 2\theta$ when the incident beam is not polarized, or $p = \frac{1}{2}(1 - \cos^2\theta)$ when it is vertically polarized. Also, as seen previously, the diffraction produces a ring which contains the total diffracted beam. When using standard diffractometers, only a part of the ring is actually measured, so the calculated intensity must be corrected to take into account only the portion that is measured. This is the *Lorentz factor*. In most cases, for a given geometry, both parameters, which depend solely on the angle of diffraction, are specified as the Lp factor. Its form for several common diffraction geometries is:

$$Lp(2\theta) = \frac{1}{2}\frac{1+\cos^2\theta}{\sin\theta}. \qquad \text{(A.7)}$$

Since this is not the correct Lp factor for our setup with imaging plates, we must correct our observed data according to it for use in a Rietveld analysis program.

This is the only factor specific to angular dispersive experiments that we need to consider. If we really needed a more precise calculation, we could also include an absorption factor from the sample, the Be support plate and the down stream diamond of the DAC to take into account the extra thickness travelled through as a function of the diffracted angle. However, for the wavelength at which we were working, the absorption is very small and does not have a significant impact on the observed spectrum.

A.3 Energy Dispersive Specific Factors

A.3.1 Synchrotron Source

In our case, we used synchrotron radiation for energy dispersive measurements. According to Appendix B, the intensity of the source is given by

$$S(E) = I_{sync}(E) \propto \left(\frac{E}{\varepsilon_c}\right)^2 K_{\frac{2}{3}}\left(\frac{E}{2\varepsilon_c}\right)^2, \tag{A.8}$$

in which ε_c is the critical energy of the source and $K_{2/3}(x)$ is the Modified Bessel function of order 2/3.

A.3.2 Sample Absorption

Any material absorbs x-rays according to

$$A(E) = 1 - e^{-\frac{\mu}{\rho}\rho t}, \tag{A.9}$$

where μ is known as the absorption or attenuation coefficient and μ/ρ is the massic absorption coefficient. In most cases, μ/ρ can be very closely approximated by

$$\frac{\mu}{\rho} \approx a_1\lambda^3 - a_2\lambda^4, \tag{A.10}$$

between two shell energies (usually the K and possibly the L shells), where a_1 and a_2 are constants which are commonly tabulated for various atomic species. Recall that $\lambda = 12.399/E$. At a given shell energy, the absorption factor rises abruptly because the shell electrons now become available.

A.3.3 Detector Efficiency

The detector we use is a high purity planar Ge detector, sealed by a Be window of thickness 1 mm. The detection process itself involves only the ability of the detector to absorb the photons, so its efficiency depends mostly on its absorption factor. Because there is a Be window in front of the Ge crystal, it will absorb photons that will not be counted in the detection process. Additionally, for energies larger than 11.1 keV, the production of escape peaks impedes the efficiency of the detector, because the peak energy will not be correct. The ratio of escape peaks with respect to the number of incoming photons $\frac{N_e}{N}$ is 16% at 11.1 keV and diminishes rapidly to 0% for higher energies. The total efficiency in this case is thus

$$D(E) = Eff(E) = (1 - e^{-\mu_{Ge} t_{Ge}}) e^{-\mu_{Be} t_{Be}} \left(\frac{1}{1 + \frac{N_e}{N}} \right). \qquad \text{(A.11)}$$

A.4 General Intensity Formulation

In chapter 2, we have discussed the preferential orientation factor, but we have not given any specific model, primarily because they are only empirical models. This factor will be dependant exclusively on the orientation of a plane, that is its Miller indices, and it essentially accentuates peaks whose planes are parallel to the thread axis, while diminishing those perpendicular to it, according to a chosen distribution. When modelling preferred

orientation, we used the March-Dollase function, where the correction factor is

$$P(hkl) = (r^{3/2}\cos^2\alpha + \frac{1}{r\sin^2\alpha})^{-3/2}, \text{ where } \cos\alpha = h\vec{k}l\cdot P\vec{O}.$$

We can now establish, for our needs, a master formulation of the calculated intensity of a peak characterized by (*hkl*) and E or 2θ:

- for angle dispersive measurements,

$$I_{hkl}(2\theta) = aP(hkl)\,m_{hkl}\left|\sum_{atoms\ j} f_j(d_{hkl})\Theta_j(d_{hkl},hkl)e^{2\pi i(hx_j+ky_j+lz_j)}\right|^2 Lp(2\theta), \qquad \text{(A.13)}$$

- for energy dispersive measurements,

$$I_{hkl}(E) = aP(hkl)\,m_{hkl}\left|\sum_{atoms\ j} f_j(d_{hkl})\Theta_j(d_{hkl},hkl)e^{2\pi i(hx_j+ky_j+lz_j)}\right|^2 T(E)\,D(E)\,S(E), \qquad \text{(A.14)}$$

where *a* is a scale factor for all peaks from the same structure (phase, sample, *etc*). The parameters which depend on d_{hkl} or *hkl* are specific to the structure , whereas those that are instrumental or geometric factors specific to experimental conditions depend on the positioning on the measuring instrument (2θ or E).

A.5 Peak Widths and Shapes

We have not yet discussed the widths and shapes of the calculated peaks for a simple reason, they are a convolution of different response functions and the intrinsic peak profile shape and incident wavelength distribution. The incident beam shape, dependant on how the radiation is produced, is itself affected by a monochromator, several slits or collimators and the geometry in which the diffraction takes place. The various response functions involved can be spatial, such as slits, or dependant on the wavelength, such as a monochromator or energy sensitive detector, or both, like a focusing device. The intrinsic peak profile is determined purely by the interference of the beams and depends on the spatial distribution of electrons in the crystal. In our case, under high pressure, stresses and pressure gradients usually

produce peaks much larger than the above components and correspond to a distribution of plane d-spacings throughout the sample. We might assume from the central limit theorem that the convolution and addition of all these contributions would yield a Gaussian peak, but that is not correct for many setups generate asymmetries or Lorentzian (Cauchy) peak shapes, which have infinite variance and therefore invalidate the use of the CLT. For optimal calculations, the peak shape should be assumed to be a Voigt function which is the convolution of a Lorentzian and a Gaussian function, or a Pearson VII function which can represent a continuous evolution from a Gaussian to a Lorentzian. It might also be necessary to consider asymmetric functions when needed. Whatever peak shape is used, the observed intensity of a peak is represented by its area, not the number of counts at its maximum. If peak widths were constant, this would not be important, but in practice they never are, either because of the sample (strains, *etc*...) or the experimental setup (diffraction geometry, detector resolution, *etc*...).

Appendix B

Synchrotron Radiation Characteristics

B.1 Introduction

Synchrotrons are circular particle accelerators, usually e^- or e^+, which are commonly being used in a parasitic mode as radiation sources. The standard synchrotron facility involves a linac (linear accelerator), the synchrotron and a storage ring. In this text, every time the term synchrotron source is mentioned, we are actually referring to the radiation emitted from the charges in the storage ring. The linac injects the particles in the synchrotron which accelerates them to approximately the speed of light (at CHESS, E=5.2 GeV and $\beta \approx 1\text{-}5 \cdot 10^{-9}$) and injects them in the storage ring. If the source is used for high energy physics, the beam collisions occur in the storage ring at constant particle speed at the vertices of particle detectors.

In the standard mode of operation, when there are no insertion devices, synchrotron radiation is provided at the points where the charged particle beam is curved by bending magnets to provide a quasi-circular orbit. At CHESS, there are two sections which receive radiation, corresponding to two sets of bending magnets and radiated by the e^--beam on one side and the e^+-beam on the other.

This appendix provides the basic information regarding the characteristics of synchrotron radiation emitted using bending magnets. As pointed out previously, the intensity spectrum is of the same type for wigglers, but not for undulators.

B.2 Beam Characteristics

As detailed by Jackson [1975] and Krinsky *et al.* [1983], relativistic charged particles which are centripetally accelerated emit high energy radiation in a cone tangent to their trajectory (**Figure B.1**). When considering a complete arc of the trajectory, this results in a plane of radiation with vertical divergence of the order of γ^{-1} ($\gamma = E/m_0c^2$). The radiation is highly polarized in the plane of the orbit.

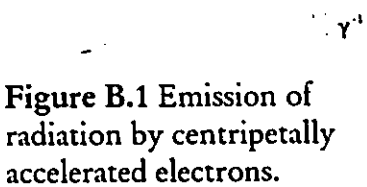

Figure B.1 Emission of radiation by centripetally accelerated electrons.

Several quantities characterizing the orbit and the electron are useful to mention here (for electrons, E is its energy and B the magnetic field of the bending magnet):

γ = 1957 E (GeV) and

ρ (meters) = 33.35 E (GeV)/B (kG) is the radius of curvature of the particle orbit.

It is also useful to define a "critical" wavelength or energy:

$$\lambda_c = \frac{4\pi\rho}{3\gamma^3} = 5.59\frac{\rho}{E^3}\ (\mathring{A})$$
$$\epsilon_c = \frac{3\hbar c\gamma^3}{2\rho} = 2.218\frac{E^3}{\rho}\ (keV). \qquad \textbf{(B.1)}$$

Using these definitions, the flux of photons of energy ϵ or wavelength λ emitted over a 1 mrad arc, with a 1% bandwidth, for an electron current I is

$$N(\lambda) = 1.256\times10^{11}\gamma I G_1\left(\frac{\lambda_c}{\lambda}\right), \qquad \textbf{(B.2)}$$

where $G_1(x) = x\int_x^\infty K_{5/3}(\eta)d\eta$.

When using synchrotron radiation without focusing the beam vertically, which is the

case in our EDX experiments, the collimator we use is sufficient to collect only the portion of the beam which is in the orbital plane ($\psi=0$). In those conditions, then photon flux is given by

$$\left[\frac{\partial N}{\partial \psi}\right]_{\psi=0} d\psi = 3.461\times10^{7} I\gamma^{2}\left(\frac{\lambda_c}{\lambda}\right) K_{2/3}{}^{2}\left(\frac{\lambda_c}{\lambda}\right), \qquad \text{(B.4)}$$

where $K_{2/3}(x)$ is a modified Bessel function. This represents the photon flux useful to our experiments, a plot of which can be seen in **Figure 2.2.**

Appendix C

XRDA: Analyzing Powder X-Ray Diffraction Spectra[†]

C.1 Introduction

XRDA is a computer program I wrote to assist in the analysis of powdered samples' x-ray diffraction spectra. It runs on a PC in the Microsoft® Windows™ graphical shell, providing the user with an essential visual feedback on the analysis process. Along with its power as a standalone program, it also integrates with other programs through several of the Windows data transfer mechanisms: the static clipboard method for basic operations and the more sofisticated OLE 2 protocol for linking and embedding the analysis results in other programs.

The program is written in C++ using the Borland® ObjectWindows™ Library (OWL 2.5) and compiled using Borland C++ 4.5. It is curently at version 4.0. Several major interface changes have been made since version 1.0, but the core analysis elements are generally the same. In some cases, errors were found and corrected, but most importantly all the algorithms were revised and optimized to be much more efficient.

A description of the analysis process and the interface of the program are presented, along with the most important analysis tools and their implementation in the program.

[†] The content of this chapter is partially covered in an article introducing and describing XRDA, "**XRDA: a program for energy-dispersive X-ray diffraction analysis on a PC**", S. Desgreniers and K. Lagarec, *J. Appl. Cryst.*, 27, 432-34 (1994).

Borland C++ and ObjectWindows are registered trademarks of Borland International Inc., Windows is a trademark of Microsoft Corporation.

C.2 Interface Design and Analysis Process

C.2.1 Presentation of the Data

The program is designed so that up to 5 phases (or 5 compounds) can be dealt with simultaneously in a spectrum. Fitted peaks, structure parameters, atomic positions, etc. can be assigned to each phase for them to be analyzed (fitted and/or used as a pressure gauge).

The program is based on a document/view model, assigning to each analysis (document) several ways to view the data. Essentially, 4 types of views can be displayed simultaneously:

▸ the *Plot View* which displays the actual spectrum, as well as the contour of the fitted peaks and the histogram (or markers) for each of the phases' calculated peaks. Its display is fully customizable and can be printed, producing presentation quality graphics. This view can be inserted in another application as an OLE object.

▸ the *Peak View* textually displays the analysis information, based around the 5 phases and their peaks. Information about the peaks and the structure is displayed and all calculated information is updated when a structure fit is performed. Peaks can be assigned Miller indexes, included or excluded from the fit, moved to another phase, etc. Also, their information can be copied to the clipboard for easy integration into another document. Each phase is assigned a button which provides dialog boxes displaying all their information.

▸ When a phase is fitted, the *Calculations View* displays all the calculated peaks' calculated and observed d-spacing and intensity, for a complete comparison of the fit results.

▸ A *Cell View* is also available to view the unit cell of each phase in 3D, with its various atoms. The image can be generated using a perspective-type view, or an orthoscopic view to suit the user. It can be rotated using a pitch-yaw-roll model and otherwise completely customized. An animation can also be performed by specifying initial and final parameters, enabling a fly-by view of the structure.

C.2.2 Analysis Process

To perform a basic analysis, the *Plot View* is used to subtract the backrgound or smooth the data. Then, the peaks can be fitted according to a selected profile shape function. Several peaks can be fitted simultaneously within a region, providing the user with correct area and FWHM parameters even when the peaks are not clearly resolved.

Once the peaks have been fitted, they are assigned to a phase and attributed Miller indices. When a sufficient amount of peaks have been specified for a phase, its lattice

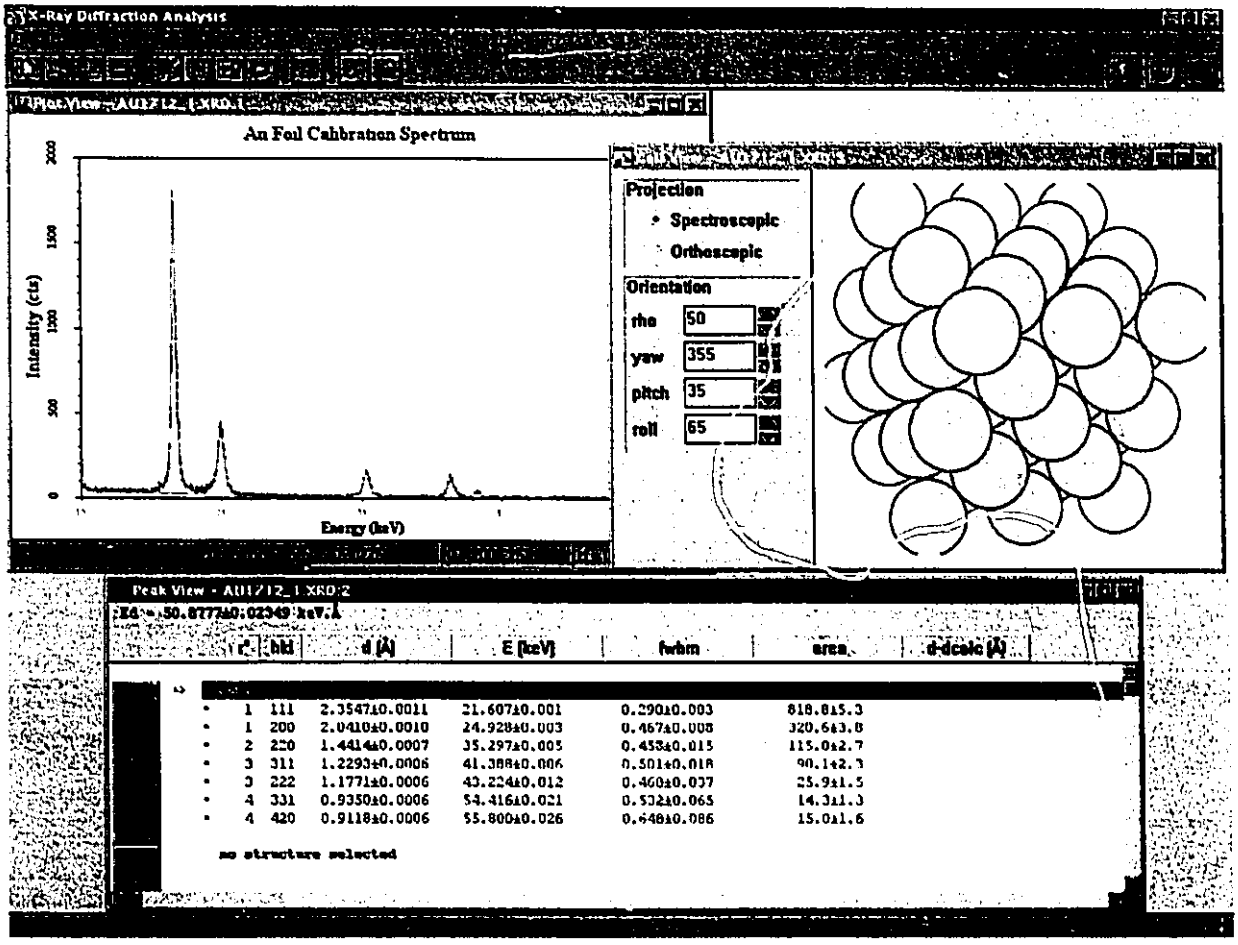

Figure C.1 Example of the analysis of a spectrum using XRDA. The peaks are fitted in the Plot View and manipulated in the Peak View. The Cell View shows a display of the atoms in the unit cell. The ToolBar and menu are context sensitive, varying depending on the selected view.

parameters can be refined to fit those peaks. Optionally, if atomic positions are known, they are used to calculate the intensities of the theoretical pattern.

Before performing a structure fit, it might be necessary to calculate the calibration constant for the spectrum and its uncertainty. It can be entered manually or determined from the calibration spectrum of any cubic structure.

Both EDX and ADX spectra can be analysed using this program, in which only the most basic functions have been specified here. For example, the EOS of a pressure calibrating material can be entered to determine the pressure, or the previous analysis of a similar spectrum can be used to guess the (*hkl*) assignments of a new spectrum.

C.3 Peak Profile Shape Functions (PSF)

C.3.1 Mathematical Description

When analyzing an XRD spectrum, it is necessary to extract the positions of all the peaks in the pattern, and optionally their width (FWHM) and area (integrated intensity). XRDA serves as a tool to fit several peaks to any type of data, according to 6 different profile shape functions and 3 types of background (none, linear or quadratic). Along with the accurate determination of well resolved peaks, it can also successively fit several peaks when they are not properly resolved.

Table C.1 List of the profile shape functions available in XRDA (H_k is the FWHM).

Name	Mathematical Form
Lorentzian	$L(x) = \frac{1}{\pi}\frac{2}{H_k}\left[1+4\frac{(x-x_0)^2}{H_k^2}\right]^{-1}$
Gaussian	$G(x) = \frac{1}{\sqrt{\pi}}\frac{2\sqrt{\ln 2}}{H_k}\exp\left[-4\ln 2\frac{(x-x_0)^2}{H_k^2}\right]$
Intermediate Lorentzian	$IL(x) = \frac{1}{2}\frac{2\sqrt{2^{2/3}-1}}{H_k}\left[1+4(2^{2/3}-1)\frac{(x-x_0)^2}{H_k^2}\right]^{-1.5}$
Modified Lorentzian	$ML(x) = \frac{2}{\pi}\frac{2\sqrt{2^{1/2}-1}}{H_k}\left[1+4(2^{1/2}-1)\frac{(x-x_0)^2}{H_k^2}\right]^{-2}$
Pseudo-Voigt	$PV(x) = \eta L(x)+(1-\eta)G(x)$
Pearson VII	$P7(x) = \sqrt{\pi}\frac{\Gamma(m)}{\Gamma(m-0.5)}\frac{2\sqrt{2^{1/m}-1}}{H_k}\left[1+4(2^{1/m}-1)\frac{(x-x_0)^2}{H_k^2}\right]^{-m}$

C.3.2 Why Provide Different PSF's ?

As pointed out in previous chapters, the shape of the intensity distribution of a peak depends on many experimental and sample specific factors. The convolution of all these source and response function produces the final peak profile function. In general, the response functions can be represented as symmetrical Lorentzians or Gaussians. This is never quite true though, since several experimental setups are known to produce asymmetric peaks, and some response functions, due to slits, are either square or triangular. However, the best general case symmetrical PSF would be a Voigt function, which is the convolution of a Gaussian and a Lorentzian:

$$V(x) = \int_{-\infty}^{\infty} ds L(s) G(s-x) \qquad \text{(C.1)}$$

This PSF would be very general, since, according to the Central Limit Theorem, the convolution or sum of random distributions with finite variance converges to a gaussian distribution, and the convolution of several Lorentzians (which has an infinite variance) is a Lorentzian. The general convolution of finite and infinite (Lorentzian-type) distributions should then be a Voigt distribution.

Unfortunately, evaluating this function and its derivatives requires the integration of a function which is very time consuming, so simplifications of the Voigt function are used: the Pseudo-Voigt and the Pearson VII. As seen in **Table C.1** , the Pseudo-Voigt function is simply a linear combination of a Gaussian and a Lorentzian with different FWHM's but the same peak position. The FWHM of the Pseudo-Voigt as well as the mixing parameter η have been related to the FWHM of the Gaussian and the Lorentzian by Hastings [1984], by fitting the Pseudo-Voigt to real Voigt functions and modelling the interdependancies of the fitted parameters. Using these relations, the Pseudo-Voigt reproduces a real Voigt function to a precision better than 10^{-3} for a unit area distribution.

The Pearson VII function is a Lorentzian-type function with a variable m exponent which also represents the mixing of the Lorentzian and Gaussian characteristics. An exponent of 1 is a pure Lorentzian, whereas an infinite exponent produces a Gaussian (in practice, $m=10$ is very close to a Gaussian). Intermediate exponents represent a evolution between both behaviours (very broad tail to very little tail), of which special cases are the Intermediate Lorentzian ($m = 1.5$) and the Modified Lorentzian ($m = 2$). In general, a Pearson VII can also very accurately mimic a Voigt function.

Additionally, the pure Gaussian and Lorentzian functions can also be selected for comparison. When a peak is fitted, the reduced χ^2 value of the fit is given, so each type of PSF can be compared visually and numerically.

C.4 Structure Fitting Method

Once a sufficient number of peaks have been fitted and assigned Miller indices, the lattice parameters of the structure can be refined to suit the desired peak positions. The same χ^2 minimization routine as for fitting PSFs is used here, but the χ^2 function is the sum of the squared differences of Q values for each peak, where $Q = d^{-2}$. Additionally, σ_Q, the uncertainty on Q is used as the fitting weight, where σ_Q is related to σ_d: $\sigma_Q/Q = \sigma_d/d$.

$$\chi^2_r = \frac{1}{n-m}\sum_{i=1}^{n}\frac{1}{\sigma_i}\left(Q_i - Q_{hkl_i}\right)^2 \qquad \text{(C.2)}$$

Recall that σ_d depends on the uncertainty on the peak position (σ_E or $\sigma_{2\theta}$) as obtained by the peak fitting routine and the uncertainty on the calibration constant (σ_{Ed} or σ_λ):

for EDX analyses,

$$d = \frac{Ed}{E}, \qquad \left(\frac{\sigma_d}{d}\right)^2 = \left(\frac{\sigma_{Ed}}{Ed}\right)^2 + \left(\frac{\sigma_E}{E}\right)^2 \qquad \text{(C.3)}$$

and for ADX analyses,

$$d = \frac{\lambda}{2\sin\theta}, \qquad \left(\frac{\sigma_d}{d}\right)^2 = \left(\frac{\sigma_\lambda}{\lambda}\right)^2 + \left(\frac{\sigma_\theta}{\tan\theta}\right)^2 \qquad \text{(C.4)}$$

The weighing can also be set to a unit weight for all peaks, but this method does not give correct uncertainty calculations. The non-linear least squares fitting scheme is the Levenberg-Marquardt method [1963], and it generates the covariance matrix [C] of the fitting function, from which the uncertainties are extracted, $\sigma_i = \chi_r^2 C_{ii}$. When the model is correct and the weights are properly evaluated, $\chi_r^2 \approx 1$ and $\sigma_i = C_{ii}$ as it should be. By multiplying them by χ_r^2 ensures that incorrect models yield the absurd uncertainties required to accomodate it.

Several other goodness-of-fit (GOF) methods could be added to test the validity of the fit, but all GOF indicators basically represent the same thing as the χ_r^2 does. Additionally, the calculated d-spacings for each peak are displayed along with the difference between the observed and calculated values. If this difference exceeds the uncertainty, it is highlighted for easy identification. Sometimes, a typing error in the Miller indices of a peak or its misindexing might be hard to identify otherwise. Also, a histogram of calculated peaks can be compared to the actual data for easy indexing of other peaks and assessment of the quality of the fit.

C.5 Conclusion

This appendix merely describes the essential elements of XRDA and show its capabilities to analyse and manage powder XRD spectra. Along with the features detailed here, it has many useful features and nifty interface components which have been developed to simplify the user's burden of analyzing a great deal of data. It is also very customizable and produces presentation quality graphics and printouts to display the results of the analysis.

Since its early stages of development it has evolved into a very powerful tool which has served throughout the analysis presented in this thesis and is now being used by several other research groups for similar analyses.

Appendix D

Analyzing Imaging Plates with IPA and Rietveld Analysis

D.1 Introduction

Using Imaging Plates (IP) to acquire ADX diffraction patterns is a relatively new technique that has proven very useful because of the high quality of the data and their ease of use. Very often used when performing single crystal experiments, IPs can also be used in powdered samples measurement in which a simple I vs. 2θ spectrum is required for the analysis. In a normal setup, the IP records a 2D image of the Debye rings intercepting the plate, so the intensities along these rings must be integrated to get the desired Intensity vs. 2θ-spectrum. Over the past few years, several groups have developed their own program to perform this integration process, but none seemed sufficiently satisfying. A new program, IPA, was thus written for our use in analyzing the few images we had, and to provide a proven basis for the use and analysis of future ADX measurements.

IPA is written to work in the Microsoft® Windows™ environment, on a PC, because of the widespread use of the PC and its significant increases in processing power and memory capacities. The program is written in 32 bit C++ code, also using the Borland® ObjectWindows™ Library. 32 bit code was preferred in this case to avoid the segmented memory encumbrances of 16 bit code when dealing with very large memory blocks, as the IP data is roughly 10 MB in size and as such requires large memory blocks.

The following sections present insights on the interface of the program and some of the algorithms used to provide the simple yet powerful analysis required. Another section deals with DBWS [Young, 1994] which was used to perform the Rietveld analysis of the integrated data.

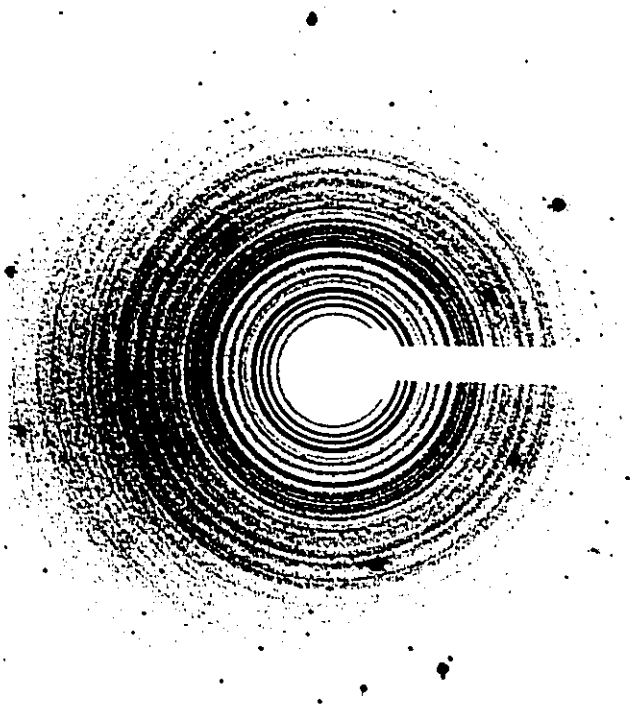

Figure D.1 Example of an IP showing the diffraction pattern of baddeleyite-type HfO_2 at ambient pressure, inside a Merril-Bassett DAC. Some Pt was used to calibrate for pressure and, in this case, to determine the sample-to-plate distance. The very bright spots on the image are due to *Bragg reflections* from the DAC diamonds which also diffract the X-rays. The shadow on the centre-right of the image is that of the beam stop which was used to attenuate the direct beam, whose central spot is still noticeable.

D.2 Using IPA to Analyze the IP

IPA uses a standard graphical interface to view and analyse the IP image. Initially, the 10 MB file is loaded and binned 4×4 so it can be viewed in its entirety on a high resolution screen (1024×768). A zoom window is also available to view the original data when the zoom magnification requires it. Any operation can be done in either window.

The first step of the analysis is to determine the position where the direct beam hit the IP. When choosing a beam stop, we selected one which would attenuate the beam sufficiently

to leave a small trace on the IP. The central intensity distribution is fitted to a 2D elliptical Gaussian in order to locate the direct beam position (x_c, y_c). Next, the orientation of the direct beam with respect to the plate must be determined (**Figure D.2**). Only S_x, S_y and ρ are needed. The parameters can be obtained through several methods:

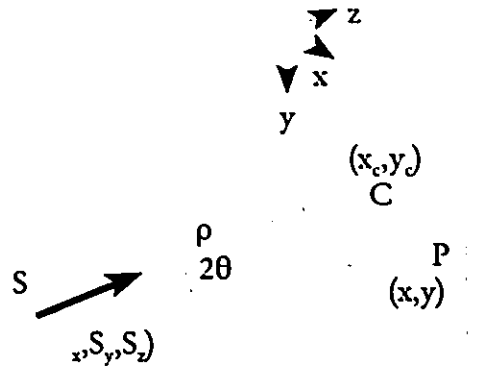

Figure D.2 Setup parameters for the integration of the IP image.

- if the sample-to-plate distance is already known from a previous calibration, a finesse algorithm can be applied to determine S_x and S_y.
- if it is a calibration spectrum or contains a reference material, one can fit the ring of known angle 2θ to determine all three parameters.
- one can manually perform the optimization of S_x and S_y so that the simulated ellipse actually corresponds to the observed ones for different angles.

Once the plate parameters are known, the image can be integrated, that is, the image data is read and the angle corresponding to a pixel is determined and the pixel counts binned to the correct angle range. The output can be a fixed angle step or a fixed ellipse radius step, resulting in an intensity vs. 2θ profile similar to the output of a conventional diffractometer.

Additionally, it is possible to eliminate regions from the integration if they are not desired (for example, the Bragg reflections from the diamond anvils). It is also possible to flip the image vertically and/or horizontally if necessary. Some other functions simplify the two plate distances calibration procedure for easy sample-to-plate distance calibration.

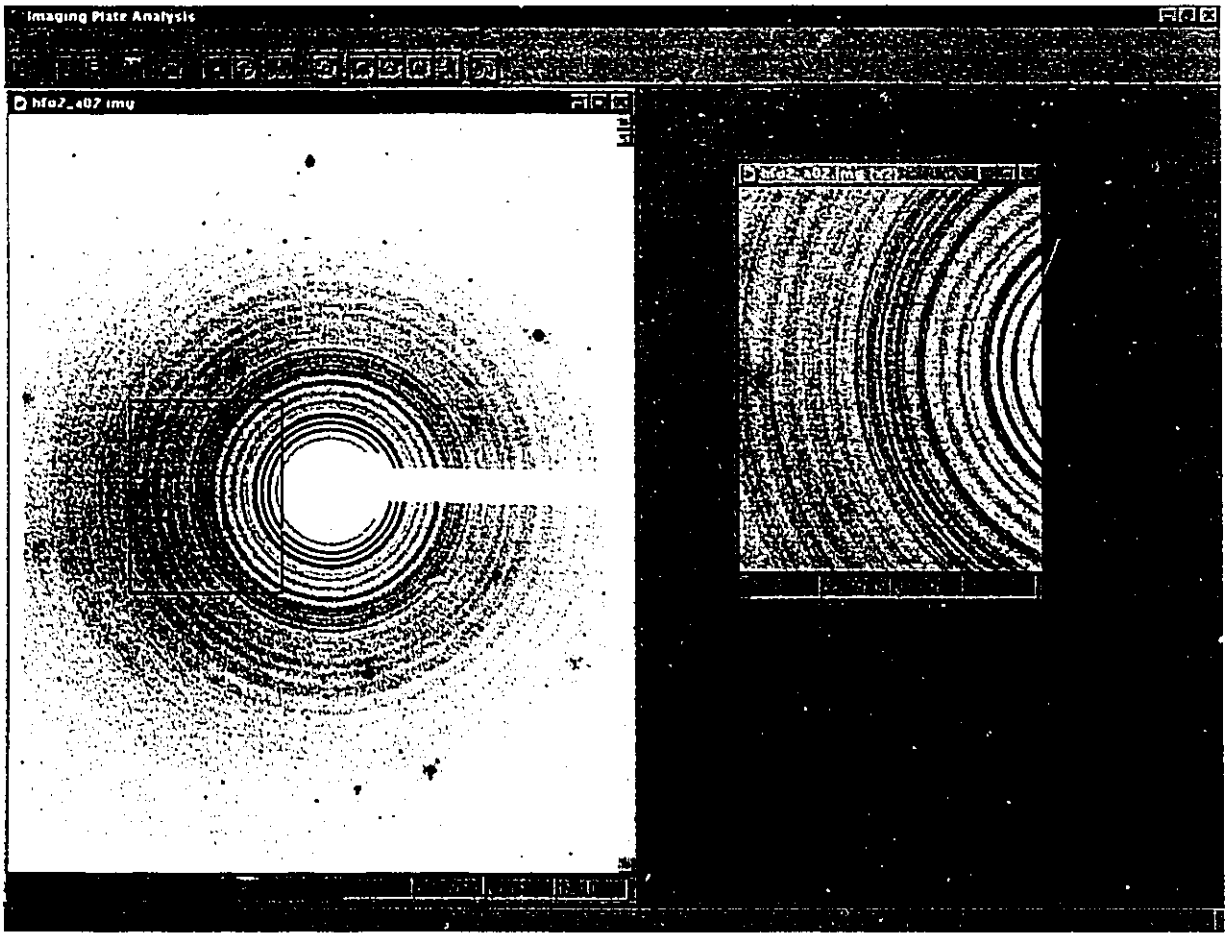

Figure D.3 Screen display during the analysis of an IP with the diffraction pattern of HfO_2. The main image is a 4×4 bin of the actual recorded data, along with a Zoom window for precise observations.

D.3 Main Formulae Used in IPA

In this section, we present the basic formulae used in the analysis of the IP. According to **Figure D.2** , the angle 2θ can be determined for each point (x,y) of the IP. Consider the relative coordinates (X,Y) with respect to the direct beam point: $X=x-x_c$ and $Y=y-y_c$. If S is the point where the diffracting sample is and (S_x,S_y,S_z) is the direct beam vector, then the angle between (SC) and (SP) is

$$\theta = \frac{\vec{SC}\cdot\vec{SP}}{SC\,SP}, \tag{D.1}$$

but $\vec{SC} = \rho\vec{S}$ and $\vec{SP} = \vec{SC}+\vec{CP} = \rho\vec{S}+\vec{CP}$. When using S_x, S_y, X and Y, this reduces to

$$\cos 2\theta = \frac{\rho+(XS_x+YS_y)}{\sqrt{\rho^2+(X^2+Y^2)+2\rho(XS_x+YS_y)}}, \tag{D.2}$$

or

$$\tan^2 2\theta = \frac{(X^2+Y^2)-(XS_x+YS_y)^2}{(XS_x+YS_y+\rho)^2}. \tag{D.3}$$

which is the equation used in IPA to determine the angle for any given point (x,y). This is also the equation used to fit the parameters S_x, S_y and ρ to an ellipse corresponding to a known angle 2θ.

When desired, the S_x and S_y parameters can be refined to increase the finesse of the integrated profile, based on a method proposed by Piltz *et al.* [1992]. In IPA, the image is decomposed into n (user-defined) azimuthal slices which are independently binned using estimated values of S_x and S_y. This produces n sets of estimated profiles data. The finesse algorithm optimizes S_x and S_y such that the variance v of the sum of these sets is maximized:

$$v = \frac{\langle I^2\rangle-\langle I\rangle^2}{\langle I\rangle^2} = \frac{\langle I^2\rangle}{\langle I\rangle^2}-1. \tag{D.4}$$

These averages are performed on 2θ (or an equivalent radius), after the sets were added together. Since the square of the sum rises faster than the sum of the squares, this algorithm produces peaks which are thinner and higher rather than wide and low in counts, as desired.

D.4 Rietveld Analysis and DBWS

Rietveld analysis [Rietveld, 1969] is a powerful method to analyse powder X-ray or neutron diffraction spectra and to extract the most information possible from them. Essentially, it is a non-linear optimization of a calculated spectrum to the observed spectrum. The theoretical spectrum is built using all the atomic and lattice parameters (positional, thermal, scattering factors, phase proportions, etc). There are numerous programs available to perform the analysis, and we have chosen DBWS, a program written by Young *et al.* [1994], in its November 1994 version. This program uses data acquired in a standard Bragg-Brentano geometry which has a specific Lorentz-polarization factor correction. In the IP setup, there is

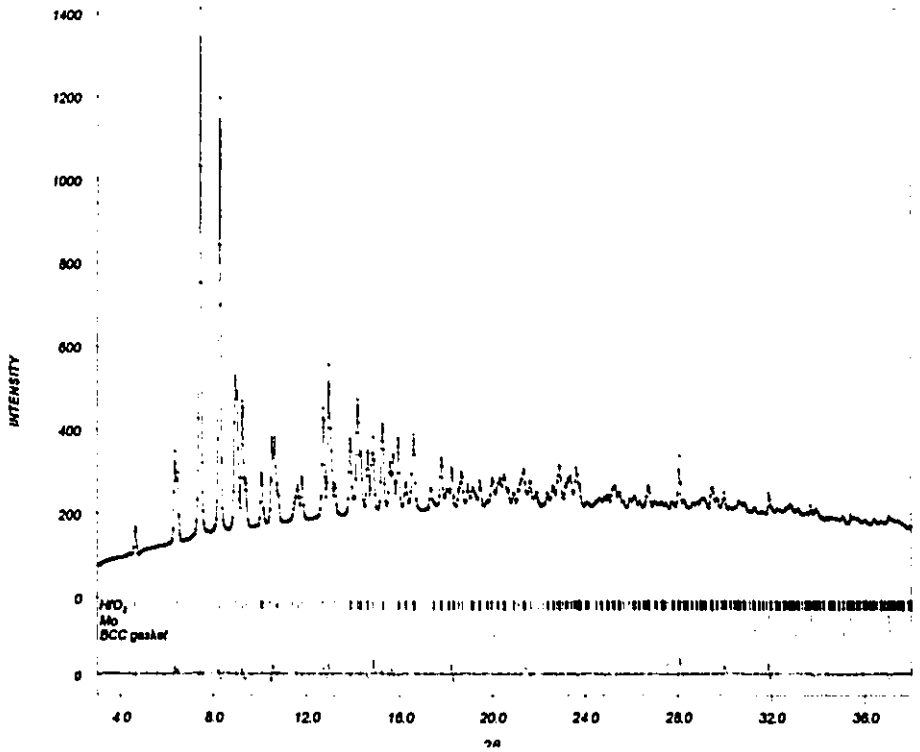

Figure D.4 Resulting integrated spectrum of the HfO_2 IP image (crosses), with the Rietveld analyzed simulated spectrum (line). The difference spectrum is displayed on the bottom, which shows there is a slight problem with the Mo phase since all the Mo intensities are off by a bit. A BCC phase from the gasket was also included to account for the strongest (111) line which is visible as a shoulder in the HfO_2 lines. No preferred orientation correction was included in this adjustment.

no specific Lorentz correction because there are no slits which limit the area detected involved. Hence, the spectrum had to be corrected for the Bragg-Brentano Lp factor. As an example of how well the IP method and IPA work, we have tested it with a less than optimal (inside a DAC) spectrum of baddeleyite-type HfO_2. Additionally, Mo and gasket phases were included in the refinement process. The resulting integrated spectrum with the final simulated spectrum and their difference are shown in **Figure D.4** . Results are in good agreement with other published results on HfO_2, considering the disparity already present in these results **(Table D.1)**.

Table D.1 Comparison between the lattice and atomic parameters obtained in our Rietveld analysis of a diffraction image integrated by IPA, and those published in separate works. No isotropic thermal parameter was included for the oxygen atoms since their uncertainty exceeded 100%. It is reasonable that the greatest difference occur in oxygen atoms positions since they contribute very little to the spectrum because of their low atomic number ($I \propto |F|^2 \approx Z^2$).

Space group $P2_1/c$ (n° 14), Z=4
Baddeleyite-type structure

		this work	Adams *et al.*	Hann *et al.*
cell parameters				
	a (Å)	5.1198(1)	5.1187(4)	5.1170(1)
	b (Å)	5.1745(1)	5.1693(1)	5.1754(2)
	c (Å)	5.2957(1)	5.2970(4)	5.2915(2)
	β (°)	99.192(2)	99.180(9)	99.216(2)
atomic positions				
Hf	x	0.2744(3)	0.2764(2)	0.2755(2)
	y	0.0396(2)	0.0402(1)	0.0397(1)
	z	0.2073(3)	0.2074(2)	0.2080(2)
	B_{iso} (Å²)	0.38(1)	0.34(1)	0.05(2)
O1	x	0.0782(38)	0.0709(20)	0.0742(21)
	y	0.3328(34)	0.3319(18)	0.3316(18)
	z	0.3456(34)	0.3438(18)	0.3467(18)
O2	x	0.4609(42)	0.4464(17)	0.4487(21)
	y	0.7520(27)	0.7554(16)	0.7581(16)
	z	0.4775(52)	0.4796(18)	0.4801(23)
refinement statistics				
	R_{wp}	2.07	10.91	9.61
	$d_{Durbin-Watson}$	0.94		
	R_{BRAGG}	4.44	4.48	1.13

D.5 Conclusion

IPA is a simple program used to view and analyse images produced using the Imaging Plate technology, with angle dispersive X-ray diffraction. It is run on a PC with minimal requirements yet produces very high quality analysis and has all the necessary display capabilities required to use IPs. As an example of its use, it has been tested by performing Rietveld analysis on the resulting spectrum and comparing it to other similar analyses, producing equivalent results. In any case, it has already proven itself as being an invaluable tool during the acquisition process, since the images could very rapidly be viewed and calibrated, and a rapid integration could be performed, all in the same program.

REFERENCES

S. C. Abrahams and J. L. Bernstein, "Rutile: Normal Probability Plot Analysis and Accurate Measurement of Crystal Structure", *J. Chem. Phys.*, 55, 3206 (1971).

D. M. Adams, S. Leonard, D. R. Russell and R. J. Cernik, "X-Ray Diffraction of Hafnia Under High Pressure Using Synchrotron Radiation", *J. Phys. Chem. Solids*, 52, 1181-86 (1991).

O. L. Anderson, in *The Nature of the Solid Earth*. Edited by E. C. Robertson, McGraw-Hill, New York (1972).

H. Arashi and M. Ishigame, "Raman Spectroscopic Studies of Polymorphism in ZrO_2 at High Pressures", *Phys. Status Solidi*, 71, 313-21 (1982).

H. Arashi, T. Yagi, S. Akimoto and S. Kudoh, "New High-Pressure Phase of ZrO_2 Above 35 GPa", *Phys. Rev. B*, 41, 4309-13 (1990).

H. Arashi, "Raman Spectroscopic Study of the Pressure-Induced Phase Transition in TiO_2", *J. Phys. Chem. Solids*, 53, 355-59 (1992).

N. W. Aschcroft and N. D. Mermin, *Solid State Physics*. Saunders College (1976).

N. A. Bendeliani, S. V. Popova and L. F. Vereshchagin, "New Modification of Titanium Dioxide Obtained at High Pressures", *Geoch. Intern.*, 3, 387-90 (1966).

N. A. Bendeliani, S. V. Popova and L. F. Vereshchagin, "New High Pressure Modifications of ZrO_2 and HfO_2", *Geoch. Intern.*, 4, 557 (1967).

H. Berger, H. Tang and F. Lévy, *J. Cryst. Growth*, 130, 108 (1993).

F. Birch, *J. Geophys. Res.*, 57, 227 (1952).

G. Burns and A. M. Glazer, *Space Groups for Solid State Scientists*. Academic Press (1990).

R. E. Cohen, M. J. Mehl and L. L. Boyer, "Phase Transitions and Elasticity in Zirconia", *Physica B*, 150, 1-9 (1988).

C. Cohen-Tannoudji, B. Diu and F. Laloë, *Mécanique quantique I et II*. Hermann, Paris (1977).

K. Deberlin and R. G. Helmer, *Gamma- and X-Ray Spectrometry with Semiconductor Detectors*. Elsevier Science Publishers (1988).

S. Desgreniers and K. Lagarec, "XRDA: A Program for Energy-Dispersive X-Ray Diffraction Analysis on a PC", *J. Appl. Cryst.*, 27, 432-34 (1994).

F. Dachille, P. Y. Simons and R. Roy, "Pressure-Temperature Studies of Anatase, Brookite, Rutile and TiO_2-II", *Am. Miner.*, 53, 1929 (1968).

S. Endo, I. Takenaka and H. Arashi, 1993 AIRAPT Conference, Proceedings #309, 1, 371 (1993).

A. Fahmi, C. Minot, B. Silvi and M. Causa, "Theoretical Analysis of the Structures of Titanium Dioxide Crystals", *Phys. Rev. B*, 47, 11717 (1993).

K. M. Glassford and J. R. Chelikowsky, "Structural and Electronic Properties of Titanium Dioxide", *Phys. Rev. B*, 46, 1284-98 (1992).

B. Gou, Z. Liu, Q. Cui, H. Yang, Y. Zhao and G. Zou, "Raman Study of Anatase (TiO_2) at High Pressure", *High Pressure Research*, 1, 185-91 (1989).

J. Haines and J. M. Léger, "X-Ray Diffraction Study of TiO_2 up to 49 GPa", *Physica B*, 192, 233-37 (1993).

J. Haines, J. M. Léger and A. Atouf, "Crystal Structure and Equation of State of Cotunnite-Type Zirconia", *J. Am. Ceram. Soc*, 78, 445 (1995).

R. E. Hann, P. R. Suitch and J. L. Pentecost, *J. Amer. Ceram. Soc.*, 68, C285 (1985).

J. B. Hastings, W. Thomlinson and D. E. Cox, "Synchrotron X-Ray Powder Diffraction", *J. Appl. Cryst.*, 17, 84 (1984).

A. M. Hofmeister, "Interatomic potentials calculated from equations of state: Limitations of finite strain to moderate K'", *Geophys. Res. Let.*, 20, 635-638 (1993).

C. J. Howard, E. H. Kisi and O. Ohtaka, "Crystal Structures of Two Orthorhombic Zirconias", *J. Am. Ceram. Soc.*, 74, 2321-23 (1991).

J. D. Jackson, *Classical Electrodynamics*. 2nd ed. Wiley, New York (1975).

A. Jayaraman, "The Diamond-Anvil High Pressure Cell", *Scientific American* (Jan 1984).

A. Jayaraman, S. Y. Wang, S. K. Sharma and L. C. Ming, "Pressure-Induced Phase Transformations in HfO_2 to 50 GPa Studied by Raman Spectroscopy", *Phys. Rev. B*, 48, 9205-11 (1993).

C. Kittel, *Introduction to Solid State Physics*. 6th ed., Wiley (1986).

S. Krinsky, M.L. Perlman and R.E. Watson, "Characteristics of Synchrotron Radiation and of Its Sources", in *Handbook on Synchrotron Radiation*. Edited by E.-E. Koch, North-Holland Publishing Company, Netherlands (1983).

Y. Kudoh, H. Takena and H. Arashi, "In Situ Determination of Crystal Structure for High Pressure Phase of ZrO_2 Using a Diamond Anvil and Single Crystal X-Ray Diffraction Method", *Phys. Chem. Minerals*, 13, 233-37 (1986).

G. L. Kulcinski, "High-Pressure Induced Phase Transition in ZrO_2", *J. Am. Ceram. Soc.*, 51, 582-84 (1968).

K. Lagarec and S. Desgreniers, "Raman Study of Single Crystal Anatase TiO_2 up to 70 GPa", *Solid State Commun.*, 94, 519-524 (1995).

J. M. Léger, P. E. Tomaszewski, A. Atouf and A. S. Pereira, "Pressure-Induced Structural Phase Transitions in Zirconia Under High Pressure", *Phys. Rev. B*, 47, 14075-83 (1993a).

J. M. Léger, A. Atouf, P. E. Tomaszewski and A. S. Pereira, "Pressure-Induced Phase Transitions and Volume Changes in HfO_2 up to 50 GPa", *Phys. Rev. B*, 48, 93-98 (1993b).

R. K. Linde and P. S. DeCarli, "Polymorphic Behavior of Titania under Dynamic Loading", *J. Chem. Phys.*, 50, 319 (1969).

L. Liu, "New High Pressure Phases of ZrO_2 and HfO_2", *J. Phys. Chem. Solids*, 41, 331-34 (1980).

L. Liu, "High-pressure phase transformations of the dioxides: Implications for structures of SiO_2 at high pressure", *High-pressure research in geophysics*. Edited by S. Akimoto and M. H. Manghnani, Tokyo (1982).

L. Liu and W. A. Bassett, *Elements, Oxides, Silicates. High-Pressure Phases with Implications for the Earth's Interior*. Oxford University Press, New York (1986).

J. F. Mammone, S. K. Sharma and M. Nicol, "Raman Study of Rutile (TiO_2) at High Pressures", *Solid State Commun.*, 24, 799-802 (1980).

J. F. Mammone, M. Nicol, S. K. Sharma, "Raman Spectra of TiO_2-II, TiO_2-III, SnO_2 and GeO_2 at High Pressure", *J. Phys. Chem. Solids*, 42, 379-84 (1981).

Manghnani, M. H., "Elastic Constants of Single-Crystal Rutile Under Pressures to 7.5 kbar", *J. Geophys. Res.*, 74, 4317-28 (1969).

H. K. Mao, P. M. Bell, J. W. Shaner and D.J. Steinberg, "Specific Volume Measurements of Cu, Mo, Pd and Ag and Calibration of the Ruby R_1 Fluorescence Pressure Gauge from 0.06 to 1 Mbar", *J. Appl. Phys.*, 49, 3276-83 (1978).

D. W. Marquardt, *Journal of the Society for Industrial and Applied Mathematics*, 11, 431-441 (1963).

J. D. McCullough and K. N. Trueblood, "The Crystal Structure of Baddeleyite (monoclinic ZrO_2)", *Acta Crystallogr.*, 12, 507-11 (1959).

L. C. Ming and M. H. Maghnani, "Isothermal Compression of TiO2 (Rutile) Under Hydrostatic Pressure to 106 kbar", *J. Geophys. Res.*, 84, 4777-79 (1979).

L. C. Ming and M. H. Manghnani, "High Pressure Polymorphs of ZrO_2", pp 135-40 in *Solid State Physics Under Pressure.* Edited by S. Minomura, KTK Scientific Publishers, Tokyo (1985).

F. D. Murnaghan, *Proc. Natl. Acad. Sci. U.S.A.*, 30, 244 (1944).

M. V. Nevitt, S. K. Chan, J. Z. Liu, M. H. Grimsditch and Y. Fang, *Physica B*, 150, 230 (1988).

O. Ohtaka, T. Yamanaka, S. Kume, N. Hara, H. Asano and F. Izumi, "Structural Analysis of Orthorhombic ZrO_2 by High Resolution Neutron Powder Diffraction", *Proc. Japan Acad.*, 66(B), 193-96 (1990).

O. Ohtaka, T. Yamanaka and S. Kume, *Nippon Seramikkusu Kyokai Gakujutsu Ronbunshi*, 99, 826 (1991).

R. O. Piltz, M. I. McMahon, J. Crain, P. D. Hatton, R. J. Nelmes, R. J. Cernik and G. Busnell-Wye, "An Imaging Plate System for High-Pressure Powder Diffraction: The Data Processing Side", *Rev. Sci. Instrum.*, 63, 700 (1992).

J.-P. Poirier, *Introduction to the physics of the Earth's interior.* Cambridge University Press, Cambridge (1991).

Powder Diffraction File [Anatase] (JCPDS International Center for Diffraction Data, Swarthmore PA) Inorganic 21-1272.

Powder Diffraction File [Brookite] (JCPDS International Center for Diffraction Data, Swarthmore PA) Inorganic 16-617.

H. M. Rietveld, *J. Appl. Cryst.*, 2, 65 (1969).

R. Ruh and P. W. R. Corfield, *J. Amer. Ceram. Soc.* 53, 126 (1970).

H. Sato, S. Endo, M. Sugiyama, T. Kikegawa, O. Shimomura and K. Kusaba, "Baddeleyite-Type High Pressure Phase of TiO_2", *Science*, 251, 786-88 (1991).

D. K. Smith and H. W. Newkirk, *Acta Crystallogr.*, 18, 983 (1965).

R. Suyama, H. Horiuchi and S. Kume, *Yogyo Kyokai Shi*, 95, 567 (1987).

J. Tang and S. Endo, *J. Amer. Ceram. Soc.*, 76, 796 (1993).

J. S. E. Tse and D. D. Klug, 1993 AIRAPT Conference, Proceedings #309, 1, 209 (1993).

P. Vinet, J. Ferrante, J. R. Smith and J. H. Rose, "A Universal Equation of State for Solids", *J. Phys. C*, 19, L467 (1986).

R. A. Young and A. Sakthivel, *Program DBWS 9411 for Rietveld Analysis of X-ray and Neutron Powder Diffraction Patterns* (1994).